Interactions of Carbon Nanotubes and Lipid Bilayers

Wojciech Rzepala

Department of Physics

University of Oxford



A thesis submitted for the degree of Doctor of Philosophy

Hertford College

Trinity Term 2013

Abstract

Interactions of Carbon Nanotubes and Lipid Bilayers

Wojciech Rzepala, Hertford College, DPhil, Trinity Term 2013

The biological membrane, which is composed of a lipid bilayer embedded with numerous proteins, defines the cell boundary, separating the cell interior from the external environment. It serves as a gatekeeper and entry point for various molecular and ionic species. This thesis describes experimental and simulation studies of the interactions of carbon nanotubes (CNTs) with model membranes (lipid bilayers). The unique properties of CNTs make them ideal candidates for many nanotechnological applications. They can, however, pose a potential risk as toxins. While research into the positive benefits of CNTs continues, very little is known about their basic interactions with cellular components. It is particularly important to understand the interaction of CNTs with biological membranes, which form the primary physical barrier surrounding a cell. Coarse grained molecular dynamics (MD) simulations and atomic force microscopy (AFM) have been used to study the interactions of CNTs and lipid bilayers. They are investigated in a controlled manner using MD simulations, while AFM has allowed the controlled approach-to-contact and insertion of CNTs into bilayers. A number of effects are reported, including lipid creep along the CNT and bilayer thickening upon contact. The robustness of this response is established using different force fields and lipid species. The experimental results show an unusual reaction to mechanical indentation, and are further backed by MD simulations. The lipid bilayer response to multiple CNTs is studied and the effects of CNTs on bilayer conformation and lipid diffusion are reported. CNT internalisation from the solvent is observed in the simulations. Indeed, many of the observed phenomena are reminiscent of those known from the field of membrane protein. This project focuses on understanding the basic molecular interactions of CNTs with lipid bilayers and addresses the gap between experimental and computational work.

Acknowledgements

I would like to thank the following people:

- Prof John Ryan, for introducing me to this project and sparking my interest in biophysics and biological membranes while teaching the physics undergraduate course at Oxford many, many years ago.
- Prof Mark Sansom, for his continuous help and support throughout this thesis, which made much of this work possible.
- Dr Chandra Ramanujan, for teaching and explaining AFM techniques to me, as well as his help on scientific and non-scientific matters.
- Ryan Levitt, for keeping me (relatively) sane throughout these years. I think his own sanity may have suffered a bit.
- Varun Ramraj, for listening to my computer and thesis-related rants, and providing constant opportunities to fill up on caffeine.

Contents

List of Figures vi

List of Tables viii

1 Introduction 1

1.1 The problem . . . 1

1.2 Background . . . 2

1.2.1 Biological membranes . . . 2

1.2.2 Carbon nanotubes . . . 6

1.3 CNTs and biological membranes: The story so far . . . 12

1.4 Perspective . . . 15

2 Theory & Methods 16

2.1 Molecular dynamics simulations . . . 16

2.1.1 Equations of motion . . . 17

2.1.2 Force fields . . . 18

2.1.3 Coarse-grained force fields . . . 23

2.1.4 Algorithms . . . 27

2.2 Software . . . 33

2.3 Atomic force microscopy . . . 33

2.3.1 Overview . . . 33

2.3.2 Principles of operation 34
2.3.3 Tip-sample interaction 36
2.3.4 Modes of operation 44
2.3.5 Force curves 47

3 MD simulations of controlled CNT-lipid bilayer interaction 48

3.1 Methods 49
3.2 Results 51
3.2.1 Response to pulling 52
3.2.2 Sensitivity to lipid species 59
3.2.3 Sensitivity to force field parametrisation 60
3.3 Summary 65

4 Force spectroscopy and mechanical properties of lipid bilayers 67

4.1 Methods 68
4.1.1 Atomic force microscopy 68
4.1.2 Molecular dynamics 72
4.2 Results 74
4.2.1 AFM 74
4.2.2 Molecular dynamics 82
4.3 Discussion 85
4.4 Summary 88

5 MD simulations of free CNT-lipid bilayer interactions 89

5.1 Methods 89
5.2 Results 95
5.2.1 Diffusion 95
5.2.2 Restrained CNT 103

5.2.3 Free CNTs in solution 107
5.3 Summary 109

6 Conclusions **112**

6.1 Summary 112
6.2 Future work 116

Bibliography **119**

List of Figures

1.1 Chemical structure of lipids - DPPC 4
1.2 Lipid bilayer 5
1.3 An overview of CNT shape and structure 6
1.4 Graphene lattice and its relation to CNT structure 7
1.5 Comparison of CNTs with different chirality 8
1.6 Raw CNT bundles - Scanning Electron Microscopy image 10

2.1 Lipid and CNT representations in simulation - Atomistic and Coarse Grained 26
2.2 AFM cantilever in operation 35
2.3 Electric double layer 38

3.1 Simulation scene overview 51
3.2 Trajectory snapshots of CNT-lipid interaction 52
3.3 Cooperative meniscus formation 54
3.4 Lipid creep - trajectory snapshots 55
3.5 Lipid creep rate 56
3.6 Lipid creep rate comparison 56
3.7 Membrane thickness map - CNT-lipid interaction 58
3.8 Membrane radial thickness profile - CNT-lipid interaction 58

3.9 Membrane depression on CNT approach 62

4.1 SEM images of the CNT probe used for measurements 71
4.2 Simulation scene overview 73
4.3 Force curves - Conventional probe 76
4.4 AFM membrane topography with a CNT probe 79
4.5 Force curves - CNT probe 80
4.6 CNT-probe attachment confirmation 81
4.7 Force curves - Simulation 84
4.8 Water layering near a wall 85

5.1 Simulation setup overview - CNT arrays before simulation 91
5.2 CNT with hydrophilic ends 92
5.3 CNT arrays outside the lipid bilayer 93
5.4 CNT arrays in lipid bilayer after equilibration 95
5.5 CNTs in the bilayer after an equilibration run with no restraints 96
5.6 Evolution of the angle between CNT and z-axis 97
5.7 Comparison of standard deviations in CNT direction 98
5.8 CNT angles with the z-axis - free diffusion 99
5.9 Average angles between CNT and z-axis - CNT particle type dependence 100
5.10 Lipid mean square displacements and diffusion coefficients around CNTs 101
5.11 Membrane deformation in response to restrained CNTs 104
5.12 Membrane creep up a CNT 105
5.13 Free CNTs in solution 108
5.14 Free CNTs in solution - approach 108

List of Tables

3.1 Effects of parametrisation - Bond 63
3.2 Effects of parametrisation - MARTINI2 63
3.3 Effects of parametrisation - Bond force field 64
3.4 Effects of parametrisation - MARTINI force field 64
5.1 Summary of simulations done for the chapter 94

1 Introduction

1.1 The problem

In recent years, carbon nanotubes have emerged as one of the most versatile materials known. With varied potential applications, it is inevitable that we will come into contact with them, be it via direct or indirect routes. It is therefore crucial to understand their interactions with the biological environment at all scales, ranging from cellular to macroscopic.

Biological membranes are probably one of the most essential parts of the cell [1]. Life could not exist without cells, and cells would probably not exist without membranes, which provide convenient compartments for the collection of biochemical reactions, collectively known as life. This is why it is important to understand the behaviour of membranes and their interaction with the environment.

This project investigates the interactions of carbon nanotubes with biological membranes. More precisely, it examines the behaviour of lipid bilayers, the most basic structural element of biomembranes, in contact with carbon nanotubes. This is carried out using molecular dynamics computer simulations and atomic force microscopy experiments.

1.2 Background

1.2.1 Biological membranes

Overview

Biological membranes are one of the most common structures found in cells. The closed compartments they provide allow the maintenance of favourable chemical and biochemical conditions that differentiate the cell from its environment, making its existence viable. But the cellular membrane is not the only place where biological membranes can be found. They surround various organelles within the cell itself, differentiating them from other intracellular components.

Structure and properties

On a basic level, biological membranes consist of a bilayer formed of lipids, in which various proteins are embedded. These proteins provide a range of functions to the membrane and are typically specific to different kinds of membranes. Their presence and abundance varies from cell to cell, and from one organelle to another, constituting about a half of membrane weight. The lipid bilayer provides a base, or a scaffold of sort, for protein anchoring. The biomembranes are not static structures. Both the lipids and the proteins are able to move laterally. This makes the membrane a fluid entity, which also facilities interactions.

One of the most important functions of biomembranes is the separation of the cell interior from its environment. They act as the gatekeepers of the cell, as they are semi-permeable, selectively allowing certain substances across. There are a few ways in which molecules can pass the membrane barrier [2]. The simplest is passive transport. This requires no energy input - molecules can cross the membrane by diffusion. This, however, is limited to small, and usually non-polar, and often hydrophobic, molecules [3, 4]. Typ-

ical examples include CO_2 and O_2. This is not a very efficient mode of transport, and it also relies on the osmotic pressure across the membrane. Other molecules, notably large or charged, need to cross the bilayer using different modes of transport. As opposed to diffusion, these modes are active and involve consumption of energy [2]. In endocytosis, the membrane engulfs the molecule to be transported, and deforms inwards, eventually fully surrounding the molecule of interest and releasing it on the other side, inside the cell. This mode of transport is usually employed for large molecules. Finally, certain proteins, known as transporters [5, 6, 7, 8], can move molecules across the membrane. They are very specific and can transfer molecules even against their concentration gradient.

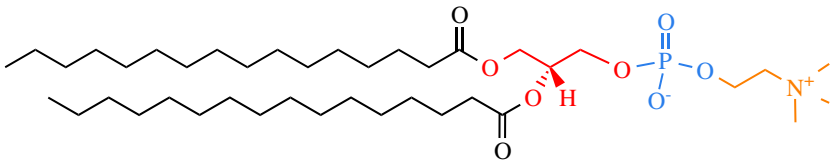
Overall, transport across the membrane can be involved and complicated. Apart from the movement of substances, membranes do have a wealth of other functions [9], including molecular recognition, biosynthesis, energy production, signalling, and nerve conduction. Biological membranes are exceptionally sophisticated and varied systems. To better understand them and their interactions with different molecules, simplified systems can be investigated. By removing some of the underlying complexity, more fundamental processes can be examined. Many aspects of these interactions can be understood by studying lipid bilayers, which, as has been noted earlier, form the basic scaffold underlying the membrane structure.

Lipids and lipid bilayers

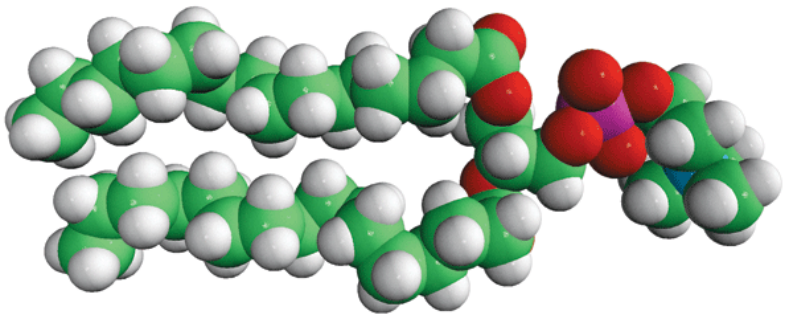
Definition Lipids can be broadly defined as a class of naturally occurring molecules characterised by their general solubility in non-polar solvents, and insolubility in water [10, 11]. This fairly broad definition includes many molecule types, such as fats, waxes, mono-, di-, and triglycerides, as well as phospholipids, sterols and some vitamins. Their main biological functions include signalling, energy storage, and providing structural components in biological membranes [11]. The rest of this section will discuss these structural lipids, which form lipid bilayers.

Structure The main structural lipids include phospholipids, as well as sphingolipids and cholesterol [12]. Of these, phospholipids are the major component of lipid bilayers [13]. A typical phospholipid will consist of a glycerol backbone, with two fatty acyl chains attached to two of its carbons, and a phosphate group occupying the third carbon. A functional group is further attached to the phosphate (fig. 1.1). Some typical functional groups include choline, ethanolamine, and serine, and depending on this moiety, the lipids will be classed as phosphatidylcholines (-PC), phosphatidylethanolamines (-PE) phosphatidylserines (-PS), respectively. Many more functional groups exist, giving different character to the lipids in each class [14, 10, 12, 11, 13]. A representation of one of the most archetypal lipids [15, 13], dipalmitoylphosphatidylcholine (DPPC) is shown in fig. 1.1.

The negative charge on the phosphate group, along with any charge on the functional



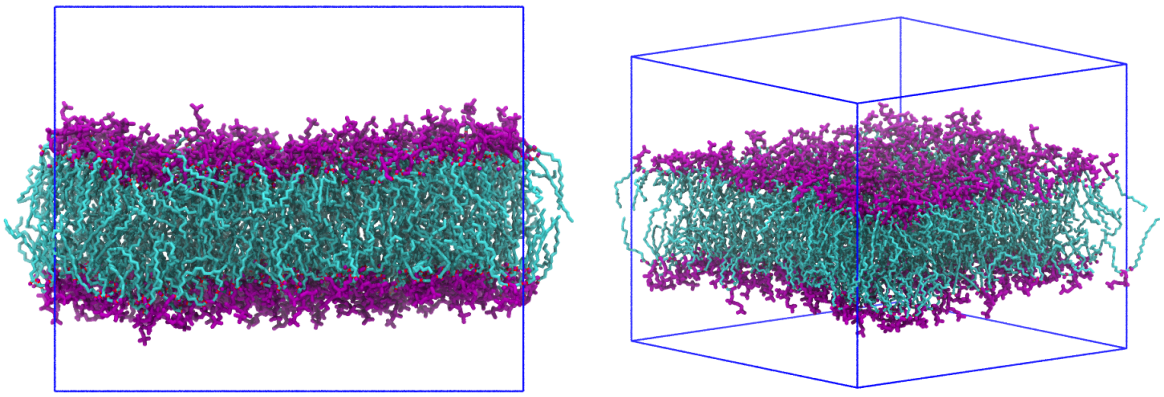
(a) Chemical structure



(b) 3D visualisation

Figure 1.1: Lipid structure. Shown is a dipalmitoylphosphatidylcholine (DPPC) lipid structure, including its (a) chemical, and (b) space-filling representation. In (a), the colours represent: black: fatty acids, red: glycerol backbone, blue: phosphate group, orange: choline group. In (b), the colours correspond to the following atom types: green: carbon, white: hydrogen, red: oxygen, purple: phosphorus, blue: nitrogen. Image source (adapted): Avanti Polar Lipids (www.avantilipids.com).

moiety, will give the headgroup a polar character (and sometimes a net charge). This will make it hydrophilic and more compatible with water. Meanwhile, the acyl chains (hydrocarbon tails) are non-polar, and hydrophobic, in nature. In an aqueous environment, this will lead to an aggregation of lipids, where the hydrophobic lipid tails come together, to minimise the entropic cost of exposure to water. While the hydrocarbons come together, the hydrophilic head groups will be exposed to water. Such self-assembly [16] will result in various structures, depending on the exact character of the lipids involved. PC lipids, the most abundant species forming such structures, due to their shape, will favour planar phases [16, 15, 13], where two layers of lipid will form a bilayer with a core formed of hydrocarbon tails and a water-exposed surface formed of hydrophilic head groups (fig. 1.2). Such an arrangement will minimise the energetic cost of exposing hydrocarbons to water [16]. Other lipids will favour slightly different phases, e.g. PE lipids, due to their relatively small headgroup size and a slightly conical shape, will prefer a different packing, where the resulting structure will have a slight curvature [17]. In reality, the lipid bilayer in a typical membrane will be a mixture of



(a) Side view

(b) Top view

Figure 1.2: Boxed, planar lipid bilayer patch. Shown in cyan are the lipid hydrocarbon tails. Magenta represents all atoms but the hydrocarbon tails. All the space in the box not occupied by lipids represents water.

different lipid species, depending on the membrane function [1, 9].

This work focuses on single component lipid bilayers. Such systems can be used as a good first approximation to the membrane structure. This is because the lipid bilayer is the most basic, crucial, and common component of biological membranes. Studying the interactions of molecules with lipid bilayers allows one to isolate the interactions of interest and focus on them, while avoiding the distractions, cross-effects and complications arising from overcomplexity.

1.2.2 Carbon nanotubes

Overview

Carbon nanotubes (CNT) are an allotropic form of carbon. They take cylindrical shapes (fig. 1.3) and typically have a diameter of the order of nanometres, with a length often in the range of micrometres to millimetres. Ever since their discovery [18, 19], they attracted considerable interest, from both a theoretical and a practical point of view. Their small size and properties (see a later section) open up the possibility of using them in nanotechnology (see later in this chapter). The wealth of their potential uses often

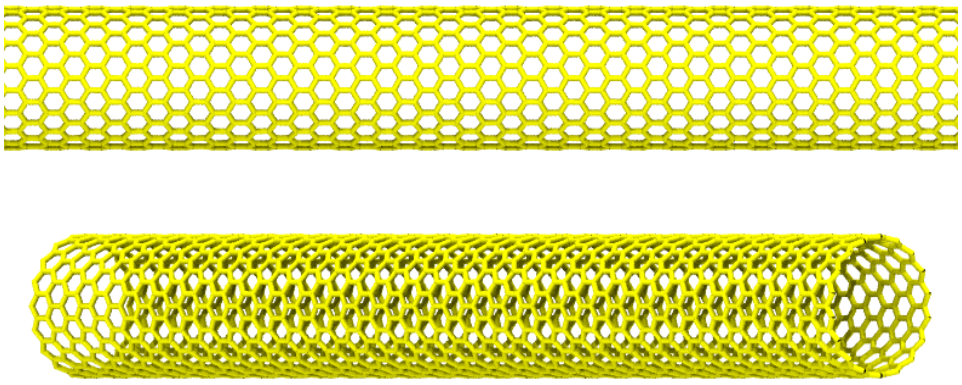


Figure 1.3: A single-walled carbon nanotube. Top image perpendicular to tube axis. Bottom image rotated to show the rolled graphene lattice. Presented is an (18,0) CNT, length 12 nm, radius 0.7 nm.

gives them, rather justifiably, the hype of the material of the future [20].

Structure

Structurally, CNTs belong to the family of fullerenes. These are composed entirely of carbon and form caged structures, spherical for buckyballs [21], and cylindrical for carbon nanotubes (fig. 1.3).

Geometrically, CNTs can be visualised as a product of rolling-up of the honeycomb graphene lattice (fig. 1.4). The chiral vector $\vec{C}$ (blue in fig. 1.4) connects two equivalent points on the graphene lattice. It can be expressed in terms of the basic 2D translation vectors $\vec{a}$ and $\vec{b}$ (red in fig. 1.4) as $\vec{C} = m\vec{a} + n\vec{b}$. The pair (m, n) completely specifies the chiral vector along which the sheet is rolled-up (and which forms the circumference of the CNT). Complementary to the chiral vector $\vec{C}$, the translation vector $\vec{T} = t_1\vec{a} + t_2\vec{b}$ (purple in fig. 1.4) specifies the direction of the tube axis, once rolled. t_1 and t_2 can be expressed in terms of m and n [22].

The chiral vectors specified by a pair (m, m) form *armchair* CNTs (fig. 1.5a), and the vectors $(m, 0)$ form *zig-zag* CNTs (fig. 1.5b). All other tubes all referred to as chiral (fig. 1.5c). The rolling procedure described thus far would produce single-walled

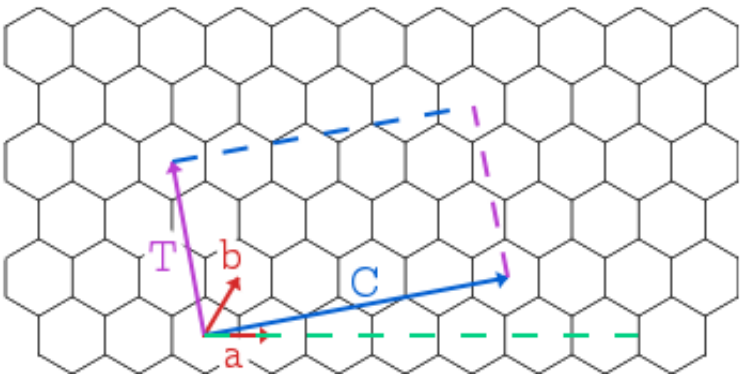
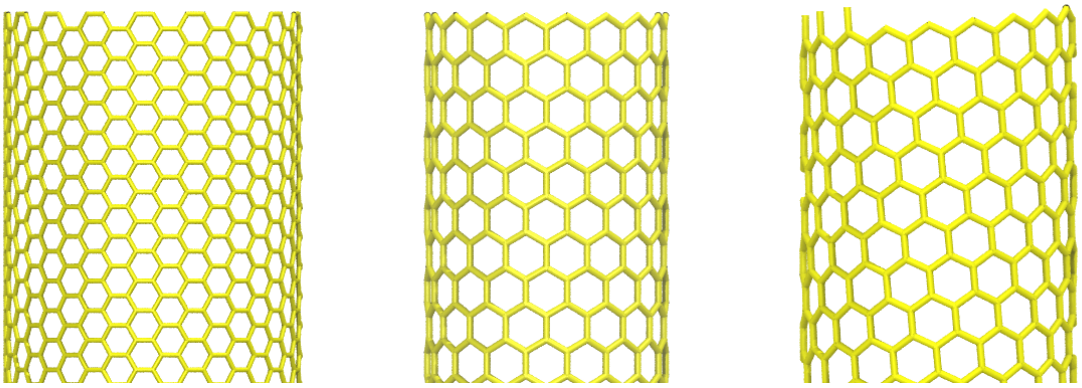


Figure 1.4: Graphene lattice to be rolled into a CNT. Vectors $\vec{a}$ and $\vec{b}$ (red) are the 2D CNT unit translation vectors. Vector $\vec{C}$ (blue) is the chiral vector and $\vec{T}$ (purple) is the unit translation vector along the axis of the resulting CNT. The angle between the green dashed line (the *zig-zag* direction) and the vector $\vec{C}$ is the chiral angle.



(a) Armchair $(18, 0)$ (b) Zigzag $(18, 18)$ (c) Chiral $(18, 32)$

Figure 1.5: CNTs with different chirality. Conventional names and chiral vectors as labelled.

carbon nanotubes (SWNT). Similarly, a bundle of concentric SWNTs, encased in each other, forms multi-walled carbon nanotubes (MWNT). SWNTs tend to have smaller diameters (typically a few nanometres), while MWNTs tend to be thicker (up to a few hundred nanometers), due to multiple carbon shells present. The carbon layers in MWNT are separated by 0.34 nm. In either case, the CNTs have a large length-to-diameter ratio [23], with lengths in excess of micro- or millimetres. Furthermore, the CNTs described so far come in two flavours, depending on closure at each end. One possibility is the open-ended, uncapped type (as in fig. 1.3), and the other is the capped type, created when the carbon atoms form a half-dome structure at either end of the tube.

The picture presented so far describes the conceptual formation of CNTs that is easy to imagine and visualise. In reality, CNTs are not rolled from graphene and need to be synthesised and grown under controlled conditions. One of three methods is typically employed. *Arc discharge* [24, 25, 18, 26] is probably the most common and easiest way to produce CNTs. In this technique, two coaxial carbon rods are placed end-to-end in a chamber filled with an inert gas. A $50 - 100$ A current at $20 - 30$ V is passed between them. Such generated current arc produces a high temperature needed to evaporate

the carbon rods. This technique can produce both SWNT (with catalyst) and MWNT of various sizes. They tend to need further purification. A similar principle is used in the *laser vaporisation* technique [27, 28, 29, 30]. Just as arc discharge, it relies on vaporisation of carbon from solid substrates. In laser vaporisation, the solid target is held in a furnace filled with an inert gas. A laser beam heats and evaporates the carbon substrate, which expands and then cools, forming CNTs. Laser ablation is mostly used to produce SWNTs. The third most common technique is *chemical vapour deposition* (CVD). This is different from the previous two techniques as it does not use a solid substrate for CNT production. Instead, a gaseous source of carbon is used (such as methane or carbon monoxide). An energy source such as a heated coil will convert the carbon source to atomistic carbon, which will diffuse to a catalyst-covered substrate. The technique has been developed further in recent years [31, 32, 33, 34, 35], but the main principle of a catalyst-assisted deposition of carbon from a gaseous source remains the same.

The CNTs thus prepared are usually far from the perfect structures described so far. They usually contain structural defects, are contaminated with catalyst, or mixed with the soot resulting from carbon burning. The resulting CNTs are typically still tangled and need further processing before use (fig. 1.6). This is due to their hydrophobic nature [36, 37, 38, 39], which makes them bundle together in aqueous solutions [39]. They need to be purified and separated before further use. Typical methods involve one or a combination of the following: air oxidation [40, 41, 42], liquid oxidation [43, 44, 45, 46, 47, 48], centrifugation [49, 50], annealing [51, 52, 53], and filtration [54, 55]. Such processing typically functionalises the CNTs [56, 57, 58, 59], which makes them more compatible with aqueous and biological environments.

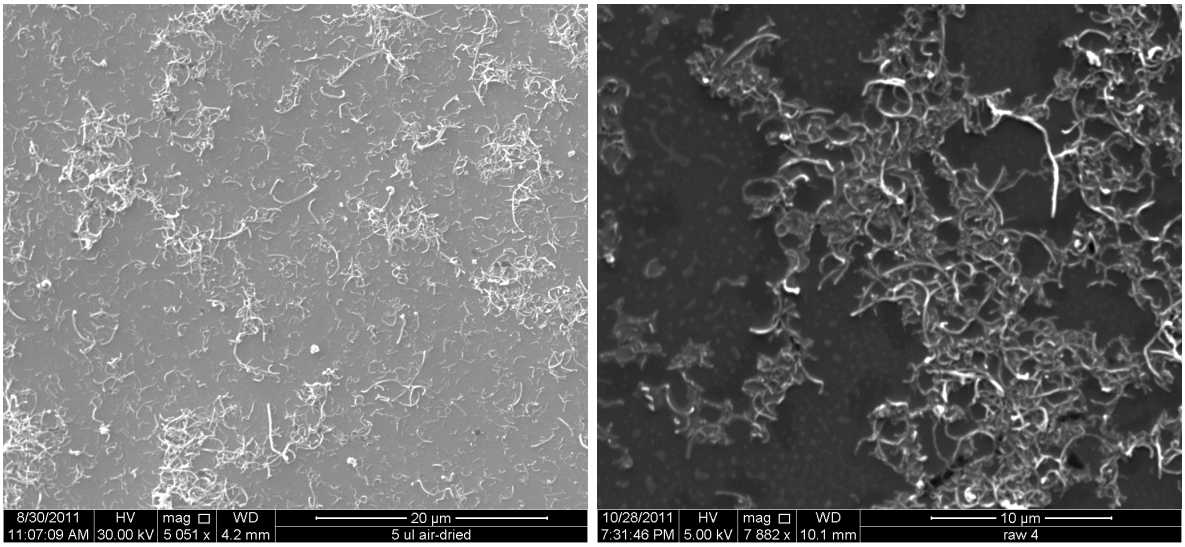


Figure 1.6: Scanning electron microscopy images of raw CNTs (nominal diameter $100 - 150$ nm) solubilised in water and sonicated before deposition. Deviation from straight shape and entangling clearly visible. Scale bar (bottom right corner) on the left image: 20 μm, right image: 10 μm.

Properties

CNTs exhibit a number of unique properties, most important of which are summarised in the following sections.

Electrical properties CNTs have been shown to be either metallic or semiconducting [60]. When the difference between the indices (m, n) of the chiral vector is a multiple of three, the CNT shows a metallic character, otherwise it behaves like a semiconductor with either a small or moderate band gap [60]. There are some deviations from this rule [61], but CNTs generally behave like metals or semiconductors. Crucially, the electrical transport properties of CNTs depend on their size and chirality.

Because of their size and dimensions, the metallic CNTs are excellent conductors. They have been shown to conduct well in the axial direction (much better than copper), while being poor conductors in the lateral direction [62, 63, 64, 65, 66].

Thermal properties CNTs have been shown to be excellent heat conductors [67, 68, 69]. As expected from their electrical transport properties, there is a directionality in the heat conductance. The highest conductivity is observed along the CNT axis [67, 68, 69], while the lateral conductivity tends to be negligible [70].

Mechanical properties Due to their sp^2 bonding between carbon atoms, the CNTs show exceptional strength and are one of the strongest materials known to date [71, 72, 73, 74, 75]. When compressed, they tend to buckle elastically [76], making them robust against mechanical stress and deformation.

Potential applications

Due to their unique properties, CNTs are already finding their way into technological applications [77]. Their current uses include material reinforcement [78], solar cells [79], atomic force microscope tips [80], polymer composites [81], coatings [82, 83], films [84], and energy storage [85].

The future use of CNTs for technological uses depends on many factors, such as growth control, improvements in separation by size and chirality, and purification. Nevertheless, the research into the potential uses in nanotechnology promises exciting developments. These come about in many diverse areas and include water desalination [86], fibres [87], wearable fabrics [88], electronics [89, 90], computer elements [91], medicine [92, 38], chemical sensing [93, 94], and even such remote concepts as the space elevator [95].

Clearly, with any future proliferation of nanotube-based technologies, however promising, the interactions of CNTs with biological environments need to be investigated. In particular, any health implications need to be considered before a widespread use of CNTs can find its way into our homes. The following section describes the current state of knowledge regarding the interactions of CNTs with biological systems, the cells, and the possible use of CNTs as nano-medicines, as well as their potential toxicity.

1.3 CNTs and biological membranes: The story so far

Ever since their discovery, the CNTs have promised elusive applications. They have attracted attention in the field of biomedicine and for various biological applications. There have been issues related to their biocompatibility and toxicity. An overview of the most important aspects of CNTs in biological systems is presented below.

Functionalisation

As prepared, the CNTs are hydrophobic and incompatible with the biological environments. This is due to their graphene-like surface and the tendency to aggregate and bundle together. They need to be functionalised before use in an aqueous environment. This is usually done via attachment, either covalent or non-covalent, or functional groups that render them more hydrophilic.

Covalent functionalisation With this method, functional groups are attached by covalent bonding to the side-walls of the CNTs. This is often a result of the more common purification methods, especially acid washing and chemical oxidation [43, 44, 45, 46, 47, 48]. This method usually cleans but also cuts the CNTs into shorter fragments [44]. Other methods are also in use, but are less common [96, 97, 98]. Surface functionalisation via these methods usually attaches functional groups to sites with increased structural strain or deviations from the hexagonal graphitic lattice (such as defects or the caps at the ends of the CNTs). One of the consequences of covalent functionalisation is CNT surface modification, which can result in the loss of some of the unique properties that depend on structure (e.g. conductivity).

Non-covalent functionalisation Another method of functionalising CNTs is by non-covalent attachment of compatible molecules [99, 100, 101]. Functionalisation with DNA [99, 102], polymers [103], proteins [99], and others [104] has been reported. The

advantage of using this technique is that the underlying CNT structure is not modified, leaving the pristine, hexagonal CNT lattice unchanged.

Biomedical applications

Structural properties, such as the large and regular surface area and mechanical robustness, along with the potential for functionalisation, have attracted attention for use of CNTs in many biologically relevant fields [105].

Functionalising CNTs by attaching various biologically relevant molecules such as peptides [106], proteins [107, 92], nucleic acids [108, 109, 110] and drugs [111] makes them suitable candidates for the next generation vehicles for translocation of these across the cellular membrane. As all the classes of molecules mentioned are too large to cross the cellular membrane [112], functionalised CNTs (*f*-CNTs) appear as attractive delivery agents [113, 114, 115].

A good number of experiments demonstrated a few promising applications of CNTs in biology. By functionalising the CNTs with ligands binding to receptors found on cancer cells, it is possible to deliver targeted treatment and even reduce the tumor growth in mice [116]. Functionalising the CNT with short interfering RNA (siRNA) was shown to successfully silence target genes [117], which promises the use of CNT systems in gene therapy. Due to their specific properties, CNTs can be used for biosensing [118] and imaging. Other possible applications include vaccinations, where the functionalised CNTs induce a strong immune response [119, 106]. The variety of possible applications of CNTs in biological context makes it important to understand their interactions in biological environments.

Membrane insertion

As far as the membrane interaction is concerned, there is no consensus as to the possible bilayer entry and crossing mechanisms [120]. It is widely known the CNTs cross the

cellular barrier easily but the exact mode of entry is not agreed upon. Some literature suggests passive transfer [120], while others claim endocytosis is the most likely entry mechanism [121]. The reality is probably more complex, with a mixture of entry pathways, depending on CNT properties, being likely. Either way, the interaction between CNTs and biological membranes at this basic cell entry point needs closer inspection.

Toxicity

Despite their 'wondrous' properties and potential applications, the use of CNTs may be limited until their toxicity to cells and organisms is fully understood. Despite years of research, there is still uncertainty related to their toxicity. As prepared, CNTs are experimentally reported to be toxic [122, 123, 124, 125, 126, 127, 128]. Functionalised CNTs are widely believed to be less toxic [129, 105].

When considering pristine CNTs, MWNTs tend to be more toxic with increasing diameter [130]. The toxicity of SWNTs tends to be dosage and time dependent [131, 132] and has been reported be higher than for MWNTs [133]. Also, the higher levels of functionalisation tend to produce less toxic SWNTs [134]. Interestingly, CNTs tend to be more toxic than C_{60}, the other member of the fullerene family [133].

The most common mechanisms of toxicity include oxidative stress, altered mitochondrial activity and metabolic routes [105]. Such interactions often cause cell apoptosis, or necrosis [105, 132].

Many of the toxicity studies have been inconclusive, despite the volume of research carried out [129, 105]. CNTs seem to offer no clear-cut answers regarding their toxicity today, more than twenty years after their discovery. A lot of work focuses on specific *f*-CNTs interacting with specific cells. Since that response does vary, it would be beneficial to understand the basic mechanism of CNT-membrane interaction, which could then influence more guided research.

1.4 Perspective

The research in the field of CNT-membrane interaction often involved analysis of how different CNTs (or *f*-CNTs) interact with cells or larger organisms, and focused on the global, macroscopic or mesoscopic picture. Relatively little work has been done to analyse the interaction at the point of entry, or physical contact between CNTs and lipid bilayers, at the molecular level. This work aims to fill this gap by means of molecular dynamics simulations and atomic force microscopy experiments.

Chapter 2 lays out the theoretical and practical basis of the techniques employed.

Chapter 3 investigates the interactions of CNTs with lipid bilayers via molecular dynamics simulations. This is done in a systematic way, under controlled conditions. The hydrophobic character of CNTs is taken into account and the sensitivity of the results to simulation parameters, force fields, and the level of hydrophobicity is examined.

Chapter 4 probes the mechanical properties of the lipid bilayer on contact with the CNT by atomic force microscopy. This is done in a controlled manner. Simulations are designed to mimic the experiment and to provide a bridge between the experimental and simulational perspectives.

Chapter 5 explores the behaviour of shorter CNTs freely interacting with the lipid bilayer. Arrays of CNTs, both inside and outside of the lipid bilayer, are inspected.

Chapter 6 concludes the thesis and suggests future experiments to build on this work.

2 Theory & Methods

Two major techniques were used in this work. The CNT-lipid interaction was investigated computationally with molecular dynamics, and experimentally with atomic force microscopy. Each method, with completely different principles and methodologies, gives insight into processes at different scales (both spatial and temporal), and both can be used to complement each other.

2.1 Molecular dynamics simulations

The solution of a physical problem often requires solving, either analytically or numerically, an appropriate equation describing the behaviour of the system under investigation. For simple systems, analytical solutions are often fairly easy to obtain. For more complicated systems, such as multi-body (or multi-atom) problems, analytical solutions are either unavailable or impractical. The solutions to such problems are often obtained by numerically solving the relevant equations with the aid of computers. Molecular dynamics (MD) simulations are a computer-aided technique of numerically solving the equation of motion for relevant particles [135]. The result of MD simulations is a molecular trajectory describing the development of the system in time. MD trajectories can be used to describe the behaviour of systems at the molecular scale. Such atomistic level of detail is often unavailable experimentally, so MD simulations can provide extra detail of the processes at the molecular scale.

2.1.1 Equations of motion

Solving a full quantum mechanical (QM) equation of motion for a multi-body system can provide the most accurate description of the dynamics of atoms. However, due to the large number of variables, a full QM description of any system but the simplest ones becomes impractical. Current methods allow QM simulations of small proteins, but these require high performance computers and are limited to a few picoseconds at best [136, 137]. Such solutions require solving a full multi-body Hamiltonian, which is not only complicated, due to the number of variables involved, but also computationally expensive. In this work, systems with much larger sizes (tens of nanometers) and processes at longer timescales (nanoseconds) were considered, hence more efficient computational techniques were required.

The Born-Oppenheimer approximation

This approximation [138] states that for a given molecule, the motion of electrons can be decoupled from the motion of the nuclei. This is because, due to their small mass, the electrons will adjust to the motion of the nuclei on a very rapid timescale. The motion of the electrons is therefore much quicker than the dynamics of the nuclei and their dynamics will adjust almost instantaneously to the nuclear configuration. Because most of the mass of an atom is concentrated on the nucleus, its dynamics will determine the position of the entire atom.

Classical description and Newton's equations of motion

Thanks to the Born-Oppenheimer approximation, the motion of electrons can be effectively ignored in the description of the ground state dynamics of a molecule. In fact, most MD simulations ignore the electronic motion and atoms are represented as points (with charge, where appropriate), which act under a potential function $V(\boldsymbol{r_1}, \boldsymbol{r_2}, \ldots, \boldsymbol{r_N})$,

where $\boldsymbol{r_i}$ is the position vector of atom i. The force acting on an atom i under the potential V is given by

$$\boldsymbol{F_i} = -\frac{\partial V}{\partial r_i} \tag{2.1}$$

This can be used to solve the simultaneous equations of motion for N atoms:

$$m_i \frac{\partial^2 \boldsymbol{r_i}}{\partial t^2} = \boldsymbol{F_i} \qquad i = 1, 2, \ldots, N \tag{2.2}$$

Simultaneously solving the above equations for all atoms in the system, in small time steps, results in a description of time evolution of atomic coordinates. Such a trajectory can then be used to analyse the dynamics of the system.

Solving Newton's equations of motion to describe the system implies that *classical* and not *quantum* mechanics holds. This is usually fine for the description of the dynamics of most systems. It does imply that certain quantum mechanical effects, such as tunnelling, are not possible. Because the electronic motion is not considered, any processes involving electrons, such as polarisation, bond-formation, or charge transfer cannot be properly accounted for.

Bonds can be treated as constraints in the potential V of eqn. (2.1) and eqn. (2.2). The set of parameters and potential energy functions used to describe V is called a *force field*. Various concepts related to force fields are described below.

2.1.2 Force fields

As shown in the previous section, knowing the exact form of the potential function V, in which the molecule moves, allows the determination of the dynamics of the molecule in question. In this work, the GROMACS (www.gromacs.org) [139] simulation package was used, and the following sections describe the implementation used therein [140].

Potential functions

For the use in computer simulations, the true potential function V is approximated by simpler functions. These take into account different atom types and various bond interactions. In the simplest form, the potential V can be represented in the following form:

$$V = V_B + V_{NB} \tag{2.3}$$

where V_B and V_{NB} represent the bonded and non-bonded contributions to the potential V, respectively.

Bonded interactions

The bonded interaction V_B is a sum of several contributions:

$$V_B = V_{bond} + V_{angle} + V_{dihedral} + V_{improper} \tag{2.4}$$

These come from the bond (V_{bond}) and angle (V_{angle}) stretching, and dihedral ($V_{dihedral}$, $V_{improper}$) potentials.

Bond stretching is represented by a potential of the form

$$V_{bond}(r_{ij}) = \frac{1}{2} k_{ij}^b (r_{ij} - b_{ij})^2 \tag{2.5}$$

where $r_{ij} = |\boldsymbol{r_i} - \boldsymbol{r_j}|$ is the distance between two atoms i and i, b_{ij} is their equilibrium distance and k_{ij}^b is the force constant. The above equation is a description of a classical harmonic oscillator, which is a good approximation for small bond-stretching.

Other functional forms for bond stretching can also be used, such as a fourth power potential [141], or Morse potential [142]. These are more involved computationally and were not used in this work.

Angle potentials are used to represent the directionality and harmonic vibrations of bonds. For three atoms i, j, k connected by an angle θ_{ijk}, this is represented by:

$$V_{angle}(\theta_{ijk}) = \frac{1}{2} k^{\theta}_{ijk}(\theta_{ijk} - \alpha_{ijk})^2 \tag{2.6a}$$

or, in simpler form:

$$V_{angle}(\theta_{ijk}) = \frac{1}{2} \tilde{k}^{\theta}_{ijk} \left[\cos(\theta_{ijk}) - \cos(\alpha_{ijk})\right]^2 \tag{2.6b}$$

where α_{ijk} is the equilibrium bond angle and k^{θ}_{ijk} (or $\tilde{k}^{\theta}_{ijk}$) is the force constant for the classical harmonic oscillator. In the force fields used in this work [143, 144, 145], the second form of $V_{angle}(\theta_{ijk})$ (eqn. (2.6b)) is used.

Dihedral potentials are used to describe the torsional energy change on bond rotation. For an angle ϕ_{ijkl} between planes i, j, k and j, k, l formed by atoms i, j, k, l, the dihedral energy has the form:

$$V_{dihedral}(\phi_{ijkl}) = \frac{1}{2} k^{\phi}_{ijkl}[1 + \cos(n\phi_{ijkl} - \beta_{ijkl})] \tag{2.7}$$

where β_{ijkl} is the equilibrium angle, n is the multiplicity (to describe the number of minima), k^{ϕ}_{ijkl} is the force constant, and β_{ijkl} is a phase factor.

To maintain the planar structure of certain bonds (especially in ring particles), and to prevent molecules from changing to their mirror images, an *improper* dihedral potential is defined as:

$$V_{improper}(\xi_{ijkl}) = \frac{1}{2} k^{\xi}_{ijkl}(\xi_{ijkl} - \xi_0)^2 \tag{2.8}$$

where ξ_{ijkl} is the angle between the planes i, j, k and j, k, l formed by atoms i, j, k, l,

ξ_0 is the equilibrium angle, and k^{ξ}_{ijkl} is the force constant for this energy term.

Non-bonded interactions

The potential due to non-bonded interactions can be split into two terms:

$$V_{NB} = V_{LJ} + V_C \tag{2.9}$$

where V_{LJ} and V_C denote the Lennard-Jones and Coulomb interactions. These potentials are pairwise-additive, i.e. their values depend on the sum of all of all non-bonded pairs. Each of these depends on a two-body interaction, unlike some of the potentials described in the preceding sections.

Lennard-Jones potential arises due to the effect of Pauli repulsion and van der Waals (VdW) attraction. For two atoms i, j, a distance $r_{ij} = |\boldsymbol{r_i} - \boldsymbol{r_j}|$ apart, the Lennard-Jones (LJ) potential has the form

$$V_{LJ}(r_{ij}) = 4\varepsilon_{ij}\left[\left(\frac{\sigma_{ij}}{r_{ij}}\right)^{12} - \left(\frac{\sigma_{ij}}{r_{ij}}\right)^{6}\right] \tag{2.10}$$

where σ_{ij} is the distance at which the potential vanishes, and ε_{ij} is the depth of the energy well at the minimum $r_{min} = 2^{1/6}\sigma_{ij}$.

The first term ($\propto r^{-12}$) in eqn. (2.10) arises due to Pauli repulsion and the second term ($\propto -r^{-6}$) is due to the attractive van der Waals interaction. The parameters ε_{ij} and σ_{ij}, defining the energy well depth and equilibrium separation, respectively, depend on particular types of atoms interacting via this potential.

The LJ potential can also be represented in a simpler, and more computationally effective form:

$$V_{LJ}(r_{ij}) = \frac{C_{ij,12}}{r_{ij}^{12}} - \frac{C_{ij,6}}{r_{ij}^{6}} \tag{2.11}$$

Where parameters $C_{ij,12}$ and $C_{ij,6}$ are provided in the force field.

Coulomb interaction is described by the standard potential:

$$V_C(r_{ij}) = \frac{q_i q_j}{4\pi\epsilon_0\epsilon_r r_{ij}} \tag{2.12}$$

where all symbols have their usual meaning, i.e. q_i, q_j are the charges on atoms i, j separated by a distance $r_{ij} = |\boldsymbol{r_i} - \boldsymbol{r_j}|$, ϵ_r is the dielectric constant, and ϵ_0 is the permittivity of free space.

Atom representations

Thus far, a methodology for MD simulations has been described in terms of force field potentials and parameters that define the behaviour of atoms. These are generally good approximations to real potentials and are computationally efficient. The force field potentials provide a layer of abstraction connecting complicated, real systems and their dynamic computer representations. These approximations are simplifications, with certain assumptions made in their derivation and parametrisation. The first simplification was provided by the Born-Oppenheimer approximation, which made it possible to describe the motion of molecules in terms of dynamics of atomic nuclei forming these molecules. With appropriate force field parametrisation, such systems can be used to describe the movement of real molecules. Such representations of atoms provides another layer of abstraction used in computer simulations.

Without the loss of generality, different atom representations can be used in different force fields, along with accordingly parametrised potentials to describe the dynamics of the systems of interest. In the situation described so far, an atom in a molecule was represented by a point with a charge. No electrons were considered. Force fields that use such representations are called *all-atom* force fields, as every atom in the system is

represented by an MD 'atom'. This provides an abstraction in the atom representation. For examples of such force fields, see [146, 147, 148, 149, 150, 151, 152].

Another type of representation is one where all heavy atoms are represented, except the non-polar hydrogens. These are bundled with larger atoms, thus forming 'united-atoms'. This saves the computation of the dynamics of hydrogen atoms, which, due to their small mass, do not contribute significantly to the dynamics of heavier molecules. Such atom representations are used in *united-atom* force fields [141].

A step further is the realm of *coarse-grained* (CG) force fields [143, 153, 154, 144, 145], where a few heavy (i.e. not hydrogen) atoms are packaged together to form an abstract CG 'atom', or 'bead'.

In this work, only CG force fields were used and they are described in more detail in the following section.

2.1.3 Coarse-grained force fields

Computer simulations can give a lot of insight into molecular interactions. However, the typical all-atom simulations suffer from limited spatial and temporal resolution due to the large number of interactions involved, which require a lot of computing power to deal with. CG methodology tries to address that by reducing the total number of particles interacting [143, 144, 145, 153, 154, 155].

In this work, two force fields were used: MARTINI2 (MARTINI version 2.1, based on the original MARTINI [144], referred to as MARTINI2 in this thesis) [145], and a locally developed 'Bond' force field [143]. Since the Bond force field is based on the MARTINI methodology with refined parameters, and MARTINI2 is an extension of the earlier version, the methodology used in MARTINI is described here. Another CG representation was suggested by the Klein group [153, 154]. It provided a different atom mapping scheme ('coarse-graining') and was not used in this thesis.

In MARTINI, the CG sites represent clusters of (roughly) four heavy (i.e. non-hydrogen) atoms. Each cluster has the mass of 72 amu, equivalent to four water particles. This convention drastically reduces the number of coordinates in a system. For example, a united-atom representation of the DPPC lipid is composed of 50 sites [156], which in MARTINI representation is reduced to 12 CG beads [144]. A chemical full formula for DPPC ($C_{40}H_{80}NO_8P$) contains 130 atoms. It shows how the CG representation significantly reduces the number of degrees of freedom in the system.

The resulting interaction potential V_{CG} is much 'smoother' (with fewer spikes and therefore more continuous derivatives) than the equivalent atomistic potential [155]. This is due to the larger size of CG beads [145]. The resulting friction is also reduced [145]. This allows the use of time steps (~40 fs) that are larger than for atomistic simulations (~2 fs), which additionally speeds up the simulations.

In MARTINI, the CG beads are divided into a few categories. There are the polar (P), non-polar (N), charged (Q), and apolar (C) particles. Additionally, the N and Q types are subdivided depending on their chemical nature and hydrogen bonding capabilities. N0 has no hydrogen bonding capability, Nd and Na can act as hydrogen bond donor or acceptor, and Nda can be either a hydrogen bond donor or acceptor. Same subtyping applies to the Q type.

Altogether, there are 10 particle types in MARTINI. These types can interact at five energy levels (ε_{ij} in eqn. (2.10)). Type P represents molecules that would dissolve in water (in fact, water in MARTINI is of type P). Type C represents hydrophobic molecules, such as butane or lipid hydrophobic tails. Type N represents mixed polar/apolar groups and type Q is reserved for charged particles or groups.

The Bond force field uses the same scheme for the potential parametrisation but the exact parameters are slightly modified [143].

MARTINI2 is the newer, or improved, version of MARTINI. The same coarse graining

methodology is used (i.e. four heavy atoms form a CG bead). The particle types (P, N, Q and C) are as before. N and Q types are subtyped as before (-0, -a, -d, -da). Particles P and C are, however, split into five subtypes each. C type is now divided into C1...C5 categories, where C1 is the most hydrophobic subtype (lipid tails in DPPC are of type C1). Type P is also split into five subcategories P1...P5, where P5 is the most hydrophilic type. Water is of type P4. A few other particle types were also introduced but they were not used in this work.

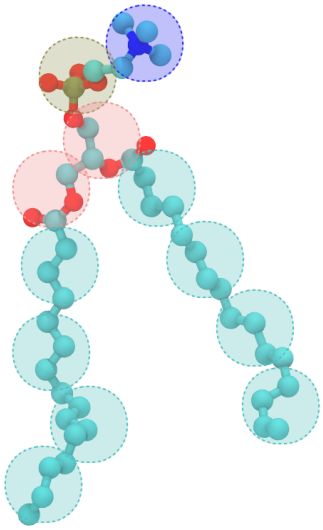
Altogether, there are now 18 particle types in MARTINI2. They interact at 10 different energy levels, instead of 5 as was the case in MARTINI. This new force field is more fine-tuned than the earlier version. While the authors do provide a conversion scheme from 'old' to 'new' particle types and energy levels, some type mixtures may result in a multiple possible type assignment. This is addressed in more detail in chapter 3.

Lipid and CNT representation

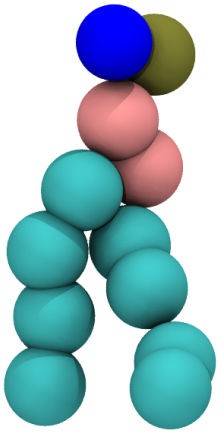
The CG representation of a DPPC lipid is shown in fig. 2.1 a-b. This is a standard DPPC lipid as parametrised in MARTINI/MARTINI2 and no changes were made to this representation.

A CNT model used in this work is shown in fig. 2.1 c-e. The mapping from atomistic (fig. 2.1c) to CG representation (fig. 2.1e) was done using a 4-to-1 scheme as in the original MARTINI model. This mapping preserves the hexagonal symmetry of the CNT. Particular CG bead types used are described in the relevant chapters.

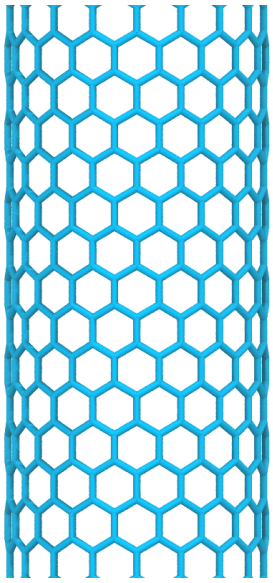
No charged groups were considered at the CNT walls or the open ends in the case of uncapped CNTs. It would be much more instructive to have a representation of the π-electrons on the CNT walls. This was not possible with the CG force fields, where structural detail at this level is not considered. Such information would give much more insight into the interaction than chance charged groups.



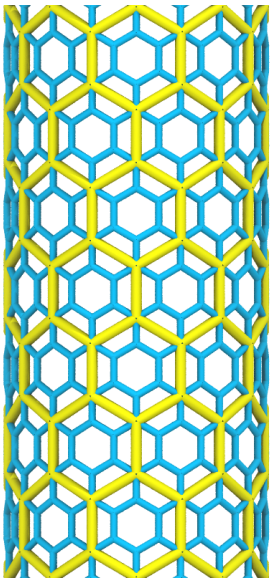
(a) Atomistic representation



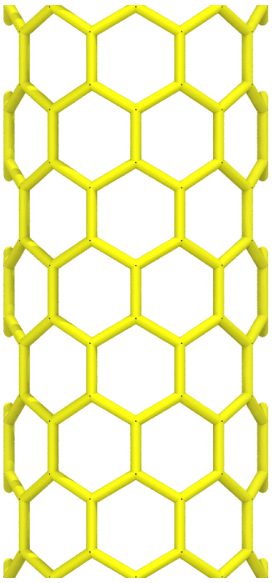
(b) CG representation



(c) Atomistic representation



(d) Combined view



(e) CG representation

Figure 2.1: Comparison of DPPC and CNT representations in atomistic and CG force fields. DPPC lipid in (a) atomistic (united-atom), and (b) CG representation. The circles in (a) show the mapping used to translate the atomistic to CG representation. (c)-(e) Comparison of various CNT representations. Shown are: (c) blue atomistic, and (e) yellow CG representations of CNT. Subplot (d) shows a combined view for easier comparison. Lines represent bonds between atoms (c, d) and CG 'beads' (d, e). Atoms themselves not shown for clarity - they are located at the intersection points of the bond lines.

2.1.4 Algorithms

A general scheme to proceed with a simulation (after the system has been set up) can be summed up in three steps:

1. Energy minimisation
2. Equilibration
3. Production run

The first step removes the unrealistic or unphysical forces that may arise in the system during set up. These usually come about due to placing molecules too close to each other, which results in unusually high force that would crash the simulation (as the particles would start moving too far under such high forces).

The equilibration and production run employ the same MD algorithms but their purpose is slightly different. Equilibration is essentially a short production run. It is used to make sure the energy of the system reaches an equilibrium, removing any remaining unbalanced forces that haven't been evened out during energy minimisation. Additional position restraints are often applied during equilibration to ensure the molecules maintain their desired positions for the start of the 'proper' production run. After the shorter equilibration run it is possible to investigate if the system behaves in a sane, or expected, way and no set up mistakes have been made.

During the production MD run, the system is run for longer periods, allowing the molecules to interact. A number of algorithms are employed for this and they are described in the following sections.

Energy minimisation

There are a few energy minimisation algorithms available in GROMACS and *steepest descent* was chosen for this work.

During energy minimisation, the forces and energies are computed for all particles in the system. The particles are then moved to their new positions $\boldsymbol{r_{n+1}}$ according to [140]:

$$\boldsymbol{r_{n+1}} = \boldsymbol{r_n} + \frac{\boldsymbol{F_n}}{\max\left(|\boldsymbol{F_n}|\right)} h_n \tag{2.13}$$

where $\boldsymbol{F_n}$ is the force acting on particle n, $\max\left(|\boldsymbol{F_n}|\right)$, and h_n is a predefined maximum displacement. If the potential calculated for some particle is lower than before, then the new position is accepted and h_n increased. Likewise, if the potential is higher than before, then the new position is rejected and h_n is decreased. This essentially moves a particle along the line of the steepest descent of the potential (the highest force) and helps it reach a lower energy state as defined by the potential V described in earlier sections. Energy minimisation is stopped after no forces higher than a threshold value are present (or a maximum number of iterations is reached).

Molecular dynamics

The MD algorithm starts with loading the energy minimised system, and from that atom positions and velocities are read (if no velocities are supplied, then they are generated randomly for each atom according to the Maxwell-Boltzmann distribution [140]). Next, the following steps are iterated [140]:

1. Compute forces

   From the atom positions and potentials described in the force field, forces on atoms are calculated. This includes the non-bonded two-body interactions and the bonded two-, three-, and four-body interactions (see chapter 2.1.2).

2. Update atom positions

   Using the calculated forces, integrate Newton's equations for each atom and update positions accordingly

Integration algorithm The default integrator used in GROMACS is the *leap-frog* algorithm [157]. It uses the positions $\boldsymbol{r}$ at time t and velocities $\boldsymbol{v}$ at time $t+\frac{1}{2}\Delta t$ to calculate the new particle positions and velocities according to:

$$\boldsymbol{v}(t+\frac{1}{2}\Delta t) = \boldsymbol{v}(t-\frac{1}{2}\Delta t) + \frac{\Delta t}{m}\boldsymbol{F}(t) \tag{2.14a}$$

$$\boldsymbol{r}(t+\Delta t) = \boldsymbol{r}(t) + \Delta t\boldsymbol{v}(t+\frac{1}{2}\Delta t) \tag{2.14b}$$

which is identical to the Verlet algorithm [158]:

$$\boldsymbol{r}(t+\Delta t) \approx 2\boldsymbol{r}(t) - \boldsymbol{r}(t-\Delta t) + \frac{\Delta t^2}{m}\boldsymbol{F}(t) \tag{2.14c}$$

where $\boldsymbol{F}(t)$ is the force at time t and Δt is the time step. This algorithm has the advantage over the Verlet algorithm in that it introduces smaller errors in velocity and less numerical imprecision [159].

Periodic boundary conditions Any system used for an MD simulation is essentially a contained, finite box with definite boundaries. This could lead to artifacts at the edges, where solvents could evaporate and unrealistic forces could arise [140]. This problem is circumvented by using periodic boundary conditions. In short, translated copies of the simulation box are placed around it. This way a continuous, 'infinite', bulk system is mimicked. A molecule disappearing off one edge of the box appears on the other side of it. This can introduce other artifacts, such as a self-correlation of dynamics, but these are usually quite insignificant compared to the alternative of not using any periodic boundaries. This effect scales with the size of the simulation box, so for large systems becomes negligible.

In this work, full periodic boundary conditions in all three directions xyz were used.

The only exceptions were simulations in chapter 4, where a slightly different method was adapted, as described therein.

Bond constraints For a given integrator, the time step Δt depends on the fastest motion in the system. For a biomolecular simulations, bond vibrations would be the fastest motion, about an order of magnitude faster than translational motions [160]. By treating bonds as rigid, these motions can be eliminated, and the effective integration step Δt increased. Such bond constraining was implemented using the LINCS scheme, where bond lengths were reset to their correct values after an unconstrained update [161].

Cut-offs and treatment of electrostatics In a MD simulation, ideally, all interactions between all the atom pairs should be included. It turns out that this is not the most efficient way of doing simulations due to the large number of non-bonded interactions decaying with distance. There are a number of ways of treating these interactions.

In this work, following the spirit of MARTINI, for each particle, a neighbour list is constructed (and updated every few MD steps). This limits the interactions to a certain cut-off distance r_{cutoff} [140]. All interactions are then accounted for within that group. A sharp cut-off in the value of potentials can introduce errors in the long range forces and create artifacts at the cut-off [162, 163]. These are usually not very severe for LJ interactions, due to their quick decay with distance.

More care needs to be taken with electrostatic interactions. In MARTINI, this situation is corrected by shifting the Coulomb interaction continuously from the particle centre at $r = 0$ to $r = r_{cutoff} = 1.2$ nm [140, 144, 145]. For the LJ interaction, the potential is shifted between $r = 0.9$ nm and r_{cutoff}. This is done to ensure the potentials and their derivatives are continuous at boundaries. This methodology was adopted to speed up the neighbour list search, which in turn gives an overall speedup of the simulations. This, however, has the drawback of mimicking the effect of distance-dependent

screening [145, 164].

A proper treatment of electrostatics requires taking into account the long range interactions, which are slow to converge beyond the cut-off. To do that, methods like Ewald summation, or Particle Mesh Ewald (PME) can be adopted [160]. The idea behind these is that the electrostatic potential energy V_C can be split into two sums and a constant [140]:

$$V_C = V_{direct} + V_{reciprocal} + V_0 \tag{2.15}$$

where V_C is the Coulomb potential, which is split into a direct sum V_{direct} and a sum in the reciprocal Fourier space $V_{reciprocal}$. V_0 is a constant. By using this approach, one slowly converging sum of long-range interactions is split into a sum of two quickly converging interactions, weighed by the error function: V_{direct} is the Coulomb potential, converging quickly in the real space, and $V_{reciprocal}$ is a Fourier sum, converging quickly in the reciprocal space.

Ewald summation, or PME were not used in this work as the MARTINI force field was parametrised using shift functions, and changing the treatment of electrostatics without re-parametrisation could lead to systematic errors.

Temperature and pressure coupling Using molecular dynamics as described would lead to an NVE ensemble (constant number of particles N, constant volume V and energy E), while the experiments are carried out under constant temperature and pressure. To achieve an NPT ensemble (constant number of particles N, pressure P and temperature T), the temperature and pressure of the simulation box need to be controlled. This is because both quantities can drift due to integration errors, or heating due to external forces or constraints. In this work, the Berendsen thermostat [165] was used, where the

temperature is scaled according to:

$$\frac{\mathrm{d}T}{\mathrm{d}t} = \frac{T_0 - T}{\tau_T} \tag{2.16}$$

where T is the current temperature of the system, T_0 is a reference temperature of the external bath, and τ_T is a time constant. This mimics coupling the system to an external heat bath. The temperature adjustment is done by scaling the velocities of all particles in the system by a parameter λ, which is close to unity.

The Berendsen thermostat has the advantage of tuning the temperature scaling via the decay time τ_T in the exponent. This can be useful for different stages of the simulation (e.g. equilibration, production run), where the influence on the system dynamics and approach to equilibrium can be simply adjusted. This thermostat does not, however, generate a correct thermodynamic ensemble (by suppressing the fluctuations in kinetic energy via velocity rescaling).

Alternative methods, such as the velocity rescaling [166], or the Nosé-Hoover thermostats [167] can be employed to generate more accurate thermodynamic ensembles.

Similarly, the pressure of the system in this work was maintained by the Berendsen pressure coupling scheme, where the pressure is adjusted according to [165]:

$$\frac{\mathrm{d}P}{\mathrm{d}t} = \frac{P_0 - P}{\tau_P} \tag{2.17}$$

where P is the pressure, P_0 is a target pressure value, and τ_P is a time coupling constant. The pressure coupling is done by rescaling the box vectors of the system and readjusting the coordinates of the particles accordingly. This leads to slight box size variation during the simulation.

In this work, the pressure coupling was anisotropic, with separate coupling in the x-y plane (the lipid bilayer plane) and the z-direction, and was carried out using the

methodology from GROMACS [140]. Temperature coupling was done separately for the lipids, CNT and the solvent to keep all the components of the system at a constant temperature (323 K). τ_P was set to 10 ps, and τ_T was 2 ps, which were large enough compared to the time step used (40 fs = 0.04 ps) to ensure weak coupling.

2.2 Software

All the simulations for this project were run using GROMACS 4+ [139] (particular versions indicated in individual chapters). Analysis of simulation data was done using own code written in Python with MDAnalysis [168], and Perl. Experimental data and curve fitting was done in MATLAB.

Visualisations and simulation snapshots rendering was prepared in VMD [169] and Tachyon [170]. All data plots were prepared using gnuplot [171].

This document was typeset in LaTeX, using KOMA-Script.

2.3 Atomic force microscopy

2.3.1 Overview

The atomic force microscope (AFM) is one of the tools used to measure surface-probe interactions. One of the first such tools was the surface force apparatus (SFA) [172, 173], which measured the forces between two molecularly smooth surfaces. The forces were measured over a relatively large contact area (tens of micrometers [174]) and could not be used to determine detail at the molecular scale or probe local changes of the sample.

A first step towards atomic resolution came with the scanning tunnelling microscope (STM) [175], which was a precursor to all scanning probe microscopes, including the AFM. The STM utilises the idea of quantum tunnelling. A sharp, conducting probe is

brought into close proximity of a sample and a bias voltage is applied between them. The resulting tunnelling current depends on the local electron density of states and can be used to provide topographical information about the sample. One of the obvious drawbacks of this method is that both the probe and the sample have to be conducting, which limits the use of STM with biological samples.

The AFM [176] could be thought of as a descendant of the STM, as it relies on similar principles. It uses a sharp probe [16] that is brought to close proximity of the sample. The probe is a cantilever beam, which can bend (following Hooke's law $F = kz$) in response to the forces, at the atomistic scale, between the probe and the sample. Measuring the deflection of the probe allows accurate measurement of topographical features of the sample and the forces experienced by the probe. Because the probe is much smaller (typical radius $10 - 40$ nm) than that in the SFA, *local* surface properties can be measured. The AFM can be used in liquid, which enables the use of it for the investigation of biological samples in their native environments. Near atomistic resolution can be achieved with the use of AFM [177]. A resolution of ~5 Å laterally and ~1 Å vertically is routinely available for biological samples [178]. This can depend on many factors, including tip-sample forces, compliance and separation, as well as tip size, shape and thermal vibrations [179, 180, 181].

2.3.2 Principles of operation

On a basic level, the AFM consists of a sharp probe that is scanned across a sample, a detection system used to track the motion of the probe, and a feedback loop to control this motion.

The AFM probe consists of a sharp tip, mounted on a cantilever beam (fig. 2.2). The tip is a micro-fabricated spike, usually rounded at the very end due to processing, with a typical radius of curvature of $10 - 40$ nm. The very end of the tip is the 'sensing' part,

interacting with the sample, and experiencing the tip-sample interaction forces. The tip is typically made of silicon or silicon-nitride, and can often be coated in e.g. gold or platinum, which can be useful for further functionalisation. As it is just the very end of the tip that is responsible for the interaction with the sample, such functionalisation can be used to investigate the interactions of the sample with various materials, or functional groups [182].

The AFM tip is mounted on a cantilever beam. The beam deflects in response to the force experienced by the tip. This deflection is governed by Hooke's law $F = kz$, where F is the force, k is the spring constant of the beam and z is the deflection, in the vertical direction, perpendicular to the sample. The cantilever spring constant k

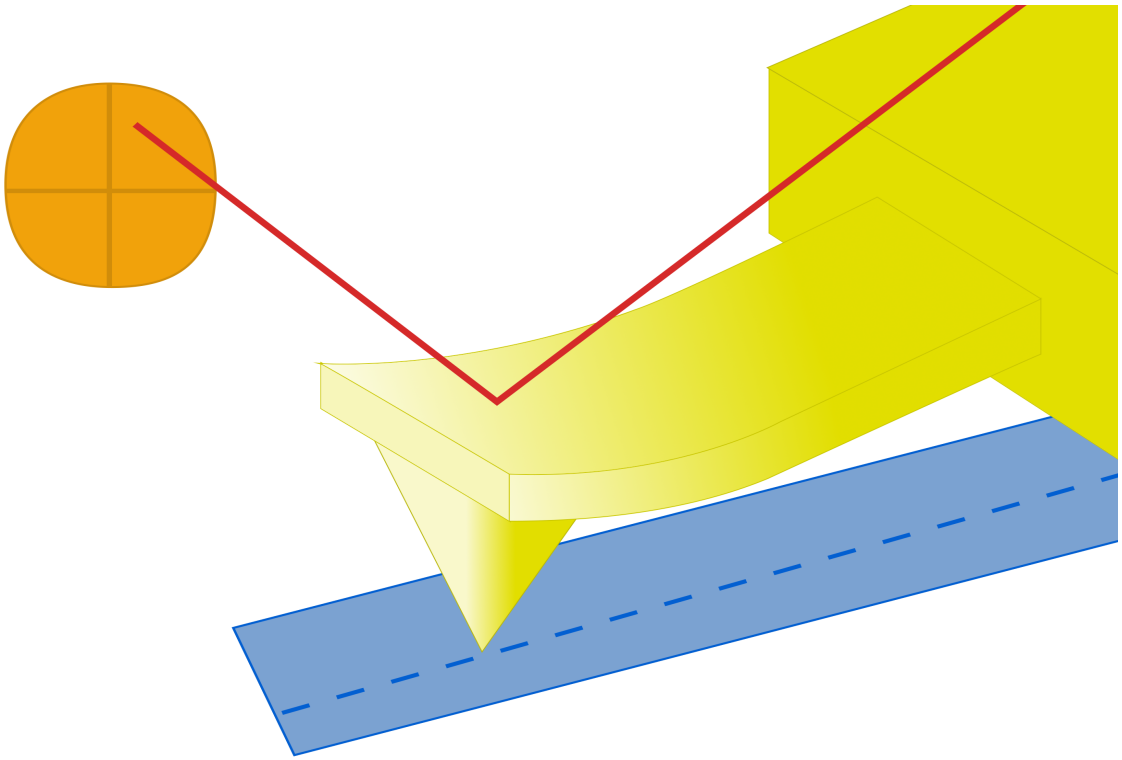


Figure 2.2: AFM cantilever in operation. The cantilever beam, with its mounting chip and the AFM tip shown in yellow. Sample shown in blue. Blue dashed line represents the scan line direction. Photodiode shown in orange, laser beam in red. While scanning the sample (blue dashed line), the cantilever beam deflects, which results in the laser beam (red) reflecting at a different angle. This beam falls onto the photodiode (orange), which registers this deflection and collects the signal for further processing.

is determined by the geometry of the beam, as well as its material properties. The geometry of the cantilever (its width, thickness, length as well as the overall shape) also determines its resonant frequency, which is important for the tapping mode operation (see further section). A typical cantilever, mounted on its chip, would typically fit into a box drawn around the word AFM.

The deflection of the cantilever is measured by an optical detection system [183, 184]. A laser beam is reflected from the rear surface of the cantilever, and falls onto a photodetector, consisting of position-sensitive photodiodes (fig. 2.2). This converts the intensity of the detected laser beam into voltage, which is the primary signal coming from the AFM. This voltage is then converted to a cantilever deflection and used as input of a feedback system which controls the tip position, maintaining various parameters constant, depending on operation mode (see chapter 2.3.4). In either mode, the tip position is adjusted by applying voltage from the feedback system to a piezoelectric element, which can expand or contract in the presence of a bias voltage [185]. Such a piezoelectric material lies at the heart of every AFM system as it allows rapid change of the position of the sensing tip with respect to the sample.

2.3.3 Tip-sample interaction

Tip-sample interaction forces are fundamental in the AFM sensing mechanism. These forces can be broadly divided into two classes of non-contact and contact regimes. Both categories are described below.

Non-contact regime

Electrostatic forces arise when the tip or the sample surface is charged. The electrostatic contribution to the total force experienced by the tip is given by the Coulomb

force between two (point) charges q_1, q_2, a distance d apart.

$$F = \frac{q_1 q_2}{4\pi\epsilon\epsilon_0 d^2} \tag{2.18}$$

where ϵ is the permittivity of the medium. This situation is modified slightly in liquids, as described in a following section.

Van der Waals (VdW) forces come about in a situation where two non-charged molecules (or surfaces) are brought together and interact via the dipole moments induced by the presence of the other particle. There are three components to the VdW forces [16]. Firstly, the *orientation* forces, which arise when two polar molecules (with permanent dipole moments) interact. Secondly, the *induction* forces, which arise when a polar molecule *induces* a dipole moment on another molecule and the two interact via dipole-induced dipole interaction. Lastly, the *London dispersion* forces [186], the major contribution to the VdW force, which have their origin in the quantum mechanical nature of atoms, whereby the electrons in one atom will induce an intermittent dipole (or higher multipole) moment on a neighbouring atom. Such interacting dipoles will give rise to an overall attractive force.

The VdW force between a surface and a sphere (which is a good approximation to the AFM tip-surface system) is given by [16]:

$$F = \frac{HR}{6d^2} \tag{2.19}$$

where R is the sphere (tip) radius, H is the Hamaker constant and d is the distance between the tip and the surface. The VdW force between similar particles in a medium is usually attractive [16].

Electric double-layer forces When surfaces are immersed in liquid, there is usually a build-up of charge at the interface. The major contributions to this surface charging are the ionisation of surface groups and the adsorption of ions from the solution onto the surface [16]. To balance this surface charge, there exists a region of oppositely charged ions in the vicinity of the surface. Some of those ions are (transiently) bound to the surface (this is known as the *Stern* layer), and others form a diffuse cloud of ions around the surface. Together, this is known as the electric *double-layer* (fig. 2.3).

For small potentials ≤ 25 mV, the Grahame equation for the surface charge [187] simplifies to

$$\sigma = \epsilon\epsilon_0\kappa\psi_0 \tag{2.20}$$

where σ is the surface charge density, ψ_0 is the surface potential, and κ is related do a characteristic length of the diffuse layer $\lambda_D = 1/\kappa$, known as the *Debye length*. Further, for a 1:1 electrolyte (e.g. NaCl), for low potentials, as above, the solution for the potential away from the surface is approximated by the *Debye-Hückel* equation [188]:

$$\psi = \psi_0 e^{-\kappa z} = \psi_0 e^{-\frac{z}{\lambda_D}} \tag{2.21}$$

where ψ is the potential at distance z away from the surface, ψ_0 is the potential at the surface as in eqn. (2.20) and λ_D is the Debye length.

The magnitude of the Debye length λ_D depends only on the properties of the elec-

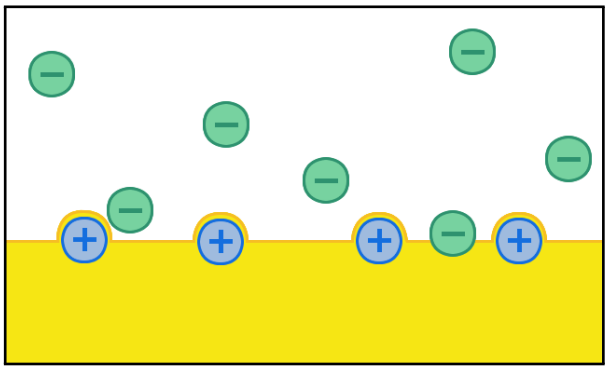


Figure 2.3: Electric double layer. Yellow represents the surface, the surface charge ions are shown in blue. Green ions come from the solution. Some of those are bound or physiorbed to the surface (known as the *Stern layer*), while others form a diffuse atmosphere around the surface.

trolyte solution, and not surface properties of the sample. Importantly, λ_D decreases in the presence of divalent ions but can be approximated by

$$\lambda_D = a/\sqrt{[\text{electrolyte concentration in mol/l}]} \tag{2.22}$$

where $a = 0.304$ for a purely monovalent (1:1) electrolyte (e.g. NaCl), $a = 0.176$ for a purely 1:2 or 2:1 electrolyte (e.g. $CaCl_2$), and $a = 0.152$ for a 2:2 electrolyte (e.g. $MgSO_4$).

Strictly speaking, eqn. (2.21) is a solution for a 1:1 electrolyte case. However, it becomes an approximate solution for any other solute if ψ_0 is small.

DLVO theory The combination of VdW and electric double-layer forces fit into the larger picture via the DLVO theory (after its inventors Derjaguin, Landau, Verwey and Overbeek). It effectively combines the electric and VdW interactions into a unified force in a liquid medium. The DLVO theory [16] is a good approximation to experiments, despite its assumptions such as the smearing out of charges, treating ions as point charges, ignoring image charges and treating the solvent as a continuum. Despite that, the theory is a good description of the forces down to a few nanometers (the order of λ_D) from the surface, when other, non-DLVO, interactions such as hydration or solvation forces come into play. The theory itself, as opposed to its individual components, is not used in this work. It does, however, show that the described effects fit into a larger context and are a part of a more comprehensive description of interactions down to the nanometre scale.

Solvation forces When liquid molecules approach a surface, the properties of the liquid start to differ from those observed in the bulk [16]. In particular, the layering of molecules near a surface will usually occur [189, 190]. This results in oscillatory density profiles, where structured layers of molecules are separated by regions of lower density. The

interactions arising from such ordering are the *solvation* forces (or *hydration* forces if the liquid is water). They typically extend a few molecular diameters into the liquid [189]. The resulting force is typically oscillatory or monotonically increasing, depending on the regularity of the liquid [16]. Either way, the resulting force is larger than the DLVO interaction at small distances to the surface or hard-wall.

Contact regime

The forces described so far applied to situations when the tip and the sample were still a distance d apart. With the AFM, it is possible to press the probe onto the surface of the sample, bringing the two into mechanical contact. The deformation of the interacting bodies at a microscopic scale has been described by a number of theories. Presented below is a summary of the most common ones.

Hertz theory Proposed by Hertz [191], this is the earliest description of a mechanical contact of two elastic bodies. The indenter is assumed to be a smooth elastic sphere, and the sample is assumed to be rigid, flat, and semi-infinite (i.e. the sample thickness is much larger than the radius of the indenter sphere). This theory ignores surface forces and adhesion. The total deformation (indentation) δ, and the contact radius a are given by

$$\delta = \frac{a^2}{R} = \frac{F}{Ea} \tag{2.23a}$$

$$a = \sqrt[3]{\frac{RF}{E}} \tag{2.23b}$$

where R is the tip radius, F is the loading force and E is the reduced Young's modulus (i.e. 'stiffness') [192] of the sample. δ can be assumed to be the indentation of the sample in a situation where it is much more compliant than the indenter, as is the case

for an AFM tip and a biological sample. The reduced Young's modulus is given by:

$$\frac{1}{E} = \frac{3}{4}\left(\frac{1-\nu_s^2}{E_s} + \frac{1-\nu_i^2}{E_i}\right) \tag{2.24}$$

where ν_s, E_s are the Poisson's ratio and Young's modulus of the sample, and of the indenter (ν_i, E_i) [192].

The Hertz theory is most applicable to situations where high loads and low surface forces can be assumed. Similar to the Hertz theory is the Sneddon analysis [193, 194], where the indenter is a rigid punch. Together they can accurately describe the total deformation of the indenter-sample system.

In a situation where the surface forces need to be considered, one of a few other theories can be used to describe the indenter-sample interaction.

The DMT theory Named after its inventors, the Derjaguin-Müller-Toporov (DMT) theory [16, 195] is similar to the Hertz description, but this time the forces between the indenter and sample are also considered. Importantly, adhesion is included. The corresponding expressions for indentation δ and contact radius a are given by:

$$\delta = \frac{a^2}{R} \tag{2.25a}$$

$$a = \sqrt[3]{\frac{R}{E}\left(F + 2\pi R W\right)} \tag{2.25b}$$

where W, the adhesion work, is related to the adhesion force F_d via:

$$F_d = 2\pi R W \tag{2.25c}$$

where all the symbols have the same meaning as in eqn. (2.23). In the case of no adhesion ($W = 0$), eqn. (2.25) reduces to eqn. (2.23), the Hertz description. In the DMT theory,

there is a finite contact area even at zero external load $F = 0$ (eqn. (2.25b)). This is related to the presence of the external forces mentioned earlier.

While the DMT theory incorporates adhesion, it is best suited for systems with low adhesion and small tip radii [196].

The JKR theory Similar to the DMT theory, the Johnson-Kendall-Roberts (JKR) theory [197, 16] considers interaction forces, but only within the contact area. The resulting description of the interaction is given by:

$$\delta = \frac{a^2}{R} - \frac{2}{3}\sqrt{\frac{6\pi W a}{E}} \tag{2.26a}$$

$$a = \sqrt[3]{\frac{R}{E}\left[F + 3\pi RW + \sqrt{6\pi RWF + (3\pi RW)^2}\right]} \tag{2.26b}$$

$$F_d = \frac{3}{2}\pi RW \tag{2.26c}$$

where all the symbols have the same meaning as before (eqn. (2.23) and eqn. (2.25)).

This theory is most suitable for soft systems with large tip radii and high adhesion [196].

The Bradley model In this analysis [198, 196], two rigid spheres interact via the Lennard-Jones potential, resulting in a force

$$F(d) = \frac{8\pi WR}{3}\left[\frac{1}{4}\left(\frac{d}{d_0}\right)^{-8} - \left(\frac{d}{d_0}\right)^{-3}\right] \tag{2.27a}$$

where

$$\frac{1}{R} = \frac{1}{R_1} + \frac{1}{R_2} \tag{2.27b}$$

and R_1 and R_2 are the radii of the spheres and d_0 is their equilibrium separation.

The Maugis theory This model [199], following the Dugdale theory [200], describes a range of material properties by the parameter λ, given by:

$$\lambda = \frac{2.06}{d_0} \sqrt[3]{\frac{RW^2}{\pi E^2}} \tag{2.28}$$

where d_0 is a typical atomic dimension. According to Maugis theory, the transition from the JKR to DMT interaction is a continuous process and can be described by the dimensionless parameter λ [196].

Discussion As has been shown, different contact mechanics theories can be applied to describe the sample-indenter interaction. Each theory has a certain region of applicability within the experimental conditions, which was further summarised in [201].

In practice, when a full description of the system is required, all the parameters need to be known. This is usually not possible as the main reason for doing experiments is to determine some of these properties. Typically, in the limit of high loads, the Hertz model can be applied to infer properties such as Young's modulus [196].

Each of the theories described so far has a region of applicability and other limitations. In particular, they all assume the surfaces are continuous and elastic. No plastic or viscoelastic properties are considered either. All of these can be serious limitations at the molecular scale. What is also important is that the AFM measures the *local* properties of the sample, due the small size of the probe. This might not necessarily be the same as the bulk value of any measured property.

All the above theories also assume the sample thickness is typically much larger (in fact, infinitely larger) than the indentation depths. Their applicability breaks down when the thickness of the sample is finite and approaches in size the radius of the indenter. In such cases, the measured stiffness is influenced by the stiffness of the underlying substrate [202]. This is important for the case of measuring the stiffness of a biologically

relevant sample, such as a lipid bilayer (thickness ~5 nm) with the AFM tip (radius $\sim 10 - 20$ nm).

The Chadwick theory This model [203] has been specifically designed to model the indentation of *thin* films on hard substrates. The films are assumed to be isotropic, homogenous, and incompressible. The resulting relation between force and indentation is given by:

$$F = \frac{2\pi E R^2 \delta^3}{3h^3} \tag{2.29a}$$

$$F = \frac{2\pi E R^2 \delta^2}{3h} \tag{2.29b}$$

where all the symbols are as before and h is the thickness of the film being indented. The above equations are the solution for the case when the film is bonded to the underlying substrate (eqn. (2.29a)), or slipping (eqn. (2.29b))

2.3.4 Modes of operation

The interaction forces described above form the basic principles of why the AFM can be used as an imaging tool. The sensing itself can be done in a few ways, and the microscope can be operated in a few regimes, the most common being the *contact mode*, the intermitent-contact/non-contact *tapping mode* and the non-contact *frequency modulation* mode. Only the first two were used in this thesis and they are described below.

Contact mode

This is the simplest, or most 'basic' AFM operational mode, where the probe is 'dragged' across the sample and follows the contour of the surface. Each such scan produces a (straight) contour line. The image is acquired by scanning the sample continuously and accumulating a series of such adjacent topology profiles.

Tip deflection is used as feedback in this mode. When the deflection changes in response to the topology of the sample, the feedback loop adjusts the height of the tip above the probe, maintaining a constant probe deflection and tip-sample separation (and, by extension, a constant force). In this mode the probe operates in the repulsive range of the tip-sample interaction.

This is a very basic method or AFM operation but it is also the most intuitive to understand. However, because the tip is in contact with the sample, some sample deformation can occur, especially for the softer (or, biologically relevant) specimens.

Tapping mode

In this setup, the tip is oscillated (usually acoustically by the vibrating piezo) at, or near, its resonant frequency (see chapter 2.3.2) *while* scanning the sample [204, 205, 206]. The line-after-line raster scanning itself is done much like in contact mode. As a consequence of this tip oscillation, the probe touches the sample only intermittently, at the lowest point in the oscillating cycle. In certain situations, the tip doesn't touch the sample at all. The obvious advantage of this setup is that a topography of the sample can be acquired without much (or any) mechanical contact between the tip and the sample.

The AFM cantilever in tapping mode is driven into oscillation [206]. The resulting signal is also oscillatory in nature. The response signal carries with it not just deflection information (like in contact mode), but also an oscillation amplitude and phase (with respect to the drive oscillation). These signals carry additional information about the tip-sample interaction force. The phase signal is particularly useful as it can be related to energy losses in the interaction [207, 208, 206, 209, 210]. As such losses will depend on the material imaged, the phase contrast image can detect differences in the specimen imaged (e.g. specimens with different stiffness, where the energy lost will depend on sample compliance). The feedback parameter in tapping mode operation is the signal amplitude [206, 205]

In tapping mode, the tip motion can be described by the following equation of a point mass [207, 211, 212, 213]:

$$m\ddot{z} + kz + \frac{m\omega_0}{Q}\dot{z} = F + F_0 \cos(\omega t) \tag{2.30}$$

where m is the mass, z is the displacement, k is the cantilever spring constant, ω and ω_0 are the oscillation and resonant frequency of the cantilever, F_0 is the drive force and F is the tip-sample interaction force. Without the force F, the solution to this equation is a well-known forced harmonic oscillator. The presence of F makes it difficult to solve the equation exactly. In fact, in a dynamic system like this, more than one stable solution to the equation of motion exists due to the interaction forces F [211, 212]. The solution of eqn. (2.30) is further changed when the AFM is operated in liquid.

AFM in liquid

The behaviour of the AFM tip in liquid is more complicated and a full understanding of the tip response is difficult to obtain. While immersing the tip in liquid removes the capillary forces, it also introduces a range of other effects, which complicate the experiments. Cantilever resonant frequency is lowered and the resonance peak broadened [214]. Additional resonance peaks also appear, complicating the choice of the drive frequency. Increased hydrodynamic damping [215, 216, 196], and coupling of the AFM vibrational modes also reduce the tip quality factor Q, reducing the signal for a given drive amplitude. Typical Q values in liquid operation obtained in this work are in range $1 - 5$, compared to $> 100 - 200$ in air.

AFM in liquid is nevertheless a valuable tool for investigating biological samples in their native environments. Tapping mode operation in liquid allows the imaging of biological samples at small forces, therefore keeping their structure. All the experiments in this project have been performed in liquid.

2.3.5 Force curves

Apart from imaging, the AFM can be used to acquire local interaction forces [217, 196]. In a typical force measurement, the tip is positioned above a fixed point above the sample (i.e. not scanning). The tip is then pressed onto the sample surface. By measuring the tip deflection, much like for imaging, the force response of such indentation can be determined. The result of this measurement is a cantilever deflection versus position of the piezo curve. This can then be turned into force-versus-distance curve by converting the cantilever deflection into force (using its spring constant k) and the tip-sample distance is calculated from the tip deflection and piezo position. Such a force-distance curve is referred to as *force curve* for short.

In this work, force-distance curves were converted into force-sample indentation curves. In such form, the mechanical sample response can be compared to contact models described in section 2.3.3.

3 MD simulations of controlled CNT-lipid bilayer interaction

Earlier chapters outlined the potential use of carbon nanotubes in nanotechnology and as nanocarriers. Due to their nano size, they are well suited for investigating using molecular simulations. A number of studies have investigated the interactions of CNTs with lipid bilayers [218]. Each of these studies researched different aspects of the problem, including interactions with detergents[219, 220], solubility [221, 220], energetic [222, 223], structural [224, 225], or elastic properties [225]. The focus of this chapter is the mechanical response and deformation of CNTs upon contact with lipid bilayers.

The bulk of computational work done on the CNT/lipid bilayer system focuses on 'ultra-short' nanotubes interacting with a single lipid species (usually a phosphatidylcholine, e.g. DPPC). The CNTs are usually left to either freely interact with the membrane [223, 226, 227] or are pulled at relatively high speeds in a systematic and controlled manner [228, 229, 219, 220, 230]. Both of these factors are convenient from the simulation perspective for a few reasons: shorter nanotubes (typically about $5-6$ nm in length) allow the use of smaller simulation boxes and the fast pulling speeds allow shorter simulations, both of which reduce the computational time needed. There are a few problems with these approaches. Firstly, real CNTs are much larger than the ones used (see chapter 1.2.2) and, the 'ultra-short' nanotubes are usually of the length comparable with the thickness of the lipid bilayer [223, 226, 228, 229, 231, 218]. This

in itself is a major limitation as it makes impossible the observation of processes at the length scale comparable to the length of a real CNT (see chapter 1.2.2). Also, systematic, experimental preparation of such short nanotubes would be very difficult to control due to the nature of the methods typically employed (see chapter 1.2.2). It is therefore of interest to investigate the properties of longer CNTs. Secondly, the typical pulling speeds employed in those previous simulations are very high and may not correspond to the speeds of processes *in vitro* and *in vivo*.

In this section the interaction of longer CNTs with lipid bilayers is systematically examined. The CNTs are pulled towards the lipid bilayer at significantly slower speeds than in previous studies. This gives rise to interactions not reported before. The focus here is on mechanical response of the system upon perturbation. These new effects are cross-checked using different lipid species. By inspecting the sensitivity to force field parametrisation, it is inferred that hydrophobicity is what gives CNTs their special properties reported here.

3.1 Methods

The MD simulations presented in this chapter were all performed in GROMACS [232] (www.gromacs.org) simulation package, version 4.5.1. They were run on a local cluster. Coarse-grained methodology (see chapter 2.1.3) was implemented throughout this work. Two force fields were used: a locally developed version of the MARTINI force field, further referred to as the 'Bond' force field [143] (with particle types based on MARTINI [144]), and a newer version of MARTINI [145] (referred to as MARTINI2 throughout this text). Lipid and solvent parameters were taken from the corresponding force fields. Lipids used were: DPPC, POPC, POPE.

CNT parameters were as in [220], where a 4:1 CG mapping was used to preserve the hexagonal carbon lattice of the CNT (fig. 1.4). The CNT model initially used the C

apolar particle type from the Bond force field (based on C type in MARTINI). This particle type was modified later in the chapter, as explained in the relevant sections. The CNTs used were all 12 nm long. Both capped and uncapped types were used for the early simulations. In light of the the preliminary results, this was narrowed down to the uncapped type only and, unless stated otherwise, the results presented are for the uncapped CNTs. Initially, two CNT chiralities were considered: $(18, 0)$ and $(32, 0)$, with diameters d = 1.4 nm and d = 2.5 nm, respectively. The (32,0) CNTs were used to investigate the influence of the nanotube radius on the observed effects and system behaviour. Only a handful of simulations was carried out using (32,0) CNTs and, unless explicitly mentioned, all the results are for the (18,0) nanotubes. No charged groups were considered (see chapter 2.1.3).

All simulations were performed at a constant temperature (323 K, above the DPPC phase transition within the force fields used [145, 233]), pressure (1bar) and number of particles. The CNT was initially placed at ~2.5 nm above a preformed bilayer and equilibrated for at least 2 ns while keeping its position restrained. This was done to ensure it was initially beyond the cutoff range for interactions with the bilayer in the used force fields (1.2 nm for MARTINI [144]). For the production runs, the CNT was pulled (see below) for either 5 nm or 20 nm at two different speeds (v= 0.1 nm ns^{-1} and lower, compared to v= 0.5 nm ns^{-1} and higher used in other studies [229, 230]), resulting in four simulation times of 50 ns, 200 ns for the faster pulling or 500 ns and 2000 ns for the slower pulling. The 5 nm pulling was performed to investigate the initial interaction with the lipid bilayer, just as the CNT touches and enters the bilayer. The longer pulling was done to investigate the effects of pulling the CNT through to the other side of the bilayer. The membrane patch size was 12×12 nm^2, 18×18 nm^2 or 30×30 nm^2, depending on the simulation. A snapshot of the initial system setup can be seen in fig. 3.1.

The CNT was then pulled in a needle-like manner towards the membrane. To achieve that, steered molecular dynamics was used. This was carried out by attaching a virtual spring to the centre of mass of the CNT and pulling a virtual point at the other end of this spring towards the bilayer (red arrow, down in the z-direction in fig. 3.1) at constant speed v. The spring constant k was 500 kJ mol^{-1} nm^{-2}, which corresponds to the stiffness of a soft AFM cantilever for biological uses. Two pulling speeds v of 0.01 nm ns^{-1} and 0.1 nm ns^{-1} were used. To ensure that the CNT approached the bilayer in a controlled, perpendicular, needle-like manner, positions of all its atoms were restrained in the x and y directions by attaching virtual springs of stiffness 1000 kJ mol^{-1} nm^{-2} to each atom. This way, z was the only dimension for free, unrestrained CNT motion.

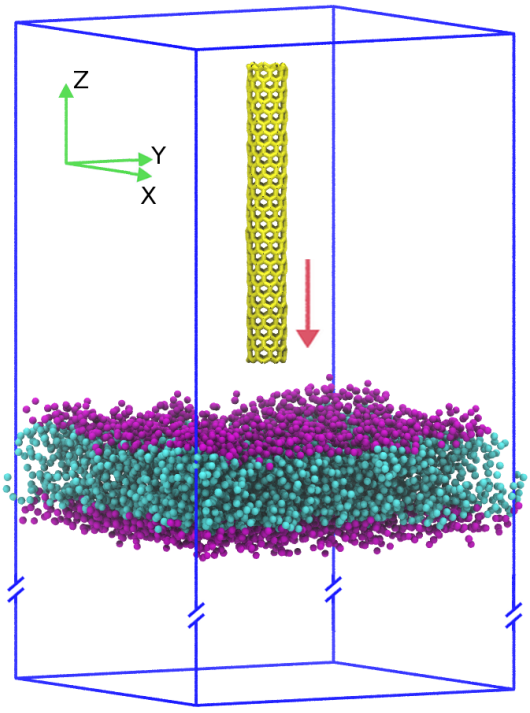


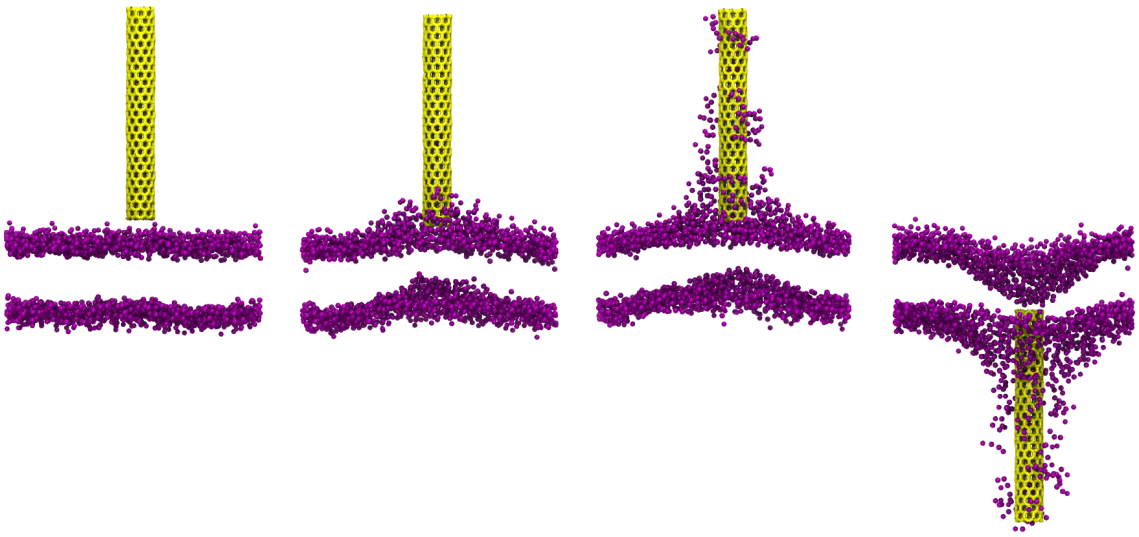
Figure 3.1: Simulation scene overview: CNT above a 12×12 nm^2 POPC membrane patch. Yellow: CNT, purple: lipid headgroups, cyan: lipid tails. Axes as labelled by the green inset. Pulling direction indicated by the red arrow. The box has been shortened as indicated by the broken lines.

3.2 Results

Except where noted, the discussion concerns open-ended (18,0) CNTs. There were only a few differences between capped and open CNTs and they are mentioned where relevant. Similarly, the (32,0) CNTs were simulated for comparison purposes and they are mentioned as required. (18,0) open-ended CNTs are to be assumed otherwise.

3.2.1 Response to pulling

Upon approach, the CNT seems to have no apparent effect on the bilayer, which remains flat (fig. 3.2a) until the tip of the CNT pierces the top of the bilayer and lipid headgroups. As soon as the CNT is within the headgroups, the membrane deforms, forming a meniscus-like structure around the tube (fig. 3.2b). In the simulations where the CNT was allowed to pass through to the other side the membrane, the behaviour of different leaflets seems to indicate the affinity of the CNT to the hydrophobic core of the membrane. Firstly, the entire membrane deforms, forming the aforementioned meniscus. The lipids in the top leaflet (on the CNT side of the membrane) seem pulled towards the tube, which leads to membrane deformation. The lower leaflet follows the upper to preserve the integrity of the membrane (fig. 3.2b). As the CNT is pulled through to



(a) Initial setup (b) Piercing (c) Lipid creep (d) Pocket formation

Figure 3.2: Membrane response to CNT pulling. Shown are snapshots from a typical piercing event. Data from a slow-pulling, 2000 ns simulation with a 12 nm uncapped CNT and POPC bilayer. Lipid hydrocarbons and water removed from view. Lipid headgroups shown in purple. (a) CNT approaching membrane, 113 ns, (b) CNT piercing membrane, showing meniscus formation, 156 ns (c) Lipid creep, 193 ns, (d) Lipid pocket formation upon CNT exit from the bilayer, 1706 ns.

the other side of the lipids, the lower leaflet forms a pocket around the CNT (fig. 3.2d), which shields the hydrophobic CNT from the interaction with water. After the CNT emerges on the other side of the bilayer, it is coated with lipids. The bilayer itself was intact in all simulations. This suggests that the slower pulling rates allow enough time for the lipids to equilibrate in response to the disruption due to the CNT.

The initial part of the interaction deserves a closer inspection. Once the CNT enters the lipid bilayer, a meniscus is formed. This is a randomly triggered event. The wait times before the lipids start forming this meniscus vary ($0 - 10$ ns) and the distance at which the CNT is from the lipid heads is variable as well (it is, however, in very close proximity to it). Both these times and distances are confined to a limited range defined by the pulling rate (which brings the CNT towards the bilayer) and the proximity to the membrane. The event of meniscus creation appears to be triggered by a single lipid being driven out of the membrane by a random fluctuation. Such a fluctuation helps to momentarily drive a single lipid out of the plane of membrane, which would not be possible in a completely static picture, where no membrane fluctuations or undulations are present. These tend to be larger for larger membrane sizes and are more observable for the $30 \times 30\ nm^2$ systems (where the box size is large enough not to suppress motions and not induce large self-correlations). This fluctuation induces an apparently cooperative transition, where the neighbouring lipids follow the initial one (fig. 3.3). This cooperative effect is not clearly evident in all simulations. It shows more often in the case of thicker CNTs. The variation in time after the CNT comes into proximity with the lipid headgroups, along with the variation of separation at which the meniscus is formed seem to confirm that the transition is triggered by a random event, which initiates further deformation. The formation of this meniscus is in agreement with [222], where mean field simulations were used to obtain similar results. Initially, the hydrophilic lipid headgroups shield the interaction of the hydrophobic membrane core from the hydrophobic

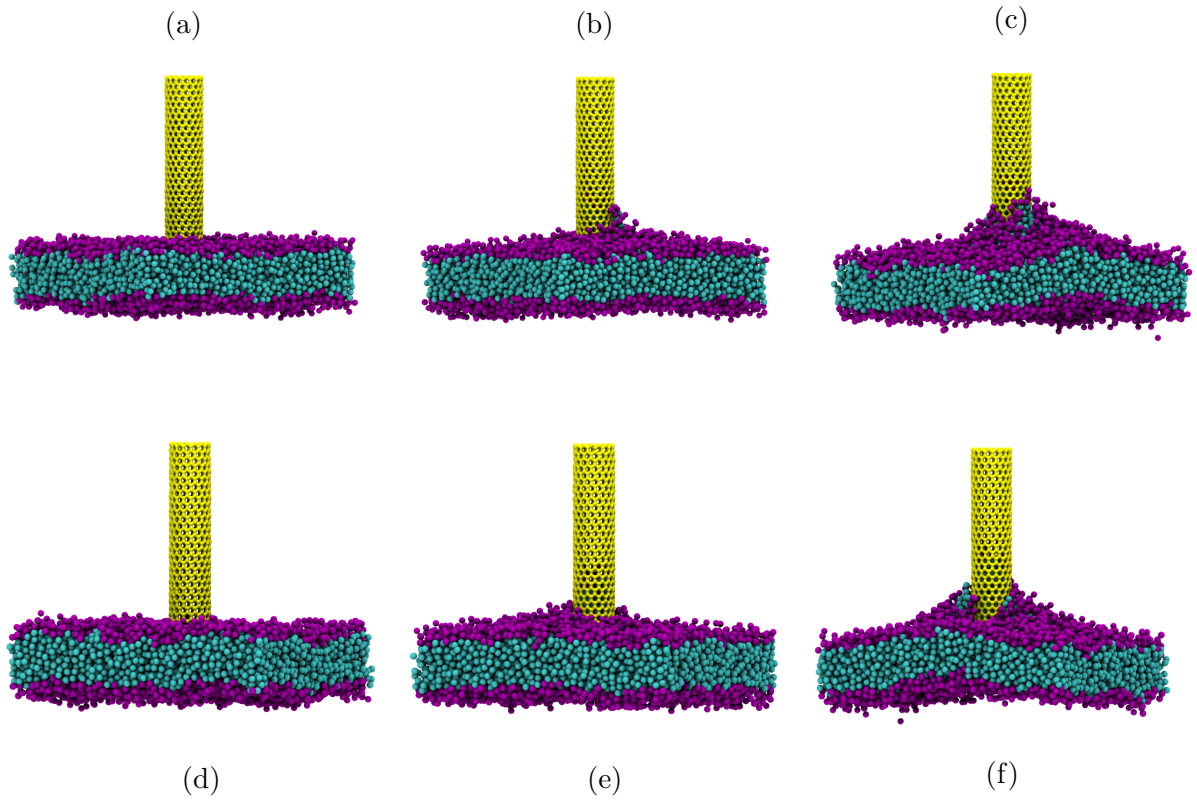
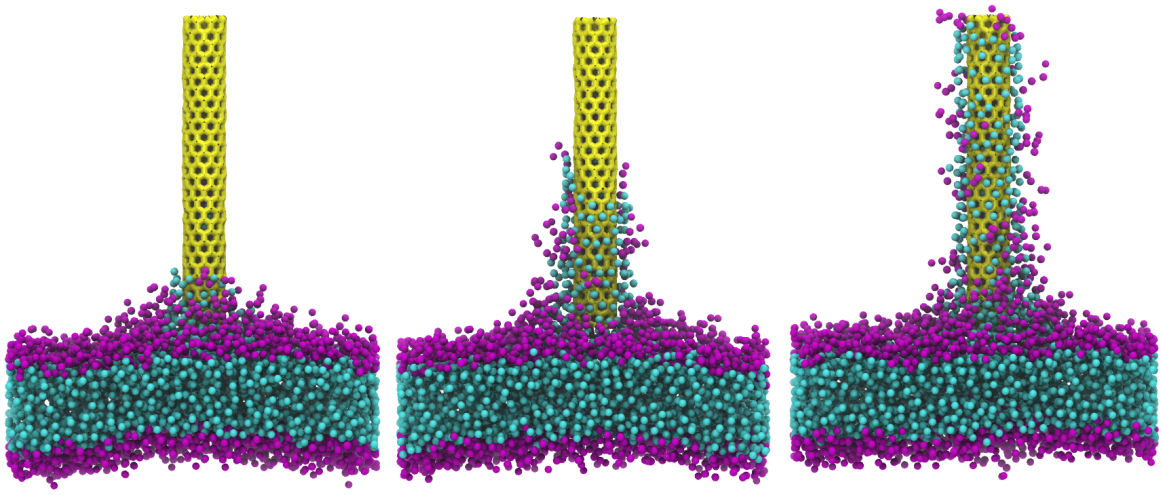


Figure 3.3: Cooperative membrane transition from flat to meniscus. Lipid engulfing shown for a (32,0), uncapped CNT with l=12 nm and d = 2.5 nm. Fast pulling towards a DPPC bilayer. Top and bottom rows are snapshots of the same time frame at two different angles (120 degrees apart). (a), (d) 209.25 ns, (b), (e) 210.50 ns, (c), (f) 212 ns

nanotube. Once the transition is initiated and the CNT comes into contact with the lipid tails, it seems to move relatively freely within the core of the membrane, which again seems to agree with [222]. This might be due to the fact that both the hydrocarbon lipid tails and the nanotube model used here are formed of the same C particle type in the Bond force field. This is further explored in a later section (see chapter 3.2.2).

Complementary to the formation of the mentioned meniscus is the creep of lipids both on the inside and the outside of the CNT (fig. 3.4). The blocking of the CNT core with lipids has been reported before [230]. The new phenomenon here is the creep of lipids on the outside of the nanotube. The formation of the meniscus mentioned earlier will only disturb the membrane elevation to $\sim 4-5$ nm from the CNT walls. This curvature effect



(a) Meniscus (b) Initial creep (c) Full CNT coverage.

Figure 3.4: Lipid creep. Shown are snapshots from a 2000 ns pulling simulation. Clear lipid creep on the CNT can be seen from the meniscus formation to full CNT coverage. (a) 156 ns, (b) 164 ns, (c) 209 ns.

is limited by the mechanical properties of the bilayer, such as its bending modulus [234]. Moreover, both the top and bottom leaflet initially deform almost equally to form the meniscus in response to CNT piercing (fig. 3.2b). Neither of these is surprising, as the bilayer tends to remain whole without any gaps between leaflets and can be described by certain mesoscopic mechanical properties. If, however, the length of the nanotube is larger than the thickness of the bilayer, then the part of the CNT that has not interacted with lipids (referred to as the top part) will be exposed to unfavourable interaction with water. After the initial deformation of the bilayer, lipids will start creeping up the walls of the CNT (fig. 3.2c, fig. 3.4, fig. 3.5, fig. 3.6). The observed creep rate varies with an average of 0.35 ± 0.1 nm ns^{-1} and a median of 0.35 nm ns^{-1} As this is at the lower bound of (or lower than) the pulling rates used in previous work, it explains why this phenomenon has not been observed before. No noticeable increase of lipid flip-flop rate was observed. As the lipids creeping up the CNT largely come from the upper leaflet, this would create an imbalance in the lipid numbers between the leaflets. This was relaxed by using larger box sizes, accommodating larger bilayer patches. In all

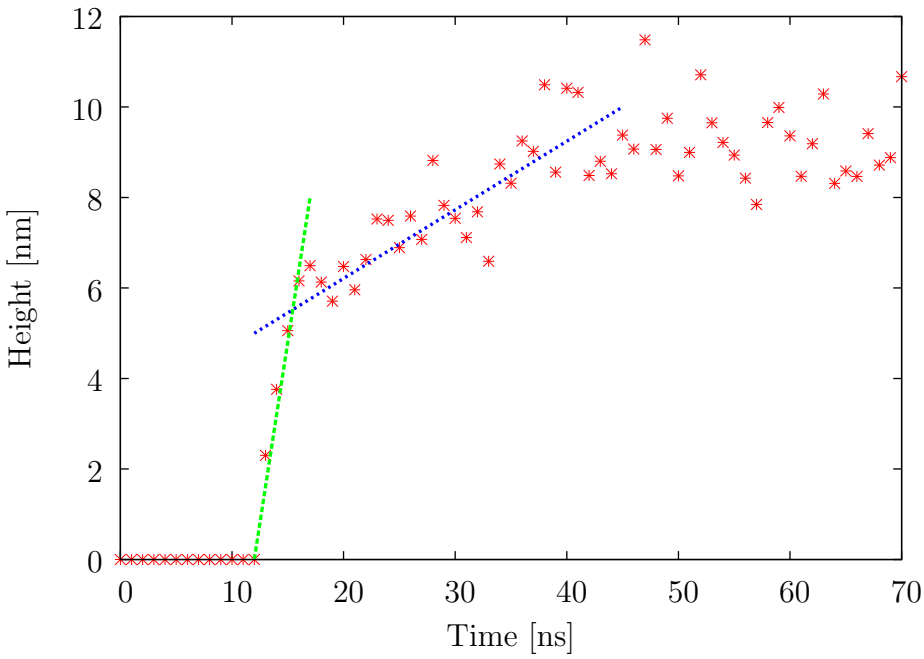


Figure 3.5: Heights above the bilayer of the most elevated lipids just outside the CNT for a 2000 ns capped simulation in Bond force field on DPPC. Lines are just guides for the eye and show two different lipid creep rates. The initial part (green line) corresponds to quick meniscus formation. The blue line corresponds to lipid creep, which elevates the lipids along the CNT at a different rate to that of meniscus formation. Data points past ~50 ns correspond to lipids that reached the top of the CNT and are pulled down along with the nanotube itself and so data past 70 ns is cut off for clarity.

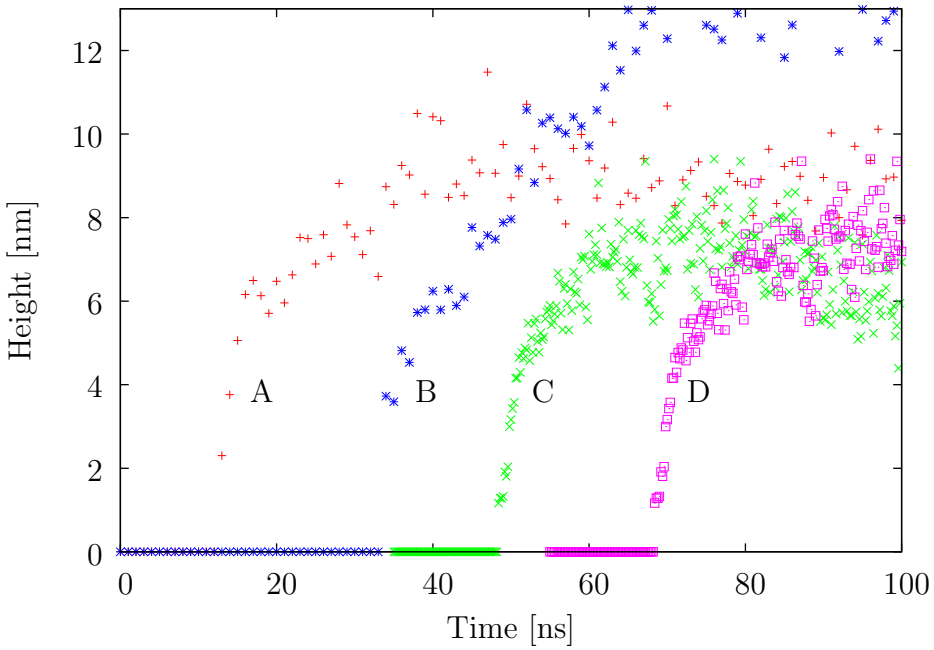


Figure 3.6: Heights above the bilayer of the most elevated lipids just outside the CNT for different CNT pulling speeds and ends (capped and uncapped). Data as in fig. 3.5. Different lipid creep rates (slopes of the data) clearly visible across the simulations. Data points shifted along the horizontal axis for clarity. A: capped, slow, B: capped, fast, C: uncapped, slow, D: uncapped, fast.

simulations this creep continues until the entire length of the nanotube is covered (see fig. 3.4c). This effect shows the mechanism by which the lipids screen the far end of the nanotube from the unfavourable interactions with water. While some of the lipid tails might now be exposed to water, the lipid heads (pointing away from the CNT, as in fig. 3.4b and fig. 3.4c) still provide at least partial screening of the hydrophobic CNT surface. This creep can be thought of as complementary to the formation of the pocket on CNT exit from the membrane. Both of these show that there are mechanisms by which the membrane shields the nanotube.

The inner side of the CNT, initially filled with water (due to the open-ended nature of the CNTs used), is rapidly filled with lipids. These tend to predominantly come from the upper leaflet. Upon contact, lipids go up along the interior of the CNT on the timescale of a few nanoseconds. This is consistent with [230]. This process happening inside the CNT is quicker than on the outside walls, possibly due to the overall favourable environment inside the CNT - displacing a water CG bead leaves the lipids surrounded by hydrophobic particles on all sides due to the small diameter of the tube. The confinement of the lipid in a rigid tube may also play a role.

In previous work, it has been reported that shorter nanotubes rotate with their long axis turning towards the plane of the membrane, such that the nanotube sits within the hydrocarbon tails of lipids [223, 226]. Here, due to the controlled movement of the CNT and its restriction in the xy plane such rotation is not possible. This is a sensible restriction when the modelled CNTs are longer than the bilayer patch size. It allows another mechanism to be observed, whereby the membrane adapts to coat the nanotube.

This membrane adaptation is accompanied by an increase in thickness around the nanotube (fig. 3.7). This is induced by the nanotube penetrating the lipid bilayer as shown by the concentric thickness profile in fig. 3.8. This thickness increase extends up to ~7 nm from the nanotube walls. It could be explained in terms of the membrane

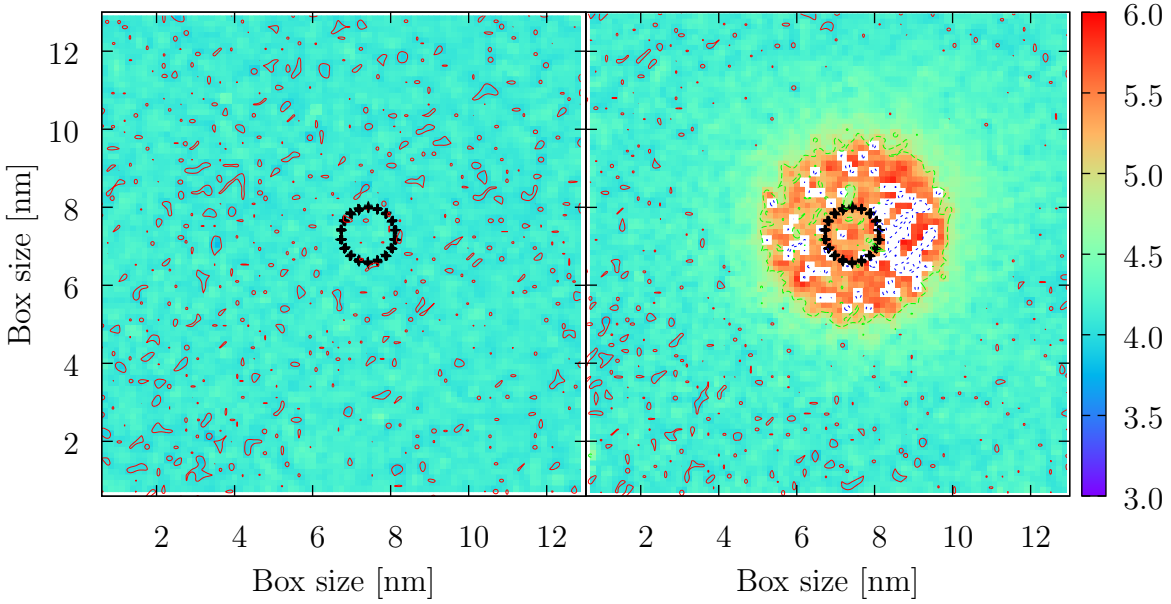


Figure 3.7: Membrane thickness map. Left figure: flat before CNT contact. Right figure: after CNT contact. Black circle represents the nanotube. Contours every 0.5 nm. Vertical scale in nanometres.

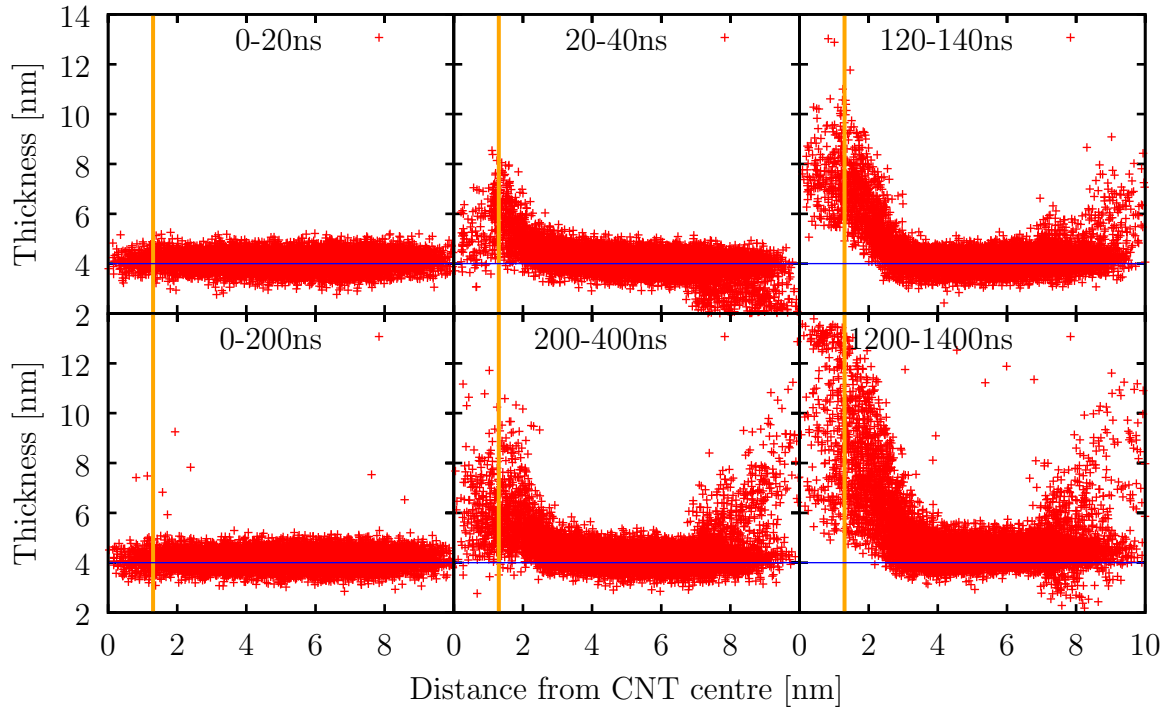


Figure 3.8: Membrane radial thickness. Zero corresponds to the CNT centre. Orange line represents CNT wall. Blue line is a guide for the eye. All graphs are averages for the indicated number of nanoseconds (same number of CG simulation frames and similar CNT position in relation to the bilayer). Uncapped CNT on POPC, Bond force field. Top row: fast pulling. Bottom row: slow pulling.

thickening and extending its hydrophobic core to better shield the nanotube from water and provide an environment compatible with the hydrophobic nanotube.

3.2.2 Sensitivity to lipid species

The same simulations were then run using different lipid species. This was done to check how sensitive the above mentioned effects are to small variations in parametrisation and in lipid structure. Two different lipid kinds were examined. Firstly, POPC (16:0-18:1 PC) was used to see if the lipid chain properties influence the interaction. POPC has structure similar to DPPC, with two additional carbon atoms and an unsaturated bond in one of the lipid chains (which alters lipid chain packing in the bilayer). POPE (16:0-18:1 PE) is similar to POPC, except that is has a different headgroup, which alters the lipid packaging properties as well [234, 2]. These two subtle lipid changes were then used to set up new simulations, with all parameters as described in the preceding section.

The result of those changes were very reassuring. All the effects and interactions observed for DPPC were also present in these simulations. All the CNT entry effects (see chapter 3.2.1) were present. Meniscus was formed upon contact (as in fig. 3.2b). The extent of membrane deformation was ~5 nm. This slight variation is to be expected due to material properties exhibited by the bilayer. More importantly, the lipid creep was observed in both cases. The rate of creep was 0.53 ± 0.37 nm ns^{-1} with a median of 0.42 nm ns^{-1}. The bilayer thickening upon CNT piercing was also confirmed. When the CNT was pulled through, a pocket was formed on the bottom side of the bilayer and the bilayer was left intact as before. Overall, there was no noticeable qualitative difference in behaviour observed for DPPC, POPC and POPE. This suggests that the observed interactions are universal across common lipid species used in biophysical experiments. Naturally, in cell membranes, more complex lipid mixtures are present [233, 14, 235, 12, 236] and only a small subset can be analysed in the current study.

3.2.3 Sensitivity to force field parametrisation

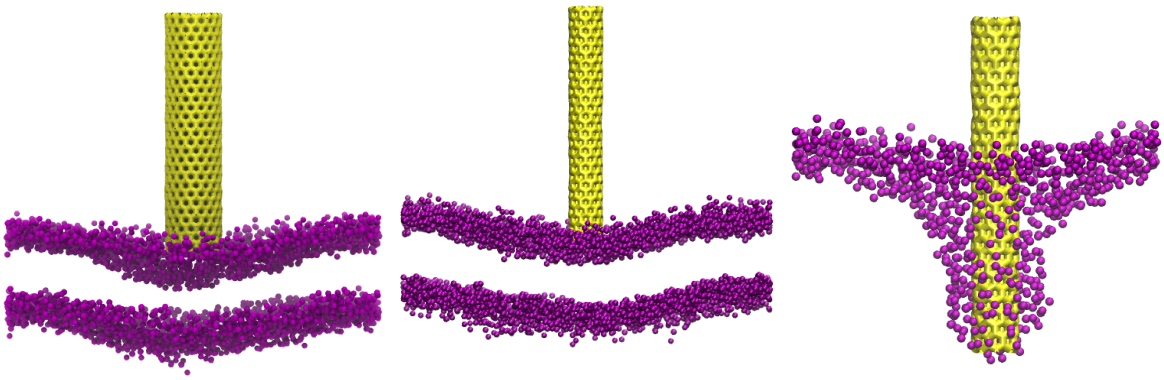
Having established the robustness of the newly observed effects to changes in bilayer lipid species, the next test was to try different force fields to check how the overall system parametrisation and particular choice of force fields affects the observed effects (by slightly altering the strength of the underlying interactions specific to each force field). Along with the Bond force field used before, MARTINI2 [145], a newer version of MARTINI [144] was used.

In MARTINI, the coarse-grained particles fell into ten different types, which interacted at five different energy levels (see chapter 2.1.3). A similar scheme applied to the Bond force field. In MARTINI2, particles could now be of one of eighteen different types, interacting at ten different energy levels (see chapter 2.1.3). It is of consequence here that in Bond/MARTINI, both the hydrocarbon lipid tails and CNT were represented by the apolar C type. In MARTINI2, this type was now split into five different types, with varying hydrophobicity. The lipid parameters were taken from [145], where the hydrocarbons were assigned the most hydrophobic type C1. For porting purposes, there is a correspondence between the energy levels in MARTINI and certain energy levels in MARTINI2, the latter having a wider and more fine-tuned set of levels. While lipid parameters were accurate and come as a part of the force field, based on the energy level correspondence, CNT could now be of either C1, C2, or C3 type, each having a different level of hydrophobicity. This is significant, as previously all the hydrocarbon-CNT interactions were all bundled into one fairly broad ensemble. The fine tuning of levels in MARTINI2 allows exploration of a wider range of interactions and the examination of sensitivity to parametrisation.

A range of simulations were performed, where CNT-like molecules were assigned different particle types for the carbon coarse-grained beads (as opposed to just C used in the section 3.2.1). The rest of the model used was as before. In Bond, the particle

types used were the non-polar N0 and polar P. In MARTINI2, the CNT and proof-of-concept CNT-like nanotubes were modelled with all hydrophobic particle types C1-C5, the neutral N0 type and two polar types P1 and P2 (which split from the P type in Bond/MARTINI). It was done to investigate how a proof-of-concept derivatised CNT would interact with a lipid bilayer. The simulations were prepared as in the previous two sections, with two different pulling speeds as before.

The first thing to notice is the behaviour of C1-C3 particle types in MARTINI2, along with the different lipids tried in Bond (see chapter 3.2.2). The behaviour of C1-C3 particle types is most consistent with what was observed in the previous section. Firstly, the lipid creep and membrane thickening were observed as before. However, for fast CNT pulling, the lipid creep was not as pronounced, disappearing altogether for the least hydrophobic particle type C3. This suggests that lipid creep depends on two factors: very slow pulling speeds and the hydrophobic compatibility of both lipids and carbon nanotube. Two new effects were observed in this set of simulations. Firstly, in all cases, the membrane would thin slightly around the CNT when it was in close proximity to the bilayer (i.e. just before touching). This thinning amounted to about $0.5 - 1$ nm and was centred on the CNT, with a radial extent of $\sim 3 - 4$ nm. Secondly, the bilayer would form a depression just before CNT-membrane contact (fig. 3.9). This depression could be described in terms of more unfavourable CNT-lipid interactions. It should be noted this effect is most pronounced at the fast pulling rates, which indicates that this could also be a membrane deformation that results from the steric push of the CNT or the water squeezed between the CNT and bilayer. This deformation is not as pronounced at slow pulling speeds. This could indicate a double origin of this effect, namely hydrophobic incompatibility between the derivatised CNT and the bilayer core, or it could be a sign that what is observed throughout this chapter, and particularly at slow pulling speeds, is a result of a near equilibrium behaviour of the bilayer-CNT system.



(a) DPPC, C3, Fast (b) DPPC, C4, Fast (c) POPE, P, Slow

Figure 3.9: Lipid depression under different pulling conditions. (a)-(b) MARTINI2, (c) Bond force field. Different lipids and particle types for the CNT-like molecules as labelled. (a)-(b) maximum depression depth before meniscus formation and piercing. (c) extreme membrane depression and deformation under a polar particle type P. Only headgroups from the top bilayer leaflet shown for clarity. Such depressions are a result of moving away from the hydrophobic nature of the CNT-like molecule.

This equilibrium-like behaviour is discussed later. All these phenomena for the Bond simulations and C1-C3 MARTINI2 simulations are summarised in tables 3.1 and 3.2.

When the other particle types are considered, it becomes clearer that the less hydrophobic CNT-like molecules do not give rise to the effects described in previous sections. Firstly, for MARTINI2, the lipid creep disappears when the particle type is less hydrophobic than C4. The membrane thickening disappears at C5. Membrane thinning seems to disappear at C4 (but reappears for the polar P1 and P2 types). The exception is the non-polar N0 type, where thinning occurs at the faster pulling speeds. This could be associated with the pressure exerted via the solvent. It also could imply that the membrane is more relaxed at slower pulling speeds and adapts more readily to the presence of the CNT. This could also explain the disappearance of depression for C4 and C5 types at slower speeds. Slower pulling speeds give rise to slower changes in position, which in turn give the membrane more time to adapt. All the differences observed for MARTINI2 (table 3.4) can be also confirmed for Bond (table 3.3).

Overall, although changing the force field introduces new effects into the picture, it

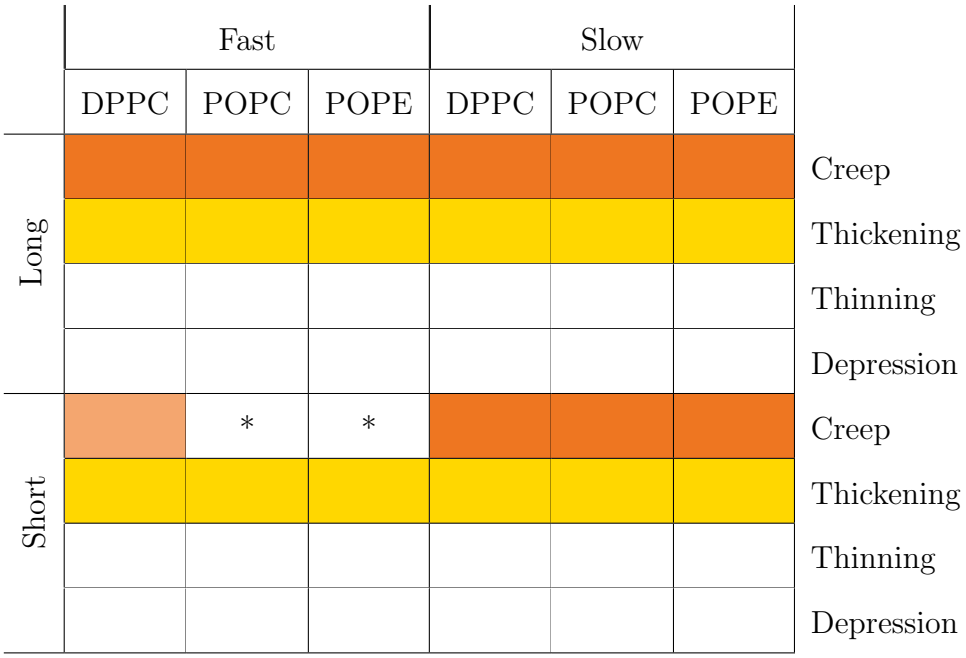


Table 3.1: Effects of parametrisation - Bond force field. Full colour indicates clear and pronounced effect. Pale colour indicates effect present but not very pronounced. White indicates no effect present. Star indicates the simulations investigated were too short to observe effect. Fast and slow refer to the pulling speeds. Long and short refer to the simulation lengths (see chapter 3.1).

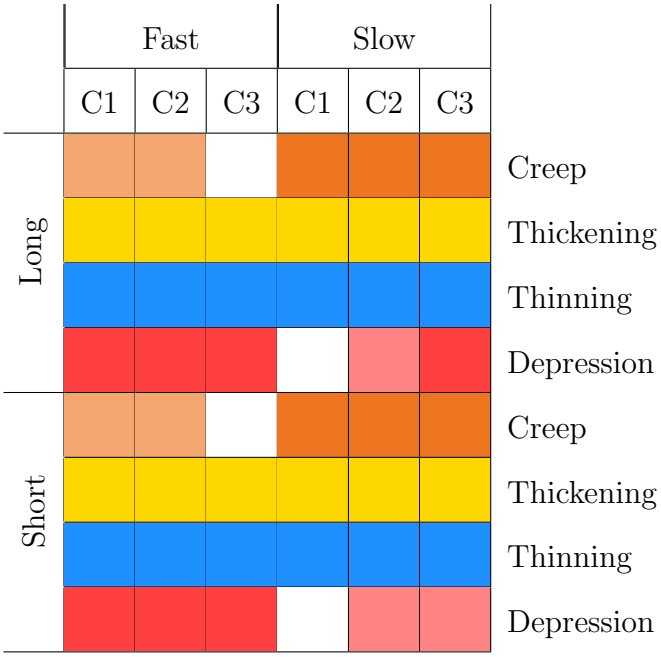


Table 3.2: Effects of parametrisation - MARTINI2 force field. Columns C1, C2 and C3 represent particle type used for CNT in MARTINI2 simulations. Full colour indicates clear and pronounced effect. Pale colour indicates effect present but not very pronounced. White indicates no effect present. Fast and slow refer to the pulling speeds. Long and short refer to the simulation lengths (see chapter 3.1).

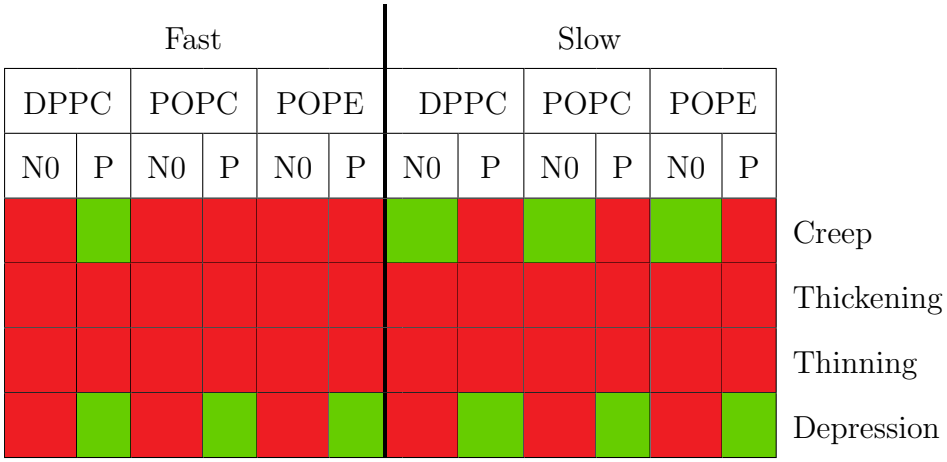


Table 3.3: Effect of parametrisation on CNT-lipid bilayer in Bond force field. Effects described in the last column correspond to those in the text. Slow and Fast correspond to pulling speeds. N0 and P are the particle types of the CNT-like molecule described (see chapter 3.2.2). Green - effect present. Red - effect absent.

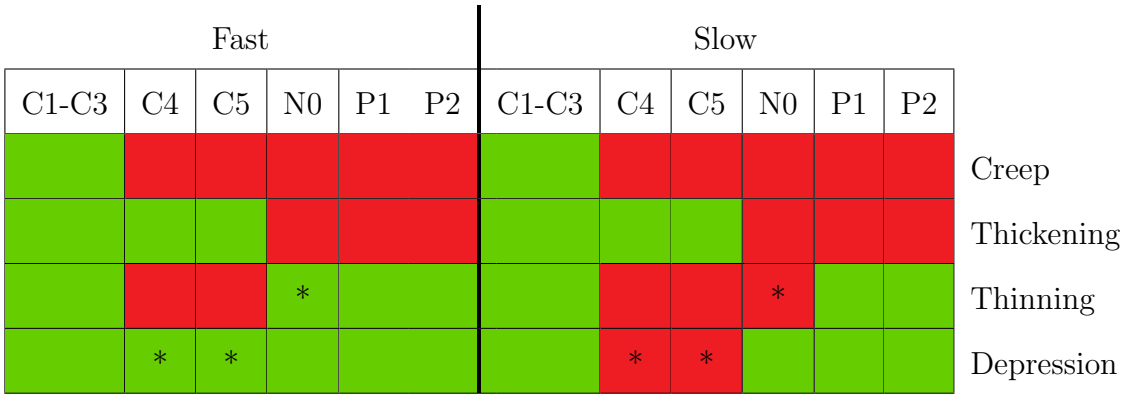


Table 3.4: Effect of parametrisation on CNT-lipid bilayer in MARTINI2 force field. Fast and slow refer to pulling speeds. Top row corresponds to particle type of the CNT-like molecule. Green - effect present. Red - effect absent. The star highlights the differences between pulling speeds.

also shows that the effects observed before, namely, lipid creep and membrane thickening, are also present. There are differences between the systems but these cannot overshadow the similarities, which lead to common behaviour. Changing the force field parameters or particle types effectively introduces changes in the CNT material used. Real, functionalised nanotubes will have different functional groups randomly scattered along the CNT wall. These could effectively be represented by different particle types in the force fields described. Changing the particle type for the entire CNT (i.e. no randomly placed impurities), as presented here, effectively averages over these functional groups. This, in turn, shows the average effects of different levels of CNT wall functionalisation. This functionalisation could either be intended or a by-product of preparation or processing. Either way, it could give insight into the future design of functional CNTs.

3.3 Summary

This work builds upon the bases set up by earlier work by Wallace and Sansom [220, 230, 219]. These publications established a methodology and parameter set [220] for the CNT-lipid systems, which subsequently led to an analysis of the interactions of CNTs with DPPC bilayers and detergents [230, 219]. That work established the groundwork for the current project. The simulations presented in this chapter can be, to some extent, seen as an extension of that previous work. Here, the simulation set-up was brought closer to that available experimentally (see chapter 4), and further cross cross-checks were carried out, by using different lipid species and force fields, to ensure the observed effects were not particular to a specific choice of simulation parameters. These changes led to the observation of a variety of new effects, as discussed. These not only complement the previous work, but also stand on their own as effects that may need to be considered when analysing any further CNT-lipid simulations.

It has been shown that slow pulling of a nanotube through a lipid bilayer gives rise to

phenomena which are conserved across different lipid species and choice of simulation parameters. Lipid creep up the length of the CNT is an effect that deserves more attention. It shows that membrane lipids will coat a naked nanotube and the CNT portion that has not been in contact with the membrane in particular. On the other side of the membrane, upon CNT exit the lipids will form a pocket around the nanotube. This shows that the membrane will deform due to and adapt to the presence of the nanotube and it will cover the CNT to shield it from unfavourable interactions with water. This is an important effect. It shows that it is not just the CNT that will reorient in the membrane as in previous work, but the membrane itself will undergo changes. This might be important in situations, where a CNT approaches the membrane but is either too large to fit flat in the plane of the membrane or unable to turn. This could lead to lipid exchange when a CNT is locked between two membranes belonging to two different organelles or cells. Moreover, most carbon nanotubes are not straight when prepared, so fitting them between the bilayer leaflets could prove more problematic other than in the most idealised situations. The membrane adaptation could prove to be a method of CNT internalisation within either the membrane or the cell. This phenomenon seems to be related to the CNT hydrophobicity and slower pulling speeds. Hydrophobic compatibility could be one of the reasons why it is fairly easy for lipids to creep along a CNT surface, which provides a similar environment to that of the hydrophobic bilayer core. That this creep could only be observed at low pulling speeds is related to the slow lipid creep rate. Another possibility is related to just this - slower pulling speeds mean that the CNT-membrane system does not change as rapidly, allowing the lipids to relax around the CNT or reach a more equilibrium-like state without rapid disruptions arising from fast pulling.

4 Force spectroscopy and mechanical properties of lipid bilayers

In the realm of bilayer/CNT interactions, there has been work on the simulational side (see previous chapter and references therein) but there has been a gap between experiment and simulation. This chapter aims to bridge this gap by designing experiments and simulations that complement each other. This combined approach is used to investigate the CNT/bilayer interaction from the mechanical perspective. This is achieved by using the atomic force microscope (AFM) and molecular dynamics (MD) simulations.

The AFM is used to probe mechanical properties of the bilayer. This is first done with regular AFM probes to establish experimental basis and collect reference data on supported lipid bilayers. The same interaction is then investigated using a modified AFM probe with a CNT attached to the tip of the cantilever. This makes it possible to harness the power of the AFM to manipulate a CNT and bring it into close proximity of a lipid bilayer in a controlled way.

MD simulations (similar to those in the previous chapter) of a CNT piercing supported lipid bilayers were designed to mimic the experimental setup. Since the size of the box in a typical MD simulation varies during a run (due to pressure coupling, see chapter 2.1.4), the relative position of the simulated bilayer fluctuates slightly in the box. This makes the extraction of indentation data rather unreliable. A bilayer surrounded on both sides by a solvent would also not experience any possible compression effect due to

the lipid being confined between a hard wall and a CNT tip. These two limitations call for simulating bilayers on a hard substrate. This allows the comparison of the simulation and experimental data more directly.

By drawing on similarities between the two, it can be inferred that the simulations give additional insight into the experimental results by providing extra detail on the molecular scale. Additionally, the experimental results can be used to verify the simulational results and justify the use of molecular dynamics to study the lipid bilayer/CNT interactions.

4.1 Methods

4.1.1 Atomic force microscopy

Sample preparation

1,2-dipalmitoyl-sn-glycero-3-phosphocholine (DPPC) was purchased from Avanti Polar Lipids (Alabaster, AL, USA). For supported bilayer preparation, the chloroform was evaporated from the lipid solution with pure argon gas (BOC Special Gases, Guilford, Surrey, UK). The vial containing the dried lipids was then placed in vacuum for at least four hours. The lipids were then rehydrated using a stock buffer (30 mM HEPES, 5 mM EDTA, 1 mM EGTA, pH 7.4) to a concentration of 2.5 mg ml^{-1} and sonicated for at least 20 minutes. A drop (~5 μl) of the lipid solution was deposited on freshly cleaved mica and placed in a closed dish at ambient temperature for at least 20 minutes. The environment inside the dish was kept humid by enclosing water in it to decrease the buffer evaporation rate. The sample was then rinsed with the imaging buffer (30 mM HEPES, 40 mM NaCl, 260 mM KCl, pH 7.4). For imaging and force measurements, more imaging buffer (~150 μl) was added to the sample. Imaging buffers were renewed periodically and a fresh lipid sample was prepared daily for the final experiments. All buffer chemicals were purchased from Sigma-Aldrich (Dorset, UK).

Imaging

All measurements were carried out using MFP-3D AFM (Asylum Research, Santa Barbara, CA). All final imaging was performed in gentle tapping mode in liquid. All measurements were done using commercial or custom-made cantilevers. The commercial probe used was Olympus OMCL-RC800PSA, referred in the text as RC800 (nominal stiffness 0.76 N m^{-1}, resonant frequency 71 kHz, length 100 μm, tip radius < 20 nm). The custom CNT probe is described in a following section. The AFM was left scanning a blank sample for 1-2 hours to reach equilibrium before each experiment. A new cantilever was used for each sample. After mounting each cantilever, the precise stiffness was determined by fitting a SHO curve to the thermal power spectrum density. Cantilever sensitivity was calculated using the (surface-touching) linear part of the force curves recorded. This was done to obtain accurate values in force measurements.

Scanning was performed at the speed of one line per second, with a maximum scan size of 20×20 μm, 256 lines per scan. All imaging was carried out in closed loop mode at ambient temperature (22 °C).

Force spectroscopy

To capture force curves, a large (a few micrometers) lipid bilayer patch was imaged several times to ensure it was well adsorbed to the substrate. A number of locations for force curve measurements were then selected on the patch. The points were selected away from the edges [237] and away from each other by at least several tip radii. No more than one force curve was taken at each point to avoid the possible effects of membrane damage or hole formation.

Force curves were taken at three different speeds, an order of magnitude apart: 50 nm s^{-1} (5×10^{-8} m s^{-1}), 500 nm s^{-1} (5×10^{-7} m s^{-1}), 5000 nm s^{-1} (5×10^{-6} m s^{-1}). Measurements were taken in contact mode as well as tapping mode to capture amplitude

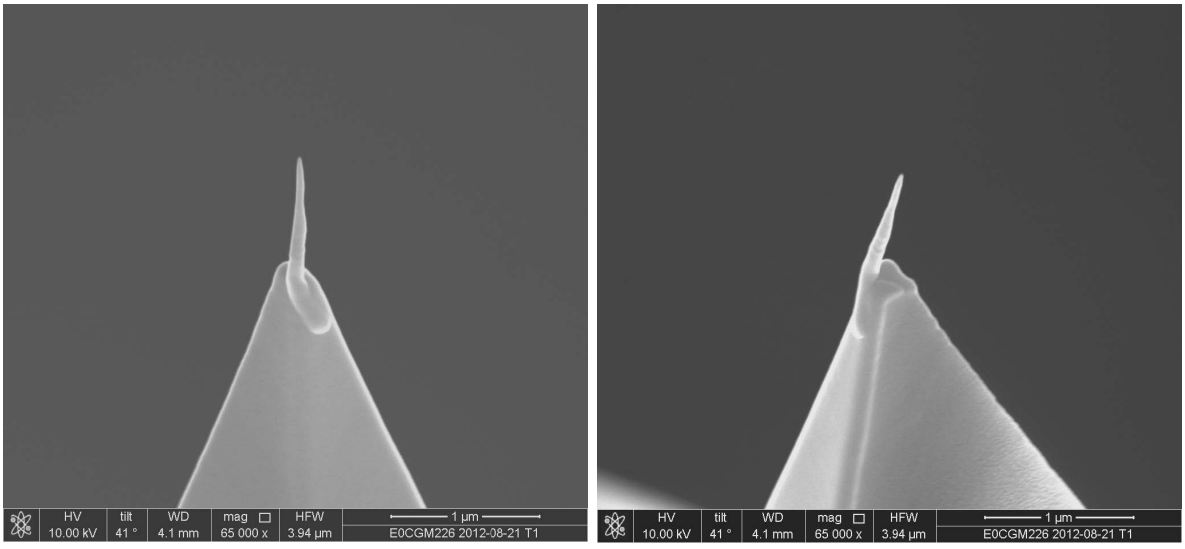
and phase data, which were necessary for the force curves using a modified CNT probe (see below). All tapping mode force curves were taken at small amplitude ($\lesssim 2$ nm, typically less). In this work, at such small amplitudes, no differences were found between force curves taken in contact and tapping mode. All force measurements were taken in open loop mode at ambient temperature as above, with a vertical range of up to 500 nm. The lipid patch was re-imaged after force curve measurement to test for possible hole formation due to cantilever piercing.

A special procedure was used for force curves taken with the modified CNT cantilever due to the possible fragility of the probe. First, a force curve at a relatively large driving voltage (~2 V, large enough for the resulting oscillation amplitude to produce a signal clearly distinguishable from the thermal noise) was taken away from the sample and the amplitude was recorded. Next, a triggered force curve was taken: The tip was retracted when the observed amplitude response dropped to ~75% of the original value. This indicated the proximity of the surface and the bottom of such force curve was taken as a starting point for the actual measurement. Vertical limits were adjusted accordingly and untriggered force curves were taken at a much smaller driving voltage (~20 mV). The resulting oscillation amplitude was of the same order of magnitude as the thermal noise (a few hundred picometres). Both amplitude and phase signals were captured along with the usual deflection signal. This allowed the collection of additional data about the system response. In particular, it made it possible to determine if the CNT was attached to the probe during consecutive measurements. This procedure was adopted to carefully adjust the vertical motion of the probe to ensure the modified cantilever was pressed gently towards the sample, without over-exerting the CNT-tip attachment. To that effect, the protocol described above allowed the selection of the smallest vertical range that was sufficient for force curve acquisition and was gentle on the CNT tip by minimising the cantilever deflection and reducing the maximum load.

CNT AFM probes

To mimic experimentally the CNT pulling simulations presented earlier, a custom-made CNT probe was purchased from Carbon Design Innovations (CDI, Burlingame, CA) [238]. The probe used was CCHR, which consists of a multi-walled CNT (nominal radius $25 - 35$ nm) mounted on cantilevers from AppNano: ANSCM-PT (nominal stiffness 1.7 N m^{-1}, frequency 62 kHz, length 225 μm, tip radius 30 nm, with Pt-Ir coating) and ANSCM-PC (nominal stiffness 0.33 N m^{-1}, frequency 17 kHz). The CNT was attached at an angle of 11 degrees relative to the base of the cantilever to ensure perpendicular contact with the sample after mounting in the AFM (the cantilever makes an angle of 11 degrees relative to the horizontal when the scanning head is level). An SEM image of the tip is presented in fig. 4.1.

The CNT was attached to the AFM tip by bringing both to close proximity and applying voltage between them. This attaches the CNT to the tip [239]. The CNT was then shortened and welded to the tip apex using current arc (similar to [240]),



(a) Front view (b) Side view

Figure 4.1: SEM images of the probe used for the final measurements. The image shows that the CNT has been straightened and and set to the angle of 11 °. The image also shows the coating reinforcing the CNTs attachment. Image courtesy: CDI.

straightened using ion beam molding [241] and the base of the CNT and the tip were coated to strengthen the CNT attachment [241, 242]. The CNT itself was not chemically processed before this procedure. However, ion beam processing can turn the pristine CNT structure into amorphous carbon [241, 243]. This is desirable as it renders the CNT more hydrophilic and more compatible with the liquid environment. It also rounds the tip of the CNT and sharpens it to ~1/3 of its radius [244]. The manufacturer specified nominal CNT length and radius of curvature are 1 μm and 10 nm, with the minimum of 0.5 μm and 5 nm, and maximum of 1.2 μm and 15 nm, respectively. The exposed length of the CNT is typically ~200 nm after coating.

4.1.2 Molecular dynamics

A batch of molecular dynamics simulations was designed to mimic the setup described in the experimental section. To that effect, the simulations were now prepared with hard walls at the top and bottom of the simulation box in the z direction (fig. 4.2). Most of the simulations parameters were as described in chapter 3.1.

The GROMACS [139] simulation package (www.gromacs.org), version 4.5.5, was used to run the simulations. The hard walls were mimicked by placing a potential wall at $z = 0$ and the top of the box (fig. 4.2, and fig. 3.1 for comparison). A $9-3$ Lennard-Jones (LJ) potential was used to simulate the wall. This was integrated over the volume behind the wall to give a full $12-6$ LJ potential [140]. A particle density of 20 CG particles nm^{-3} for both walls was used. This roughly corresponds to a typical density of mica crystal atoms [245]. The MARTINI particle type used for atoms in the wall was N0. The use of hard walls required changing the periodic boundary conditions for the box. These were only applied in the x and y directions. Semi-isotropic pressure coupling was used as before, but this time with z compressibility set to zero [140] to avoid any changes of the box size in the z dimension. All these changes were necessary to run a

simulation with a surface mimicking a hard substrate.

Other than what was described above, all the parameters were as in chapter 3.1. MARTINI2 force field was used as before. The temperature and pressure were set to 323 K and 1.0 atm, with time constants of 2.0 ps and 10.0 ps, respectively. One significant difference was the use of the antifreeze water particles. This was done to prevent water from freezing near the wall surfaces, which was reported before [145]. A mole fraction of 0.1 antifreeze particles was used throughout the simulations presented here, as recommended in [145]. A smaller fraction of 0.05 was also investigated but turned out unstable and froze quickly, making the results unworkable. The 0.05 mole fraction simulations were discarded.

The simulation box (fig. 4.2) was similar to the one used in the previous chapter (fig. 3.1). The lipid bilayer was placed 1.2 nm, 1.5 nm, and 1.8 nm above the bottom wall (at $z = 0$ nm). This corresponds to a thin layer of water typically present between the lipid bilayer and mica in the experimental conditions [246, 247]. Different distances were used to try the effect of CG water layering due to increased ordering near the wall. This was desired, as real water usually forms layered structures near real interfaces [248, 16, 249]. While the experimentally observed water layer would usually be a little thinner, the large size of CG water molecules (corre-

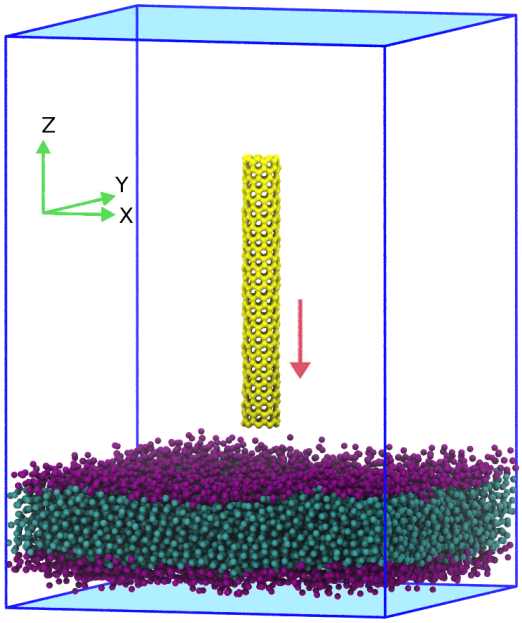


Figure 4.2: Simulation scene overview: CNT above a 14×14 nm^2 DPPC membrane patch. Yellow: CNT, purple: lipid headgroups, cyan: lipid tails. Walls indicated by the shaded box sides. Axes as labelled by the green inset. Pulling direction indicated by the red arrow. Water removed from view.

sponding to four atomistic water molecules [144, 145]) required using a slightly thicker layer of water to screen the lipids from the wall potential more effectively and allow for some disorder between the waters and lipids. The bilayer lateral size was either 14×14 nm^2 or 18×18 nm^2.

The CNT particle types used were C1, C2 and C3 which correspond to the most hydrophobic types in MARTINI force field (see [145] and chapters 2.1.3, 3). Three lipid bilayer compositions were used, consisting of pure DPPC, POPC, or POPE lipids only. The CNT was placed ~2 nm above the bilayer. The simulation box was then energy minimised and equilibrated for 2 ns with lipid z-position and full CNT positional restraints. For the production runs, the CNT was pulled down along the z axis (see red arrow in fig. 4.2) towards the lower side of the box, i.e. towards the lipid bilayer and the hard wall just beneath it. The pulling was done until the CNT reached the box boundary. Two pulling speeds of 0.01 nm ns^{-1} (1×10^{-2} m s^{-1}) and 0.1 nm ns^{-1} (1×10^{-1} m s^{-1}) were used, as in the previous chapter.

All the simulations were run using the IRIDIS computer cluster [250] and the Oxford Supercomputing Centre [251].

4.2 Results

4.2.1 AFM

With the AFM, it is possible to extract information about the interaction of the probe with the surface. The information is collected at the molecular scale, unlike with other methods (see chapter 2.3). The focus in this study is on analysing the force-distance curves [196], which represent the force experienced by the AFM probe as it approaches the surface of interest, in this case, a lipid bilayer.

Two mechanical properties have been analysed. Firstly, Young's modulus has been

extracted from the data. This is related to the stiffness of the material. This property, intrinsic to any material, dictates, along with the probe shape and radius, the mechanical response of the material and the shape of the force curve. This was investigated in order to check if the membrane stiffens or softens upon CNT approach. Secondly, breakthrough forces have been analysed. These are typical for force measurements on lipids [252, 253] and have been shown to be a signature of particular lipids or lipid mixes [252]. These breakthrough events depend on the speed of approach of the probe [254, 255], temperature [256, 257], ionic strength [258], and probe hydrophobic/hydrophilic character [259]. For any given set of conditions, the breakthrough forces are therefore related to the interaction between the bilayer and the indenter.

The only parameters that changed in the currently presented experiments were the speed of approach and character of the probe (see chapter 4.1).

Conventional probes

A typical set of force curves using the RC800 conventional probe (short lever, on DPPC) is shown in fig. 4.3. As can be seen by two breakthrough events and the extent of the force curve (10.7 ± 1.3 nm), two lipid bilayers were present. This is further confirmed by phase images (similar to fig. 4.4).

To determine the Young's modulus, the data was fitted to a contact mechanical model. Previous studies used the Hertz model to analyse their data [260]. The model [192] assumes a semi-infinite extent of the indented material and ignores all interactions but indentation. The force response has the form

$$F = a\delta^n \tag{4.1}$$

where F is the force, δ is the indentation, n depends on tip geometry, and a is is a parameter that depends on the Young's modulus, tip radius, the Poisson ratio of the

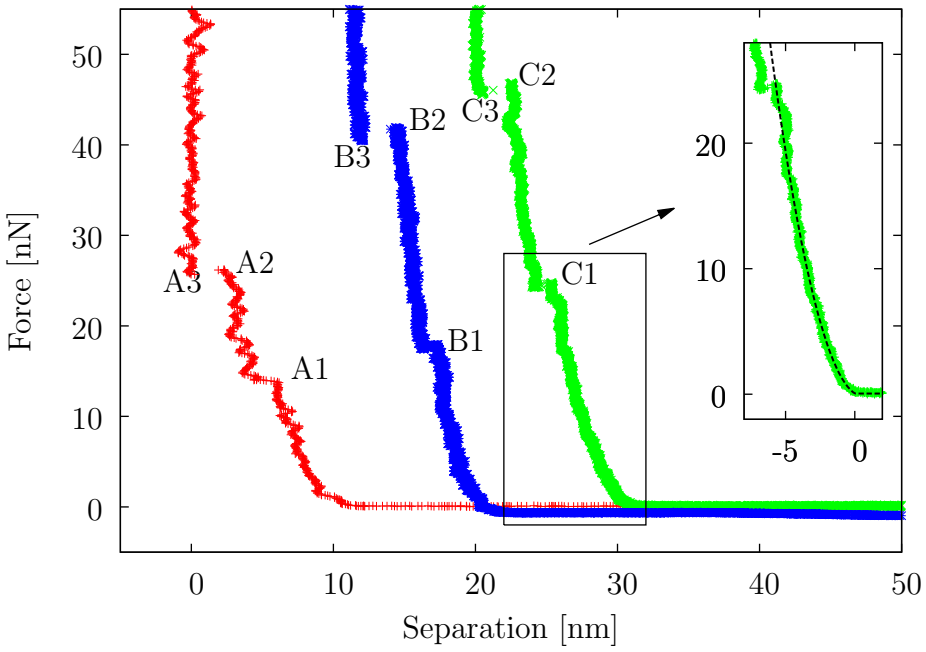


Figure 4.3: Force curves on DPPC, taken with the RC800 probe (short lever). Typical curves for different speeds shown. Red (A): fast, blue (B): medium, green (C): slow. The inset shows a part of the green curve with a fit (black dotted line, discussed in text) imposed on top. A1-C1: first breakthrough, A2-B2: second breakthrough, A3-C3: substrate level. All curves shifted along the x axis for clarity.

material [16] and n. While this is a good first approximation, it is inadequate to describe lipid bilayer indentations. The bilayer has a finite thickness and after indenting for a few nanometres on top of the surface, the effects of the hard substrate are starting to be felt [202].

The present data was fitted using the Chadwick model [203, 261], which was designed to describe the indentation of thin layers on a hard substrate with slip (i.e. the layers were not attached to the substrate), which is appropriate in this case (see chapter 2.3.3). The model was specifically meant to address the biologically relevant problems. The functional form of the interaction, for a thin layer with slip, is given by:

$$F = \frac{2\pi E R}{3h}\delta^2 \tag{4.2}$$

where F is the force response, E is the Young's modulus, R is the radius of the indenter, h is the thickness of the layer being indented and δ is the indentation depth (such that $\delta = 0$ occurs at probe-bilayer contact).

This equation was fitted to the data, with the probe radius R set to that stated by the manufacturer, and the layer height set to the height of a single lipid bilayer. Only the data between contact and the first breakthrough (i.e. before A1,B1,C1 in fig. 4.3) was used for fitting. Beyond that point, no reliable contact point could be established. An example fit can be seen in the inset in fig. 4.3. The goodness of fit R^2 was 0.97 on average. This could indicate that the model used is a good description of the data.

The Young's modulus obtained for DPPC was 66.3 ± 19.0 MPa for the RC800 cantilever and this is of a similar magnitude as the results in the previous experimental studies [262, 263, 264, 265, 260, 266].

Extracting Young's moduli from MD simulations would be difficult for a number of reasons. First, there are, to the best of author's knowledge, no suitable parameters for silicon nitride (which the RC800 tips are made of) for biologically relevant force fields. Secondly, contact mechanical models usually assume a continuous material, an assumption which breaks when atomistic systems are considered (for the purpose of this argument, CG systems can be counted atomised, i.e. not continuous). Lastly, experimental indentations are done on a much longer scale than feasible in simulations, so there would be difficulties arising from comparing near-equilibrium conditions in experiments and non-equilibrium situations in possible MD indentations. The longer data extraction times in experimental conditions mean that the values extracted are averaged much more than in simulations. A number of lengthy simulations would have to be carried out to provide a statistically significant sample size. This, in light of the arguments above, was not considered a priority at this time.

The breakthrough forces were 13.3 ± 0.7 nN, 18.8 ± 1.8 nN and 22.9 ± 2.1 nN for the

slow, medium and fast probe speeds respectively. This is in agreement with previous results for measurements under high ionic concentration [258]. The breakthrough forces increase with increasing indentation speeds, which agrees with theory and experiment [255, 254].

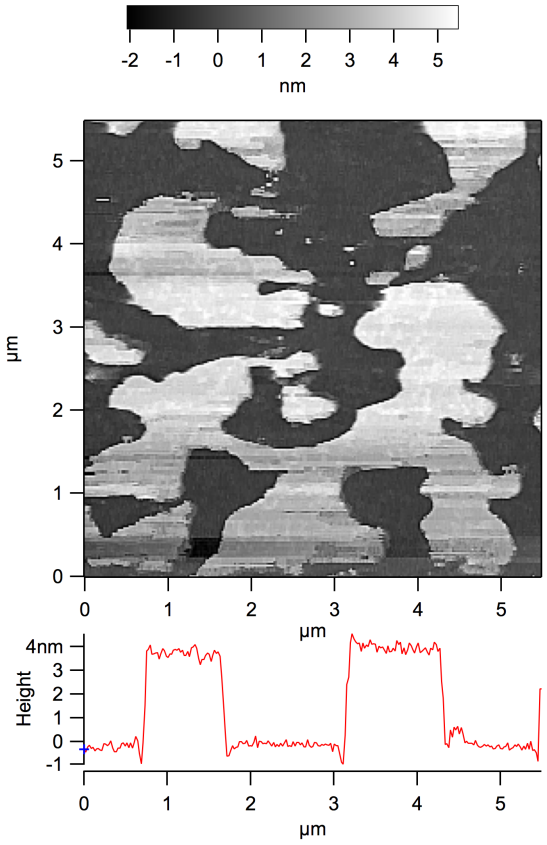
Overall, the results obtained for the experiments with the conventional AFM probe agree well with previous results. The purpose of those experiments was to establish a methodological basis for comparison with the experiments performed with the CNT probe.

CNT probe

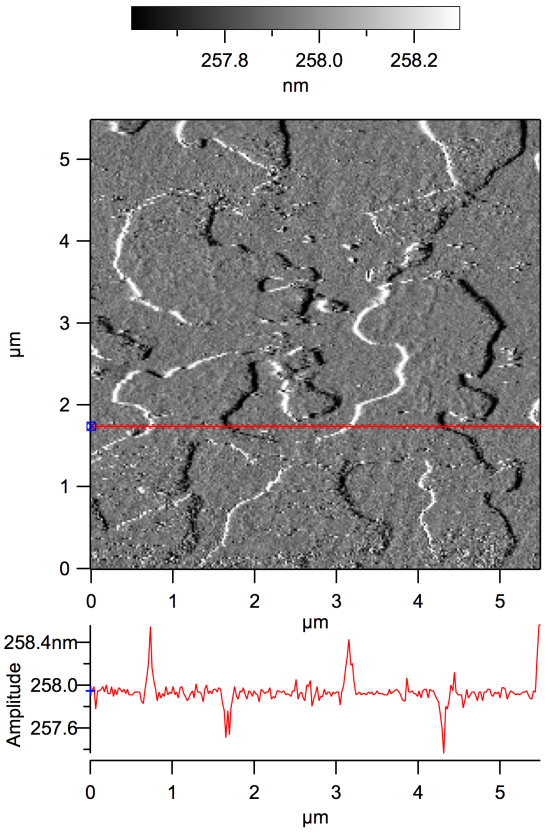
The same experiments were then repeated with the CNT probe. The area over which force data was collected is shown in fig. 4.4. A typical set of force curves is shown in fig. 4.5.

At first glance, those force curves do not differ much from the ones obtained with conventional AFM probes (fig. 4.3). However, on closer inspection, it becomes apparent that each force curve has an almost linear section immediately after the tip touches the bilayer (see inset in fig. 4.5). This is unusual for force curves on lipids and deserves closer investigation.

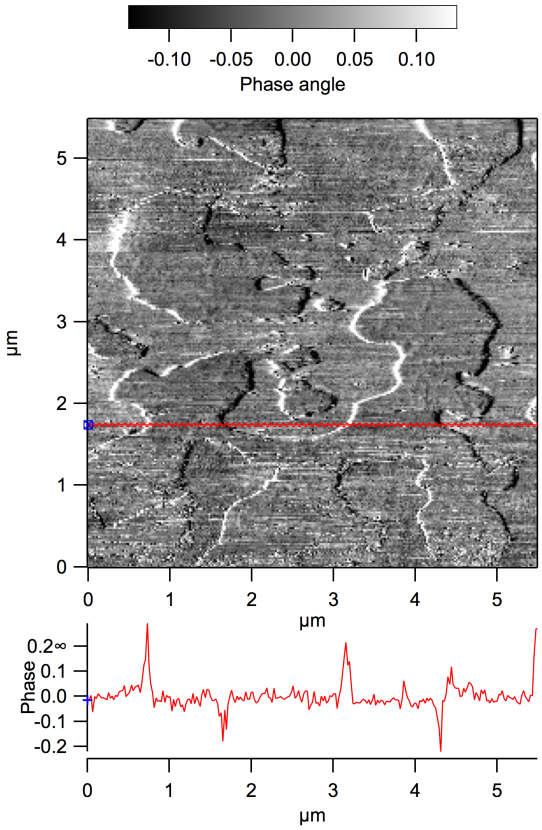
Buckling of a CNT in a CNT-modified AFM probe has been reported previously [267]. The force curves reported there did have linear sections at the beginning of the indentation region. However, the particulars of the experiments in [267] make the current situation different. Firstly, the CNTs in [267] were of the coiled type [268, 269]. Also, the CNT in [267] does not appear to be positioned perpendicular to the sample surface. This is in contrast to the experiments described here (see chapter 4.1.1). This is an important difference. While CNTs can easily undergo an elastic bending [270, 271, 74], they do not buckle as easily when subject to an axial force [270, 272, 271, 273, 74], as is the case here. Moreover, in this work, additional force curves were taken after the main



(a) Height



(b) Amplitude



(c) Phase

Figure 4.4: AFM topography images taken with the CNT probe. Images taken just before force measurements. Force measurements taken on the elevated patches in fig. 4.4a. Phase image (c) shows the elevated islands and the flat surface underneath are actually the same material, confirming multiple layers of lipid.

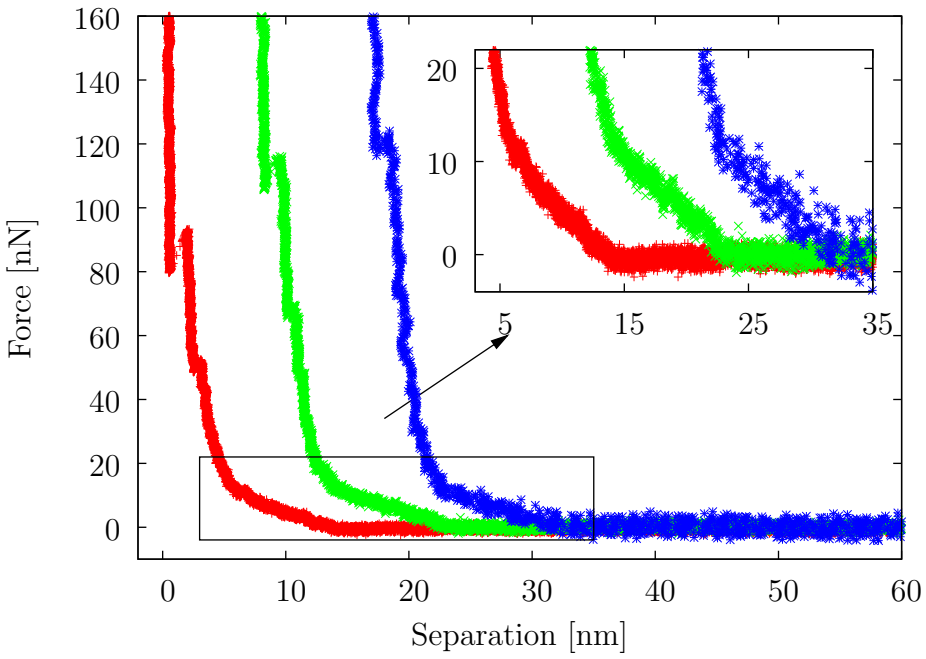


Figure 4.5: Force curves taken with the CNT probe. Typical curves for different speeds shown. Red (A): fast, blue (B): medium, green (C): slow. The inset shows a part of the green curve with a fit (discussed in text) imposed on top. A1-C1: first breakthrough, A2-B2: second breakthrough, A3-C3: substrate level. All curves shifted along the x axis for clarity.

lipid indentations. They were captured with the AFM cantilever driven closer to the surface than for the initial force measurements. This increased the load on the CNT tip. As can be seen in fig. 4.6, a sharp drop in cantilever deflection (accompanied by a sharp spike in amplitude) was observed at those deeper indentations. This drop (~200 nm) corresponds to the exposed length of the CNT at the end of the modified tip, as reported by the manufacturer (see chapter 4.1.1). This confirms the attachment of the CNT after the force measurements on lipids. As the threshold force required to buckle the CNT was higher and the cantilever vertical position lower than for the lipid indentations, this shows that the CNT bending occurred beyond the load at which the indentations were performed. This confirms that the CNT was straight throughout the region of interest. Bending of the CNT throughout the experiment cannot therefore explain the shape of the force curve.

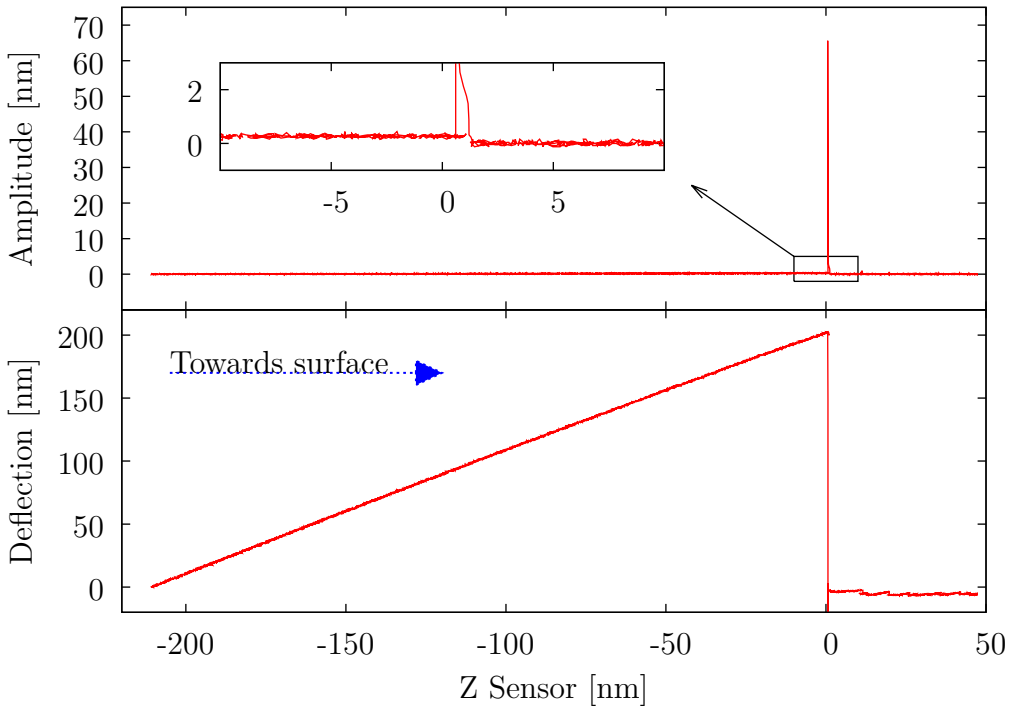


Figure 4.6: Force curve taken after registering force curves on lipids. The AFM probe was driven closer to the surface, increasing the load on the tip. The drop in deflection (of the same magnitude as the exposed end of the CNT) and a sharp peak in amplitude confirm CNT attachment.

Electrostatic interaction can be safely ruled out as a possible explanation. The shape of the curve is not of the form expected for electrostatic interactions (see [16] and chapter 2.3.3). The average extent of the seemingly linear region (7.3 ± 1.5 nm) is larger than any reasonable electrostatic force would have. The forces involved (average maximum of 13.3 ± 4.0 nN in the linear region) are also larger than what would be expected of electrostatic interactions. Furthermore, the ionic strength of the buffer effectively reduces the Debye length (see [16] and chapter 2.3.3) and the extent of the electrostatic double layer (further increase in buffer strength produced no significant Debye layer reduction). The same buffers were used in both the CNT and conventional probe experiments. No significant double layer force was observed in the conventional probe experiments. It is therefore reasonable to assume that this is not the case here either.

The possibility of single (i.e. non-bilayer) lipids adhering to the CNT tip can probably

be ruled out. This would happen after the CNT touched the lipids for the first time (or came in contact with free-floating lipids from the buffer). If that was true, similar reasoning could be applied to the bulk of work measuring the force curves on lipids using conventional probes. As such lipid adhesion is not considered in previous work, it will not be assumed here either. This is done to simplify the comparison of force curves.

Another possible explanation could be the shape of the probe. In the Hertz model, the force is linearly proportional to indentation for a flat punch indenter ($n = 1$ in eqn. (4.1)). This scenario is, however, unlikely. Firstly, as it has been discussed earlier in this chapter and in chapter 2.3.3, the Hertz model is not an appropriate description of indentations at this microscopic scale. Secondly, it is doubtful that the CNT tip had a flat shape profile. Moreover, the sharpening of the tip is also not expected to leave the free end of the CNT flat. A more rounded, spherical shape is more typical [244]. Further, a non-linear force response is restored after a linear portion of indentation. This makes the flat punch Hertz-like indentation an unlikely candidate to explain the shape of the force curves observed.

Another possibility could be related to CNT compression under an axial load. The Young's modulus of CNTs [73] is usually at least a few orders of magnitude larger than that observed for a lipid membrane (see the result earlier). This means that the compression of the CNT in the axial direction is much smaller than that of a lipid membrane. Therefore, the observed cantilever deflection comes almost entirely from the bilayer, making the compression of the CNT an unconvincing explanation of the data.

To address the shape of the force curves, molecular dynamics simulations of a CNT indenting supported lipid bilayers were carried out.

4.2.2 Molecular dynamics

MD simulations of a lipid bilayer on a hard substrate were performed. They were carried

out with the same parameters as in the previous chapter (see chapter 3.1 and 4.1.2). The parameters were only changed where necessary for the set up of a hard wall (see chapter 4.1.2). The CNT was pulled towards the lipid bilayer as before. Such steered molecular dynamics (SMD) is conceptually equivalent to an AFM indentation. In an AFM experiment, a probe is driven towards a sample at a constant speed and the cantilever arm is deflected proportionally to its spring constant. In SMD, a CNT is pulled towards the bilayer at a constant speed by means of a virtual spring (see chapter 3.1). The resultant force is the difference in position between the probe (either the CNT in simulation or cantilever tip) and its drive (either an AFM piezo or a virtual point in SMD) times a spring constant. This allows comparison of the experimental and simulational force curves.

Some typical force curves obtained in the simulations are shown in fig. 4.7. There are a few things to note. Firstly, there is a slight increase in the force felt by the CNT as it approaches the bilayer. This suggests an energy barrier. However, for a hydrophobic CNT (as is the case here), a barrier would not be expected [222]. This peak seems to arise from the immediate repulsion of the hydrophobic CNT CG beads and lipid headgroups *before* the formation of the meniscus and lipid creep. It is most likely the response to mechanical contact before piercing. Secondly, there is a drop in the force value and the force is negative, as if the CNT was attracted to the bilayer. Then, there is an apparently linear increase in force, followed by peaks in force due to the layering of water at the box wall (fig. 4.8). This trend has been observed in simulations using the Bond force field [230] and CHARMM force field [229]. This is very similar to what has been observed experimentally.

Extracting Young's moduli from the simulations would be, at best, inconclusive, as described earlier. It could be possible to attempt extraction of bending moduli from the simulations [221, 225]. They are, however, not directly comparable to Young's moduli

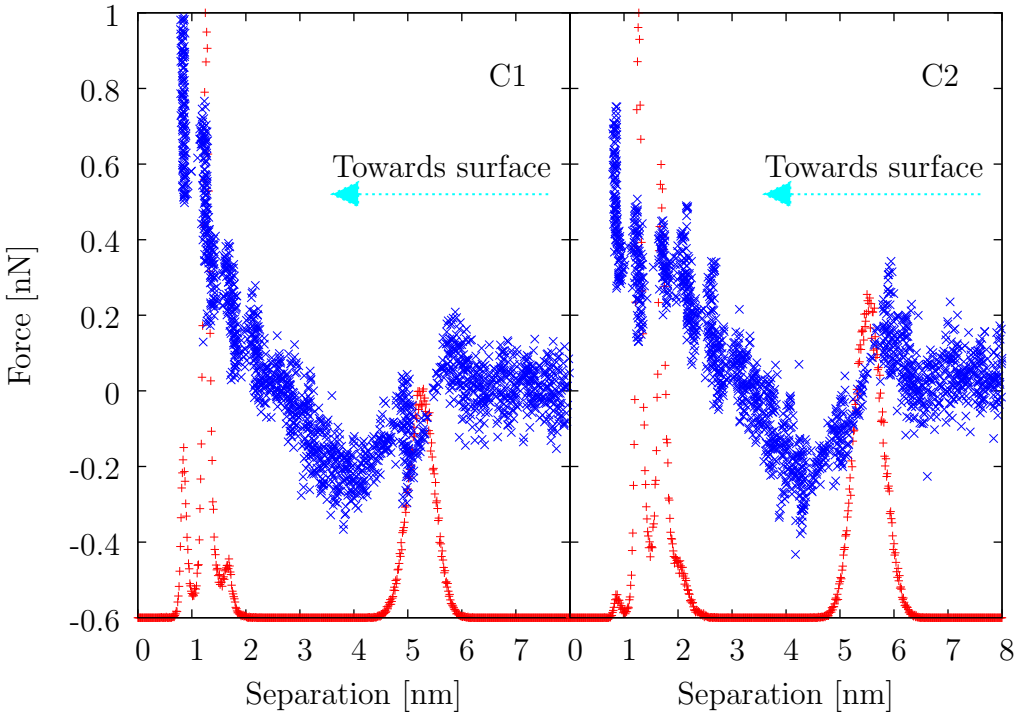


Figure 4.7: Typical force curves obtained in simulation. CNT particle type (see introduction and previous chapter) as indicated in sub-captions in top right corners. Pulling direction indicated by cyan arrow. Blue is the force experienced by the CNT as it penetrates the bilayer. Red is the density of the phosphate groups at the beginning of the simulation (arbitrary scale, not shown). Separation is measured from the wall (bottom wall in fig. 4.2, zero at the wall). Lipid headgroup density is split into a few sharp peaks due to layering of water and lipid molecules near the interface (see chapter 2.3.3, 4.1.2 and fig. 4.8). Sharp drops in the force near the wall correspond to the probe breaking through those layers of solvent near the substrate.

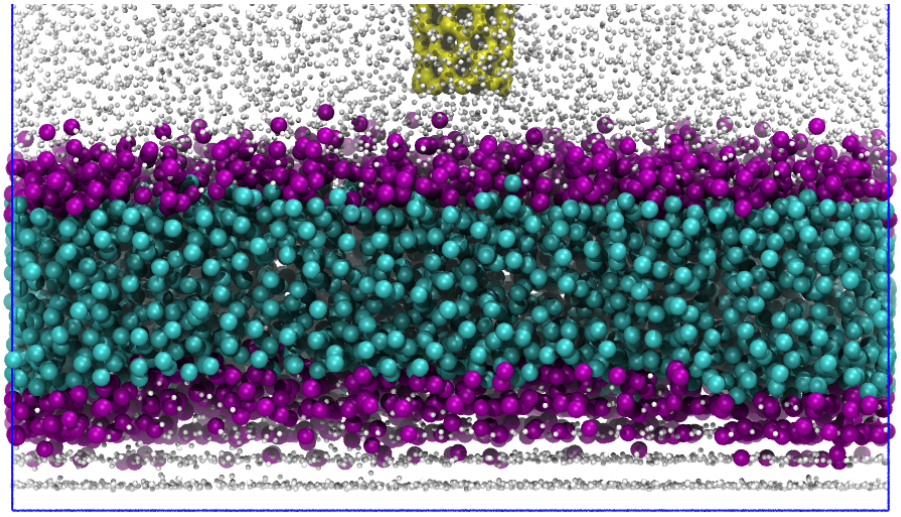


Figure 4.8: Water layering near a wall. Water shown as grey spheres. Cyan: lipid hydrocarbon tails, magenta: lipid headgroups, CNT shown in yellow in the background. First few layers of water near the wall are layered due to surface proximity. This layering promotes layering of the first few lipid particles. Lipid layering is not as effective as for solvent.

and there is no obvious conversion method between the two properties. Due to the limited size of the simulation box, these numbers would not be accurate, as argued in [225].

4.3 Discussion

The simulational data does seem to qualitatively agree with the experiment. There are some differences that still need to be addressed.

Firstly, the shape of the initial, seemingly linear, part of the force curve. Both in this work and in other work for CNT/bilayer systems in the Bond force field [230], there is a dip in the force just after the CNT pierces the membrane and crosses over the headgroup region. This is not observed experimentally. However, the simulations suggest that the value of this dip is of the order of a few hundred piconewtons. This is of a similar magnitude as the thermal vibrations of the AFM tip at room temperature and such an

event could easily be lost in the thermal noise. Unfortunately, the phase data recorded along with the force curves is very noisy and cannot be used to determine if there was a change from repulsive (positive force) to attractive (negative force) regime.

On the other hand, the force data in [229] does not seem to show this dip in force. This is most likely related to the different force field they used in their work. The common feature of all these simulations is this apparently linear force as the CNT pierces the bilayer.

The average slope of a linear fit in that region calculated from simulations in this work is 0.27 ± 0.11 nN nm^{-1}. The estimated values in [230] and [229] seem to be of similar magnitude ($0.1 - 0.2$ nN nm^{-1} and $0.5 - 1.5$ nN nm^{-1} respectively). The experimentally determined linear fit slopes are 1.4 ± 0.2 nN nm^{-1} (with the goodness of fit $R^2 = 0.94$ on average). Given the differences in probe approach rates in simulation and experiment, these results are not in significant disagreement. The experimentally recorded linear region extends to indentations of 7.3 ± 1.5 nm and maximum forces of 13.3 ± 4.0 nN. This suggests that the measured interaction extends past a single lipid bilayer. This is important as it implies that a single lipid bilayer is not a sufficient barrier for a CNT.

Beyond the linear region in the experiment, a more typical behaviour seems restored. The characteristic breakthrough forces appear again. A force curve shape not dissimilar to that observed for conventional probes reappears. That region has not been fitted with any model as it is not possible to determine with confidence a good value for any contact point. It is possible that this behaviour is re-established because of the very reason that gave rise to the linear force response. As demonstrated in the previous chapter, in simulation, lipids start creeping up the CNT to shield it from unfavourable interactions with water. A similar scenario can be taking place here: Lipids shield the CNT from the interaction with the solvent upon contact. After penetrating the first lipid layer, the

CNT is at least partially screened from the solvent upon reaching the second lipid layer and no more such shielding needs to take place. It might not be possible for the lipids from the second layer to cross over into the first bilayer due to geometric confinement caused by the proximity of the lipid layer above it. This could lead to restoration of the indentation behaviour. While a possible explanation of the data, this is speculative and needs to be investigated further.

It has been shown in a previous study [259] that by using a hydrophobically functionalised probe (functionalised with mercaptohexadecane, or $-CH_3$ groups, in practice) the breakthrough force on lipids is effectively reduced to zero and the probe experiences virtually no force until it reaches the substrate. The hydrophobic CNT in this study does not give rise to this effect. The force increase is monotonic and apparently linear. It can be therefore inferred that what was observed here is related specifically to the CNT-lipid interaction and not to the hydrophobic character of the CNT.

Unfortunately, is it not possible to calculate Young's moduli from the simulation data. This makes the comparison between simulation and experiment unfeasible. Simulations can provide the value of bending modulus [225, 274, 275, 276, 277]. There is, however, no good relation between Young's modulus and bending modulus. Additionally, the bending modulus in simulation is calculated from the analysis of free membrane undulations (with [225], or without a CNT [225, 274, 275, 276, 277]). Young's modulus, however, represents a relation between stress and strain, and in experiment it is determined by physically pressing the membrane with a probe. The simulations in this chapter were carried out to mimic a typical experimental setup. The results, along with the experimental data from this chapter, suggest that a CNT interacting with a bilayer does not represent a classical indentation, where both the sample and the indenter deform on contact. There is little justification or purpose to calculate a classical property in a non-classical situation.

4.4 Summary

It has been shown experimentally that the interaction of CNTs with lipid membranes gives rise to new effects that, to the best of author's knowledge, have not been reported before. A monotonic, apparently linear increase in force upon CNT-lipid contact is a particular feature that differentiates the CNT-lipid interaction from the typical lipid-AFM probe interaction reported before. This cannot be explained in terms of previously reported phenomena and can be thought as specific to the CNT-lipid interaction.

A set of MD simulations was carried out to try to explain the observed, experimental results in more detail at a molecular scale. These simulations were conceptually equivalent to the AFM measurements carried out. The simulational results show some qualitative agreement with experiment. In particular, they show a linear force response when lipids are indented with a CNT.

Despite subtle differences in simulations and experiment, the main features are preserved across both. This shows that molecular dynamics is an adequate description of the interaction, even at the coarse-grained level of detail, and can be used to shed extra light onto the process. Moreover, the experimental verification of simulation results confirms that coarse-grained simulation methodology (using the force fields tested here) may be used to describe the interaction and justifies the use of MD as a useful tool to further analyse it.

5 MD simulations of free CNT-lipid bilayer interactions

The work described so far included investigating CNT-bilayer interactions under controlled conditions (either in simulation or experiment). In this chapter, the CNTs were largely unconstrained, which is in contrast to the results presented in the previous chapters, where the CNTs were position-restrained and only steered MD (SMD) simulations were carried out. Here, the CNTs are free to diffuse with no constraints in a lipid bilayer, and can interact with it after being randomly placed in the solvent. This is to investigate the behaviour of CNTs freely floating in solution and diffusing in a membrane, as would be the case for drug delivery systems and other nanotechnological applications. Some surprising effects were observed, in particular for the case of free CNTs in solution, where their preferred location after interactions with the bilayer was different from expectations.

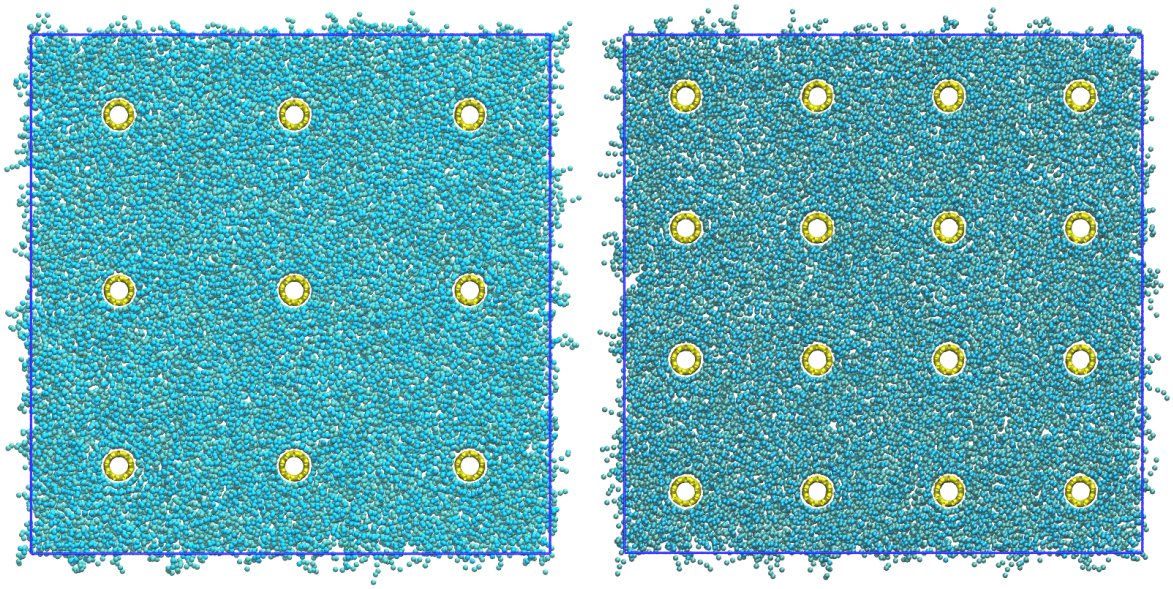
5.1 Methods

Molecular dynamics simulations were prepared with parameters as described in the previous chapters. A coarse-grained methodology (see chapter 2.1.3) using the MARTINI2 force field [145] was used. MARTINI2 (MARTINI, version 2.1) was used, unless stated otherwise. When MARTINI2 was used, the CNT particle type was C1-C5 (see chapters

2, 3, 4). All the systems were simulated using GROMACS (www.gromacs.org) [139], version 4.5.3.

A number of systems were set up, where short (length ~6 nm, radius 0.7 nm) (18,0) CNTs were embedded within the bilayer, with their axes perpendicular to the bilayer plane. A matrix of either 1×1, 2×2, 3×3, 4×4 equally spaced CNTs was placed in a pre-formed DPPC bilayer with lateral size of 30×30 nm^2. This choice was made to investigate the effect of CNT crowding in a membrane at various concentrations. The equal spacing was merely a convenient starting point for the analysis of the subsequent diffusion as the CNTs were expected to move away from this configuration. It also averaged out any possible CNT-CNT interactions, at least initially. The system with just one CNT is a general case of a very sparse CNT concentration. In general, it is difficult to talk about any mass or molar concentration of CNTs, as, due to their varied size and unlike other molecules such as specific proteins, they do not have a well-defined mass. A unit concentration was used instead. A top side overview of the systems can be seen in fig. 5.1. The box height was typically ~10 nm, which was enough to accommodate the lipids, CNTs, a layer of water on each side of the membrane and ensure there were no self-interactions between the periodic images across the box boundary. Temperature and pressure coupling were set to the same values as in the previous chapters.

System equilibration was carried out in a few steps. A total of five 1 ns equilibrations, with varying levels of restraints, were performed before the main MD production run. After energy minimisation, the system was equilibrated for 1 ns with full CNT positional restraints and the lipids restrained in the z direction. This was done by attaching a virtual spring with stiffness $k = 1000$ kJ mol^{-1} nm^{-2} to the restrained atoms along the relevant axes (all x, y, z directions for the full CNT restraints and the in the z direction for the lipid headgroups restraints). This way the lipids could still move in the plane of the membrane to reach a semi-steady state around the CNT. Then, the restraints on the



(a) 3×3 (b) 4×4

Figure 5.1: A top side view of the systems as set up, showing a (a) 3×3, (b) 4×4 matrix of equally spaced CNTs embedded in the lipid bilayer. Yellow: CNT, cyan: DPPC bilayer. Simulation box outline in blue. The bilayer defines the xy plane. Z-direction perpendicular to the bilayer, along the CNT axes (perpendicular to paper). Box size: 30×30 nm^2.

lipid were eased (by reducing the parameter k in the z direction to 100 kJ mol^{-1} nm^{-2}) and the systems were equilibrated for a further 1 ns, after which the restraints on the lipids were lifted altogether and the system was further equilibrated for another 1 ns. Following this, the restraints on the CNTs were eased by reducing the spring constant k holding them in place to $k = 100$ kJ mol^{-1} nm^{-2}, much like for the lipids earlier, and another 1 ns equilibration was run. Finally, the restraints on the CNTs were lifted altogether and the system was equilibrated for another 1 ns. The total equilibration time, with various levels of restraints on the molecules, was 5 ns. After this, a production run of 2000 ns was carried out. Each pre-equilibrated system was simulated three times, each time with a different seed for the initial velocity generation.

Another batch of simulations was prepared. For this set, the particle type of the carbon rings at either end of the CNT was set to N0 (see chapter 2.1.3 and fig. 5.2).

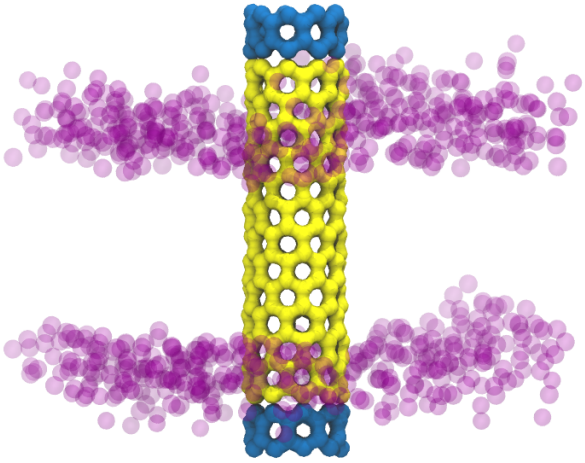


Figure 5.2: Overview of the CNT with hydrophilic ends. Yellow: CNT, blue: modified CNT ends, purple: lipid headgroups. Lipid tails not shown for clarity. The ends of the CNT were modified by changing the particle type in the CNT representation to a more hydrophilic kind (see text). Two zig-zag carbon rings (corresponding to one layer of the hexagonal grid) at the end of the tube were modified. The CNT was embedded within the bilayer as shown by the lipid headgroup density.

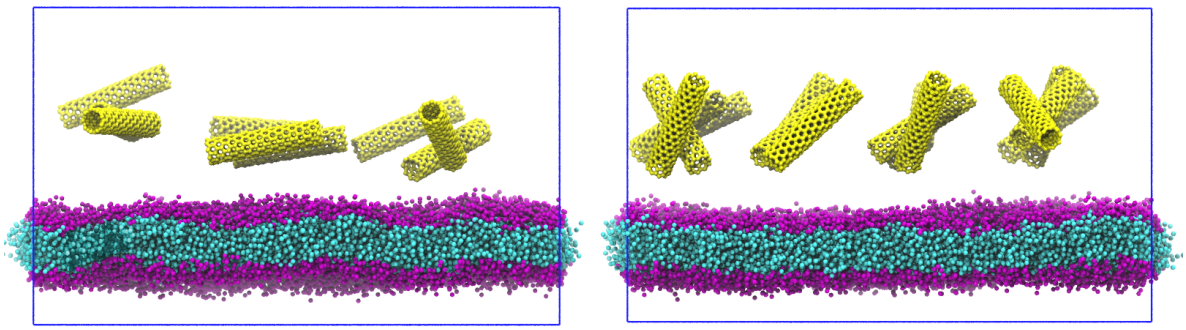
This is the same particle type as for the glycerol group in the MARTINI representation of DPPC. The CNT was free to move in all directions (no restraints). This was done to investigate the possible use of the CNT as a nanopore. Whether such a pore would be feasible in experiment is uncertain due to the energy barrier on insertion (seeing as a non-hydrophobic CNT end would have to be translocated across the bilayer). This investigation was carried out to see how such a lab-designed pore would work once within a bilayer and whether any attempt to design was sensible.

A third batch of simulations was prepared as above. The only difference was that the CNT restraints in the z direction were never lifted, either during the equilibration or production runs. This way, the CNT was free to move in the xy plane. All other parameters remained the same as in the simulations described above. This was carried out to investigate, whether restrained CNTs would behave like proteins. Such vertical position restraint is most likely not achievable experimentally. This simulation was done in order to investigate how close the behaviour of CNTs can be correlated to the behaviour of transmembrane proteins [278, 279].

A fourth, short batch of simulations was prepared in light of the results obtained from the set with restrained CNTs above. A short CNT (5 nm length) was pulled towards a small (8×8 nm^2) patch of DPPC bilayer (much like in the previous chapters) and

restrained immediately after touching the lipids. This set was prepared in the Bond force field and the CNT particle type was set to C, as in chapter 3.

Finally, a set of simulations was prepared, where arrays of 3×3 or 4×4 CNTs were placed *outside* the lipid bilayer. The CNTs were arranged on a grid above a preformed 30×30 nm^2 bilayer, but their axes were pointing in random directions (fig. 5.3). This is different from all the previous simulations, either in this or previous chapters, where the CNTs were always positioned with their axes perpendicular to the bilayer plane at the start of the simulation. The positioning here was semi-random, with two sets of CNTs pointing predominantly with their axes in the off-perpendicular direction (fig. 5.3b), and two sets of simulations with their axes slightly off the plane of the bilayer (fig. 5.3a). They can be thought as roughly vertical or horizontal (fig. 5.3) and they will be referred as such for the rest of this chapter. The exact orientation of the CNTs was not important as the general trend was investigated. The overall behaviour was the property looked at. In summary, two each of the following starting structures were prepared: 3×3 'vertical', 3×3 'horizontal', 4×4 'vertical', 4×4 'horizontal', where vertical and horizontal refers



(a) 3×3, horizontal (b) 4×4, vertical

Figure 5.3: An overview of the simulation boxes with the CNTs outside the lipid bilayer. Yellow: CNTs, purple: lipid headgroups, cyan: lipid tails. The CNTs were placed outside the pre-formed lipid bilayer in a grid of 3×3 or 4×4 CNTs like in (a) and (b), respectively. The CNT axis orientation was semi-random, with the CNTs lined predominantly in the (a) off-horizontal or, (b) off-vertical direction.

Simulation	Diffusion	Hydrophilic ends	Restrained	Halted	Free in solution
Restraints	No	No	Yes	Yes⋆	No
Initial CNT location	Inside	Inside	Inside	Outside	Outside
Initial CNT orientation	Perpendicular	Perpendicular	Perpendicular	Perpendicular	Pseudo-random
CNT particle type	C1-C5	C1-C5	C1-C5	C†	C2
Simulation time	2000 ns	2000 ns	2000 ns	200 ns	2000 ns

Table 5.1: Summary of the simulations carried out for this chapter. ⋆CNT restrained after touching the bilayer, †Bond force field, as opposed to MARTINI2.

to the general orientation of the CNT arrays as described above (fig. 5.3). Each of those starting structures was run four times (giving a total of 32 simulations), each time with a different seed for the initial velocity generation. For this set of simulations, only the C2 particle type from MARINI2 was used for the CNT (see chapter 2.1.3). This set of simulations was prepared to investigate how the CNTs would interact with a membrane from the intercellular medium and whether they would get across the lipid bilayer and how they would behave on physical contact.

A summary of the simulations prepared can be seen in table 5.1. All the simulations in this chapter were run on the Iridis computing cluster [250].

5.2 Results

5.2.1 Diffusion

A few things were observed in the first batch of simulations. The first effect was observed in the equilibration runs in which the restraints on lipids were lifted but the CNT restraints were still in place. In the simulation boxes as set up, the CNTs were embedded in a flat bilayer, such that the ends of the CNT would point out of the bilayer and be exposed to the surrounding water. In the present situation, after the restrictions were lifted on lipids, they started coating the exposed parts of the bilayer (fig. 5.4). By doing so, they increased the thickness of the bilayer around the CNT.

This effect is akin to the lipid creep observed in chapter 3. There, the lipids would form a meniscus around a CNT when it started piercing the bilayer. Here, the situation is slightly altered, as the CNTs were not moving, so the dynamics is different and the meniscus is formed on both sides of the bilayer. It appears that, in both situations, the lipids adjusted their configuration to shield the CNT from the surrounding solvent.

During the last equilibration run, when the CNTs were unrestrained, and during the production run, the CNTs all rotated towards the hydrophobic bilayer core (fig. 5.5). The turning occurred within $\sim 20 - 40$ ns (no longer than ~60 ns). Once rotated, the

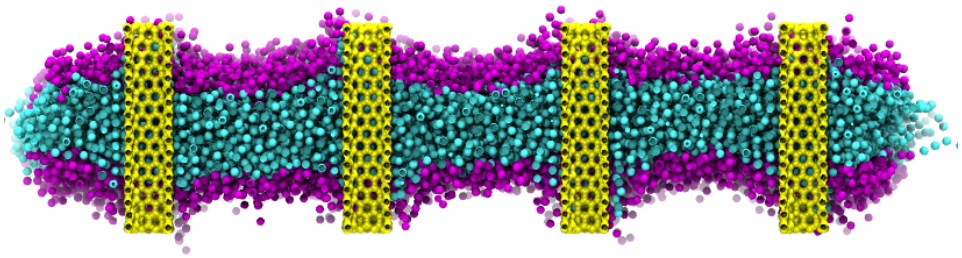


Figure 5.4: A cross section of the system after equilibration with the CNT positions restrained in all directions. A thickening of the bilayer around the CNTs can be seen. The CNT restraints were released in further equilibration and production runs.

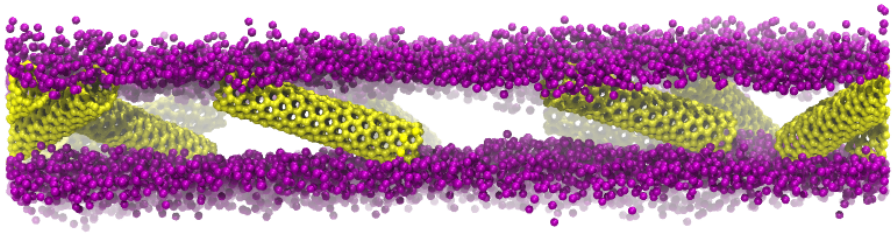


Figure 5.5: System overview after an equilibration run with CNT restraints released. Yellow: CNTs, purple: lipid headgroups. Lipid tails removed from view. The CNTs rotated towards the hydrophobic core of the bilayer, as in [225].

CNTs generally maintained their angle with respect to the z axis (perpendicular to bilayer plane) throughout the simulation (fig. 5.6). An overall average angle to the z axis was 79.4 ± 5.5 °. There was some slight deviation from the average throughout the simulation for each nanotube, but it was not significant. Such tilting is reminiscent of protein tilting to match the hydrophobic length of the bilayer [280, 281, 282]. When interpreted in such way, this behaviour is not surprising.

The angle with the x axis (representing a projection of the CNT axis onto the bilayer plane to show rotation) did not stay fixed and varied largely, as can be seen in fig. 5.7. The large deviation in this projection angle seems to support the results in [225], where no pairwise correlation between CNTs orientations was found.

In the simulations where the CNT ends were made hydrophilic, the angle between the CNT and the z axis was lower, and at 69.7 ± 4.4 ° it was closer to the bilayer normal. This is not surprising, considering the shorter hydrophobic length of the CNT (requiring less tilting to match the hydrophobic length of the bilayer) and the fact that the CNT ends were more hydrophilic (fig. 5.2), and therefore wouldn't readily mix with the bilayer core. An overview of the tilting angles for both the fully hydrophobic (i.e. no hydrophilic ends) and 'hydrophilic' (i.e. with hydrophilic ends) CNTs are shown in fig. 5.8.

There were slight variations in this tilting angle depending on CNT particle type, and CNT concentration in the bilayer (which depends on the initial CNT array size). This is

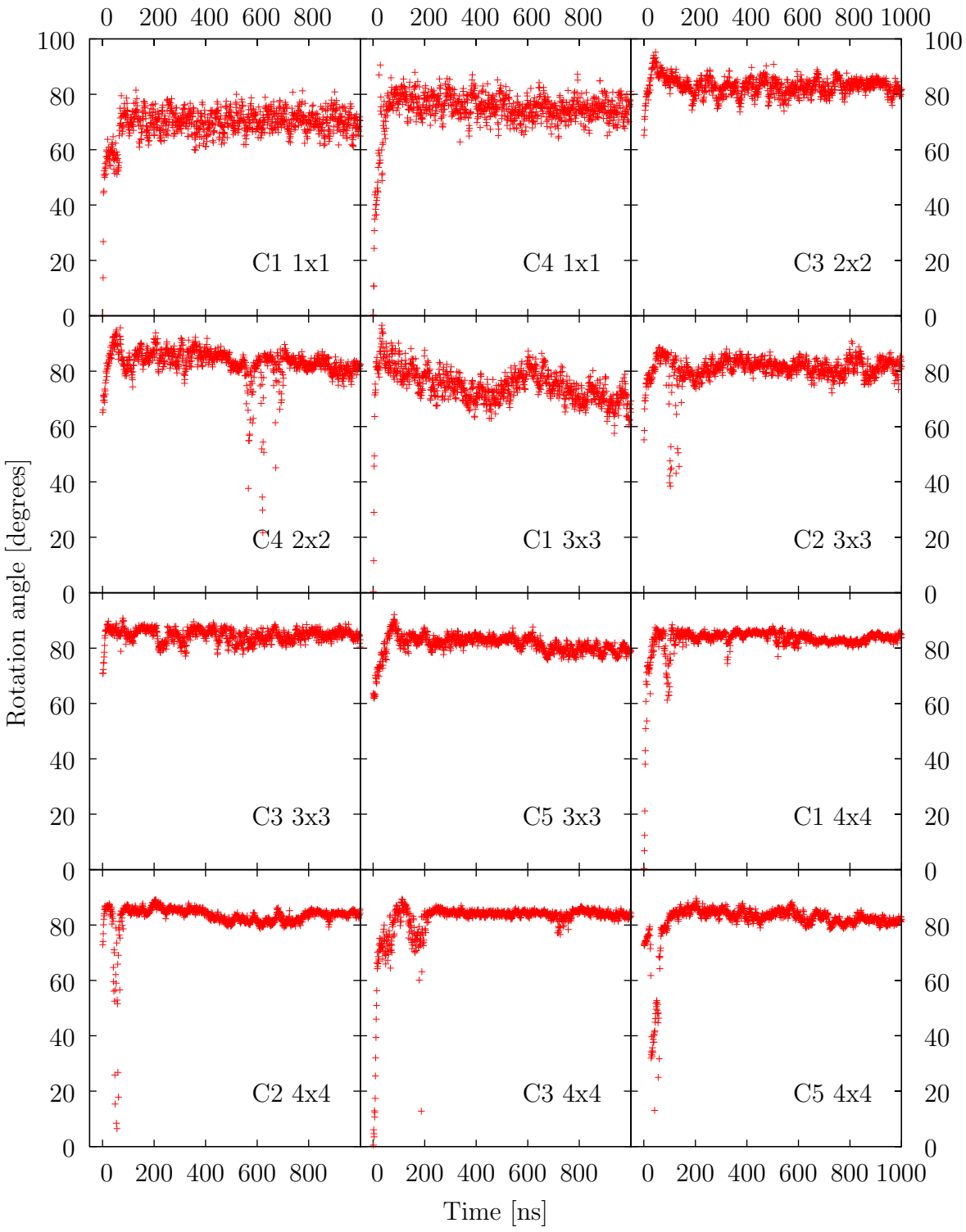


Figure 5.6: Time evolution of the angle between the CNTs and the z-axis for sample CNTs. After rotation and full system energy minimisation (~200 ns), the angle tends to remain stable. Array size and CNT particle type as labelled.

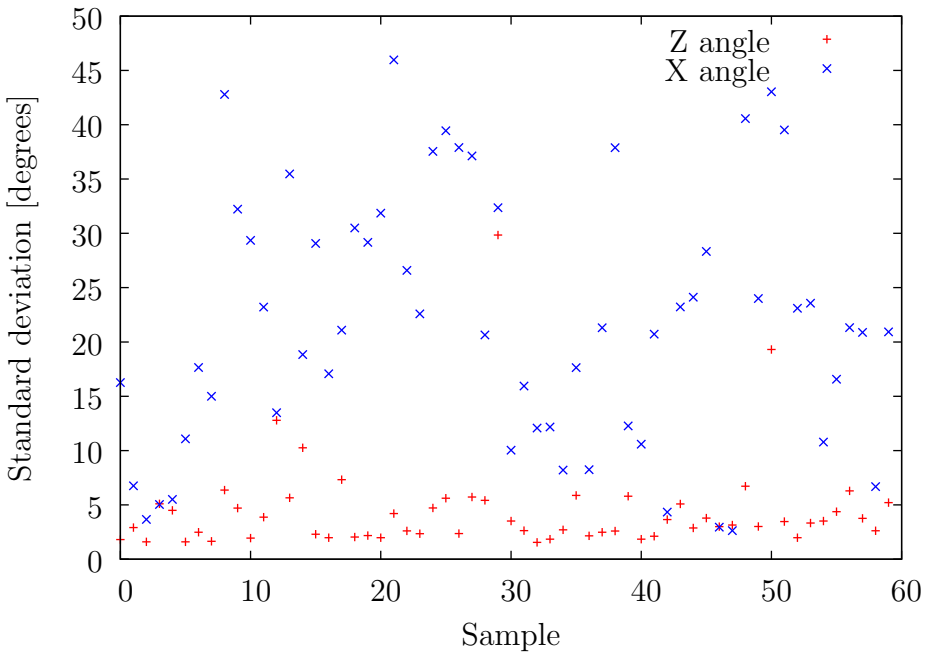
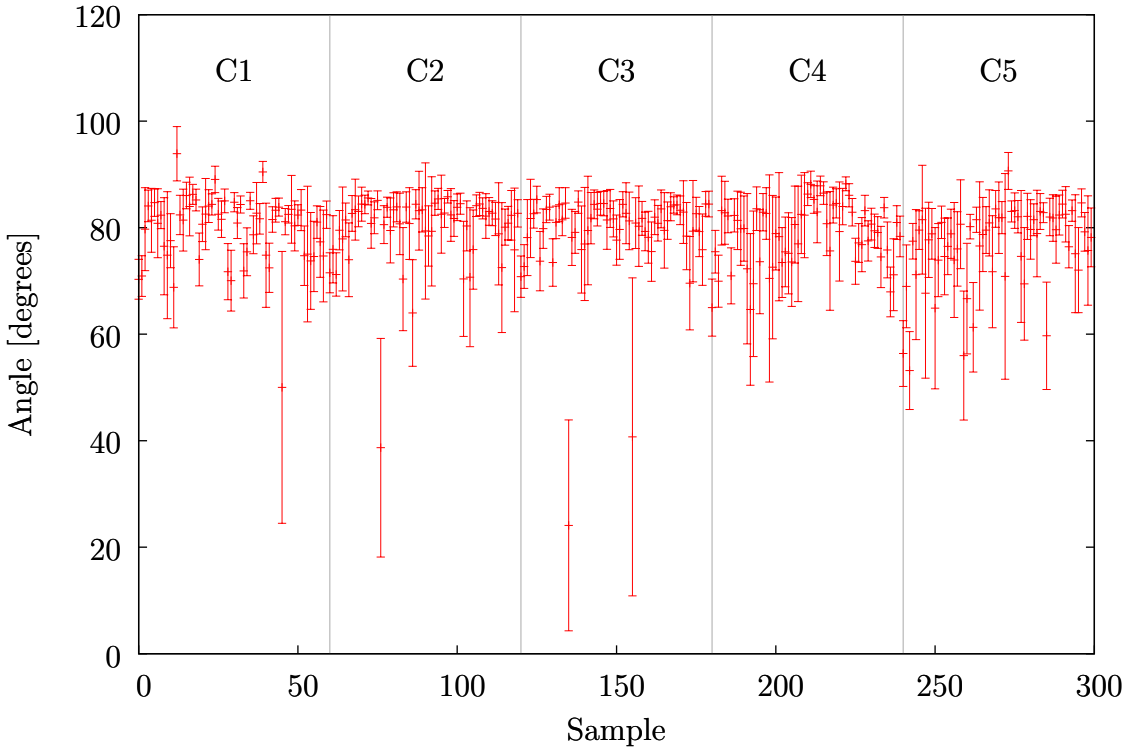
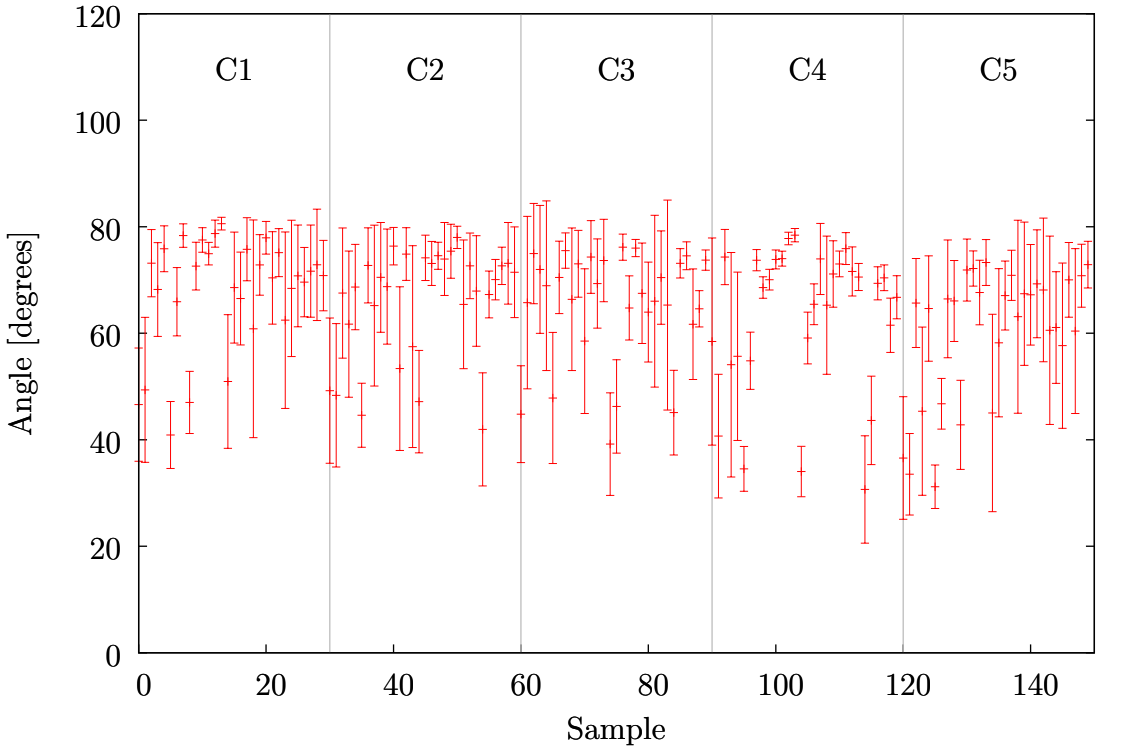


Figure 5.7: Comparison of the standard deviations of CNT projections onto the z-axis and x-axis. As can be seen, the z-direction stays relatively close to the average for each CNT, whereas the in-plane direction (represented by the projection onto the x-axis) of the nanotube changes significantly.



(a) Hydrophobic CNT



(b) CNT with hydrophilic ends

Figure 5.8: Average angles each CNT made with the z-axis after rotation for the (a) fully hydrophobic CNTs, and (b) CNTs with hydrophilic ends. Average angles with their standard deviations plotted. The measurements where the angles differ largely from the average are for the simulations where the CNT rotated towards the vertical during the simulations, therefore lowering the average and increasing the standard deviation. These were not large in number and the general trend for the CNTs was to rotate and keep their direction throughout the simulation run. CNT particle type used as labelled in the regions delimited by the grey lines.

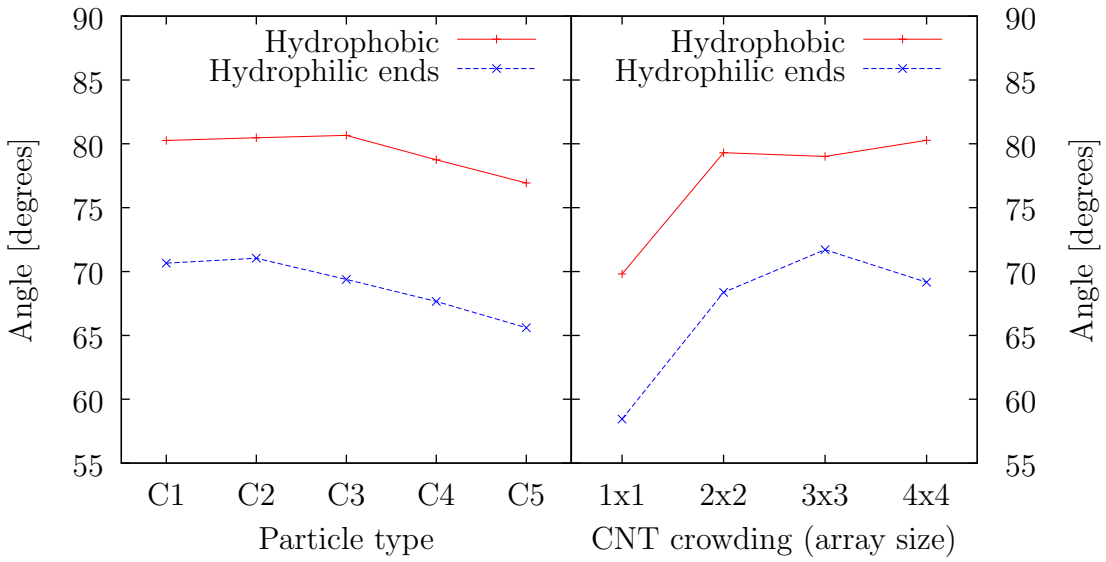


Figure 5.9: Average angles between CNTs and the z axis (bilayer normal). Each point represents an average for all relevant points, e.g. C1 represents the average of all CNTs with bead type C1, but it averages over all CNT array sizes.

illustrated in fig. 5.9. A weak dependence can be seen, whereby the tilting angle decreases (i.e. the CNT moves towards the bilayer normal) with decreasing hydrophobicity. This is to be expected, as a strongly hydrophobic particles would need more screening from the solvent outside the membrane, and stronger tilting towards the bilayer core would achieve the required effect. Interestingly, the CNT tilt seems to decrease for the systems with just one nanotube. No clear explanation is currently available for this effect.

The presence of CNTs does disturb the flow and diffusion of lipids in the bilayer. This is due to the exclusion of volume from the space that would normally be occupied by the moving lipids. Such crowding effects have been observed before for proteins [283, 284]. The slowing of lipids occurs up to around ~5 nm from the CNT (fig. 5.10), where the average square displacement of lipids approaches the values appropriate for each crowded membrane. To quantify that, the average square displacement of lipids was calculated in 1 nm contours around the CNT. Displacements in regions $0-1$ nm, $1-2$ nm, $2-3$ nm, $3-4$ nm, $4-5$ nm, and a region beyond 5 nm from the CNT were calculated. None

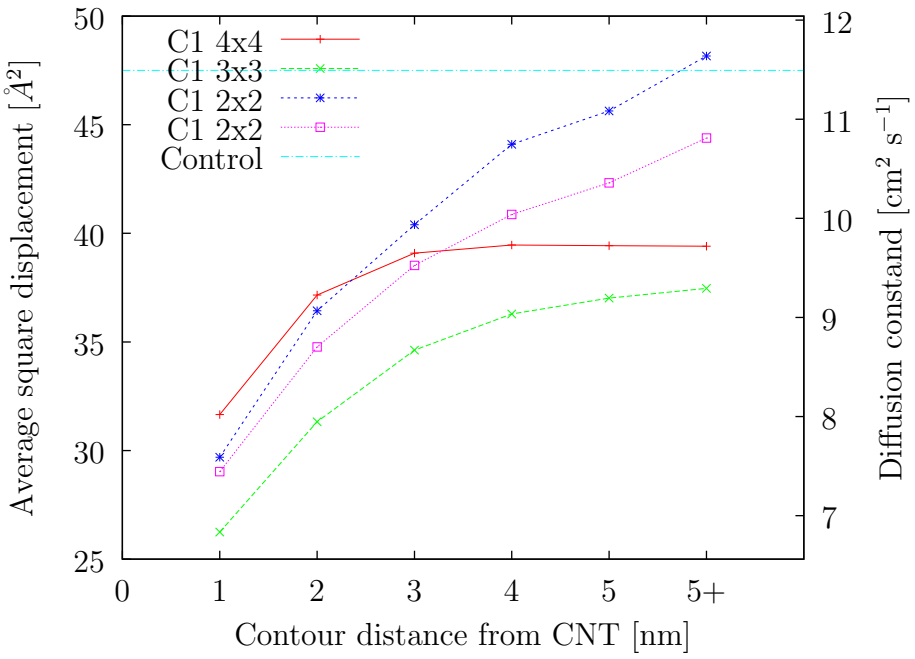


Figure 5.10: Comparison of lipid mean square displacements $\langle r^2 \rangle$ and diffusion coefficients D in various contour distances around the CNT. Observation time 1 ns (see text). Contour distance of 1 nm corresponds to an area $0-1$ nm around the CNT, contour distance of 2 nm corresponds to an area between 1 and 2 nm from the CNT. For crowded membranes, contours are allowed to overlap. '5+' indicates any lipids further than 5 nm away from any particular CNT (this region, for any CNT under consideration, may contain other CNTs). The overall diffusion coefficients are different for different measurements presented, for in more crowded membranes, an average lipid is closer to any CNT, which slows down the diffusion rate. Diffusion coefficient of the control sample (see page 102) plotted for comparison.

of the outer regions included the lipids from the inner regions. Those contour were, however, allowed to overlap, e.g. a $3-4$ nm contour for one CNT may overlap with another contour for another nanotube. The contour labelled '5+' corresponds to lipids further away than 5 nm from a particular nanotube. In the case of multiple nanotubes in the bilayer, this region may still be occupied by another CNT. The purpose was to check if there is an overall slowing down of the lipids in the immediate vicinity of a CNT. As the net effect of CNTs on lipids is to slow down the diffusion, for the more crowded bilayers, the overall diffusion coefficient is lower, as can be seen in fig. 5.10.

Due to the dynamic nature of lipids, the square displacements were calculated in 1 ns

intervals, to keep the lipids as close to the specified regions within a time window as possible. Average square displacement $\langle r^2 \rangle$ for a two-dimensional system is related to the diffusion coefficient D via $\langle r^2 \rangle = 4Dt$, where t is time [283]. As measurements were performed for fixed time windows, $\langle r^2 \rangle$ is a measure of lipid diffusion coefficient D. The results are shown in fig. 5.10. The overall range of values obtained for the diffusion coefficient D ($9 - 12 \times 10^{-7}$ cm^2 s^{-1}) seems to be in agreement with previous studies [285, 286]. In particular, it seems to agree with the results for protein-lipid systems [285]. The results obtained are slightly larger than the mean value in [285]. Given the 1 ns time windows used in this work, it actually is rather reassuring that the diffusion constants obtained are slightly larger, as it has been observed before that for short observation time windows, the diffusion coefficient may appear elevated [287, 286]. The long observation time (1000 ns) diffusion coefficient obtained for a control sample of in a pure (i.e. no CNT or other inclusions) 30×30 nm^2 DPPC lipid patch obtained in this study was 11.4×10^{-7} cm^2 s^{-1}. This is close to the values reported in other studies [285, 288, 286], especially given the range of values of D obtained for lipids in both experiment and simulation [286]. In the $4 - 5$ nm region, the lipids seem to reach mean square displacements similar to that in the region outside the outer border of such defined contours, indicating the mean square displacements approached the 'bulk' values. This is particularly true for the systems with a higher CNT concentration, where fewer regions were far from the CNTs, i.e. more lipids were within ~5 nm, or less, of the CNT for the systems with more nanotube crowding. This is further confirmed by the lower D values obtained for these systems. Interestingly, the extent of this diffusion coefficient reduction is of a similar magnitude as extent of bilayer thickening reported upon the CNT piercing in chapter 3. This relation by no means implies correlation or causation and currently no link between the two values could be established.

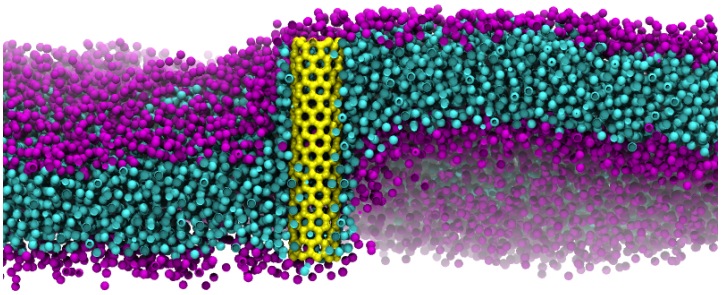
The diffusion coefficient for the CNTs could not be established at this time. This

is mainly because there were insufficient samples to make the diffusion law work (as it relates the diffusion coefficient to the *average* square displacement, and a large number of samples is required for this average to reflect the diffusion law). Accumulating enough statistically significant samples would require many more simulations, which was beyond the computational power and computing time available for this project. It would, however, be a very interesting task to analyse CNT diffusion more closely. As the CNTs do not have a cylindrical cross-section when in plane of the membrane (when viewed from above the bilayer), their diffusion would be expected to be different from that of any other regularly-shaped objects (like proteins or nanoparticles) and a different description might be needed. Additional considerations, such as the cylindrical shape, tilt or tube-tube interactions might have an influence on the CNT diffusion. This would be a very interesting future problem.

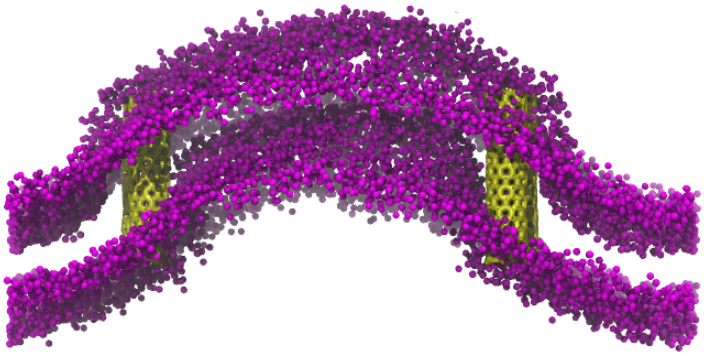
5.2.2 Restrained CNT

To investigate the behaviour of a CNT spanning across the lipid bilayer, a set of simulations was prepared where the CNTs were constrained in the z-direction (perpendicular to the bilayer normal). This way the CNTs were still free to move in the xy plane defined by the bilayer (fig. 5.1). This was done to prevent the rotation of the CNTs observed in the previous section.

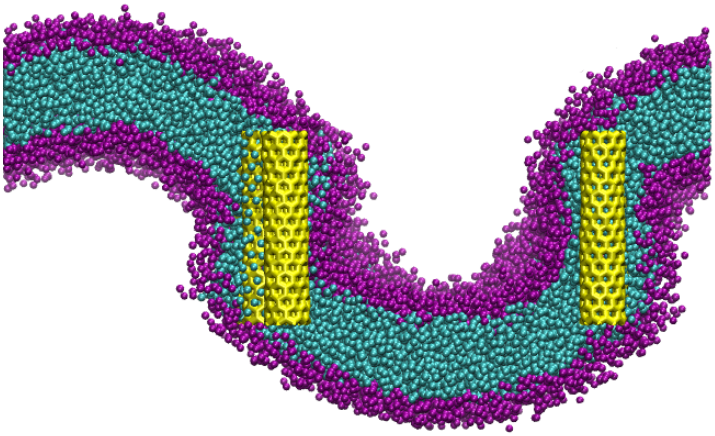
The results were rather surprising. The CNTs did indeed maintain their z-position in the simulation box and did not rotate. Instead of observing a semi-free (due to the z-position restraint), cylinder-like CNT diffusion within the bilayer (which could be thought of as analogous to protein diffusion [279]), what was actually observed was the bilayer adapting its geometry to cover the CNTs (fig. 5.11a). The bilayer no longer remained planar, and formed bud-like structures (fig. 5.11b) and folds (fig. 5.11c). In the previous section, the CNTs rotated within the bilayer to minimise the hydrophobic



(a) Membrane twisting and adaptation



(b) Bud-like structure formation

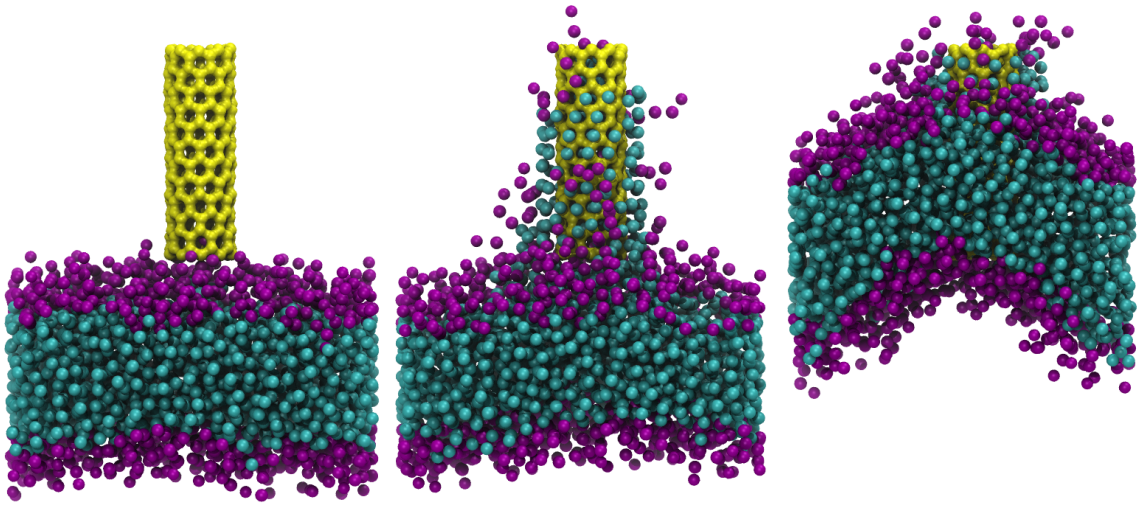


(c) Fold formation

Figure 5.11: Membrane deformation in response to position-restrained CNTs

length mismatch between the CNT and membrane, as discussed. Here, an analogous process seems to take place. However, this time the CNT is not free to rotate, and so it is the bilayer that adapts to cover the CNTs. Interestingly, the protrusions in the bilayer surface are reminiscent of those described in [225], where the presence of the CNTs led to local membrane softening. The authors did not extract any values for bending moduli, due to the limited size of their system. Simulations presented here are of similar lateral size, and also have more complicated geometries, so the extraction of bending moduli was not attempted, for the same reasons as presented in [225].

A batch of simulations was prepared to check how a short (5 nm), restrained CNT placed *just outside* a bilayer would affect the CNT-membrane interaction. In this set, the CNT was initially positioned immediately outside a small DPPC bilayer patch (of size 8×8 nm^2) and it was nearly touching the lipid headgroups (see fig. 5.12a). The CNT was pulled towards the bilayer and fully position restrained ($k = 1000$ kJ mol^{-1} nm^{-2}) just



(a) 0 ns (b) 5.4 ns (c) 52 ns

Figure 5.12: Simulation snapshot. Short (5 nm) position-restrained CNT above an 8×8 nm^2 bilayer patch. CNT position constant in the box and in the images. Simulation times as marked. Initially (b), a lipid creep is observed, just as in chapter 3. Due to CNT position restraints, at later times, the entire bilayer moves up the CNT

after touching the membrane. This setup is similar to what was presented in chapter 3. See fig. 3.1 for a system overview comparison. The main difference here is that the CNT was restrained immediately after making contact with the lipids. After the restraining took place, the lipids would start climbing up the CNT (fig. 5.12b) as before (see chapter 3). However, due to CNT restraints, after the lipids covered the CNT, the membrane would move up the CNT *as a whole*, while the CNT remained fixed in position. An extended meniscus-like shape was formed as the bilayer was translated up the CNT and lifted from its original position (see fig. 5.12c).

While the restraints as described here may not be practically achievable in a real situation, they do point to an important effect, namely that the bilayer may respond to the presence of a CNT under certain conditions, just as a CNT will respond (by rotation) to being in a bilayer. Idealised arrays of CNTs as simulated may not be available experimentally, but it is not difficult to imagine a single CNT being immobilised in the proximity of a bilayer or cell membrane.

This effect is akin to what was postulated earlier. In chapter 3, the lipid creep was attributed to the membrane trying to screen the CNT from the unfavourable interaction with water by coating the CNT in a layer of lipids. For a CNT immobilised in a bilayer, this effect appears to be more drastic. The entire bilayer seems to move, presumably to cover the CNT. Just as in the previous section the CNT seems to rotate in the bilayer to match the hydrophobic length, here the bilayer will 'rotate', or move, to accomplish a similar effect. Significantly, despite such deformation due to the presence of the CNTs, the membrane *does* maintain its integrity and stays continuous and intact throughout the simulations. This seems to be in agreement with previous studies on both carbon nanotubes and fullerenes [218].

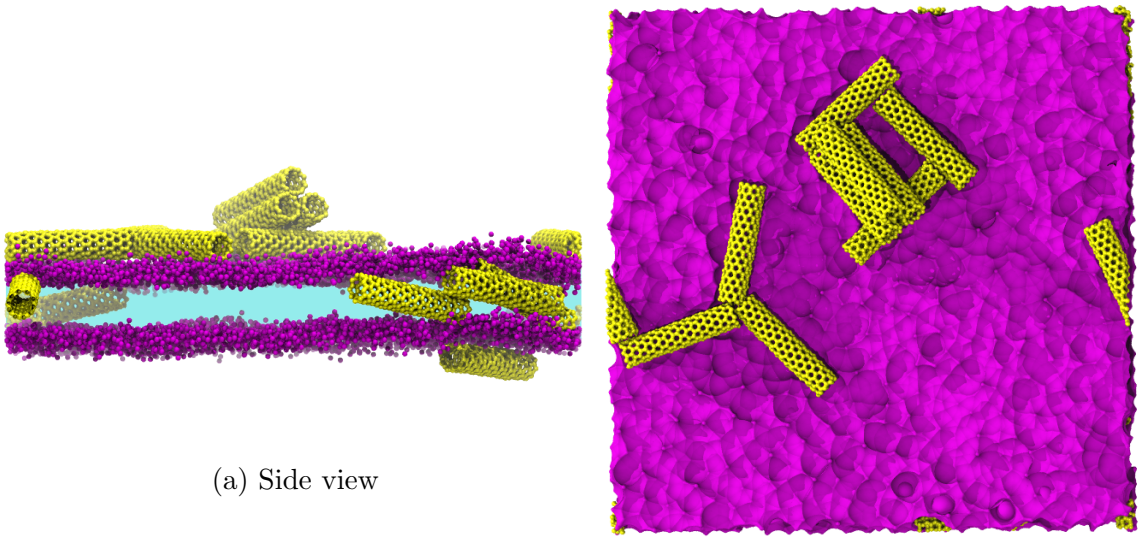
5.2.3 Free CNTs in solution

Finally, simulations were prepared to investigate the behaviour of CNTs 'suspended' in a liquid solution outside of the lipid bilayer. This was done to investigate the potential for cell internalisation and the possible use of CNTs as drug delivery agents. This situation was largely simplified by placing arrays of semi-randomly oriented CNTs above the bilayer (fig. 5.3).

Whereas no uniform behaviour was observed regarding the 'horizontal' and 'vertical' starting arrangements, two regimes across the simulations were noticed. The CNTs would localise in two preferred locations, either within the lipid bilayer, or, surprisingly, at the lipid-water interface *outside* the bilayer (see fig. 5.13). The latter is unexpected, neither from the work done for this thesis so far, nor any previous simulations.

This final location could be attributed to the method or CNT-lipid approach. It has been observed that CNTs approaching the bilayer with their axes pointing in the direction that is largely perpendicular to the bilayer ('vertical', as in section 5.1 and fig. 5.3b) will be internalised, and those approaching the bilayer with their axes closer to parallel to the bilayer plane ('horizontal', as in section 5.1 and fig. 5.3a) will stay outside the membrane and never internalise (fig. 5.14), at least within the timescale of the simulation (2000 ns). The internalisation itself was a rather long process, taking $100 - 200$ ns on average, per nanotube. The angle at which this switch in behaviour occurs could not be determined due to the casual nature of this process. This angle would be expected to be subject to significant variations just as the formation of a meniscus upon CNT piercing (see chapter 3) was expected to be of a stochastic nature.

It was interesting to observe the CNTs bundle together (with their axes parallel), or just come into contact (with their axes crossing) in solution. This is exactly what happens to CNTs in a water-based solution experimentally (see chapter 1.2.2). One of two things could happen to such CNT bundles. If one of the CNTs approached the



(a) Side view

(b) Top view

Figure 5.13: Resulting CNT locations in simulations where the CNTs were placed outside the bilayer and left to interact freely with the surrounding system (i.e. each other and the bilayer). Different views (rotated by 90 degrees) of the same simulation frame shown. For a starting configuration, see fig. 5.3b. Cyan shading in (a) indicates bilayer hydrocarbon tails, to differentiate from the white solvent areas outside.

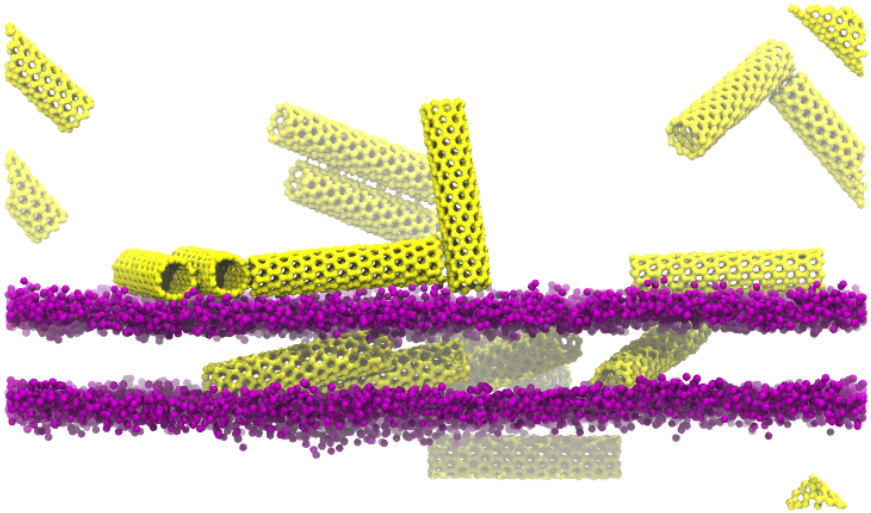


Figure 5.14: Free CNTs from solution approaching the bilayer. The CNTs lying flat on the bilayer will stay there for the duration of the simulations. The CNT perpendicular to the bilayer is about to be internalised in the bilayer.

bilayer in a needle-like manner, it would get internalised and would also facilitate the internalisation of the other CNT in the bundle. If the CNTs stayed on the outside of the bilayer without internalising, the bundle would still be stable (fig. 5.13), and further contacts with other CNTs could be made. In some cases, the CNTs would even stack on the outside of the bilayer (fig. 5.13b). Such stacking could prove to be dangerous to cells. Firstly, bundles of CNTs, apart from blocking access to the membrane, would effectively turn parts of the cell membrane in the vicinity of the CNTs slightly hydrophobic. Possible membrane stiffening could potentially arise from extended CNT networks, an effect similar to that arising from the presence of cytoskeleton [202, 289].

At this time, no clear mechanism for this behaviour could be inferred with a high degree of certainty. Two possible explanations come to the forefront. Firstly, the cost of perturbing a bilayer. It is relatively easier to introduce a small perturbation arising from the small contact area of a needle-like, or 'vertical' approach than from a large contact area arising from a CNT wall-lipid contact in the 'horizontal' approach. This is further confirmed by studies on internalisation of fullerenes [227, 221], which had similar diameters as the CNTs used in this work. Secondly, geometric constraints could play a role. In the needle-like, 'perpendicular' approach, the CNT provides a large area on which the lipids could climb, as described in chapter 3. In the 'horizontal' CNT approach, the lipids that would climb the CNT if it was in the 'vertical' position could be geometrically constrained, or 'blocked' by the CNT wall immediately above them.

5.3 Summary

It has been demonstrated that both CNTs and the lipid bilayer will adapt in response to the presence of the other. The membrane will increase its thickness around the CNT to match the hydrophobic length of the nanotube, and in extreme cases it will

significantly deform. Importantly, even the most radical deformation did not lead to disruption in membrane integrity. The CNTs, when free to move and embedded in the membrane, will tilt to align their axes towards the bilayer core. It appears to be similar to hydrophobic length matching observed for proteins [280, 1]. In fact, the overall behaviour of CNTs in this chapter appears not to be too different from what is observed for proteins. It is known that proteins will tilt slightly [280, 1] in the membrane to match the hydrophobic length of the membrane hydrocarbon core. Some extent of thickening (and thinning) has been observed around proteins whose hydrophobic length does not match the hydrophobic thickness of the bilayer core [2]. Similarly, membrane proteins do not usually spontaneously insert into membranes. Such insertion needs to be facilitated. In the current simulations, only some of the CNTs were inserted into the bilayer, while others stayed outside of the membrane. Of course, the CNTs presented here, compared to a typical protein, were fully hydrophobic end-to-end, which could make any insertion into the membrane easier.

Based on the data presented in this chapter, it cannot be inferred that CNTs behave exactly like proteins. Such a conclusion would not be reasonable, due to completely different structural properties of each. There are, however, some similarities, and maybe a slightly different view should be assumed when looking at the CNT-lipid interaction, at least for small CNTs. This would not be unreasonable: given the wealth of data available for proteins and membranes, it might be possible to hypothesise new behaviour based on the existing knowledge.

Finally, the simulations with free CNTs in solution suggest that CNTs may not internalise as easily as could be imagined, and hydrophobicity is not enough for bilayer penetration [290]. While their hydrophobic nature does play a significant role once the membrane structure has been perturbed (e.g. by piercing), they may not penetrate the bilayer as readily. This appears to be in contrast to fullerene penetration [227, 221],

where all hydrophobic particles would internalise upon contact. This is most likely related to the size of the particles in question. Fullerenes, being much smaller, can perturb the lipid bilayer more easily. This is reminiscent of the CNT approach described in this chapter, where a perpendicular CNT could perturb a small area more easily than a parallel one.

6 Conclusions

The work presented in this thesis focused on the use of MD simulations and AFM microscopy to study the interactions between the CNTs and lipid bilayers. What is meant by 'interactions' in this context should be understood as a response to a stimulus or a reaction of the membrane to the presence of a nanotube. While this may involve energetic response to the presence of foreign chemical moieties, the focus here was on mechanical properties and physical phenomena, such as deformation, indentation or rupture. The main objective was to look at the processes occurring at the point of CNT-lipid contact at the molecular level, to better understand the behaviour of the system and the mechanical response as the basis of the interaction. The experiments and simulations were designed to complement each other, and the results from each influenced further progression of the other. MD simulations, backed by experimental data, revealed a number of new effects.

6.1 Summary

A number of phenomena were observed upon contact between the lipid bilayer and a CNT pulled towards it. The bilayer would adapt a meniscus-like shape on CNT piercing the lipid headgroups, which would be followed by a creep of lipids up the CNT walls (see chapter 3.2.1). This is reminiscent of what was observed experimentally in [291]. Here, this creep was associated with the hydrophobicity of the CNT, or at least hydrophobic

compatibility of the CNT and the lipid tails, as the exact hydrophobic particle type (and CNT hydrophobic character) was not as important, as long as it was kept relatively close to that of the lipid tails (see chapter 3.2.3). The lipids were thought to coat the CNT to screen it, at least partially, from the unfavourable interactions with water. Importantly, this was observed for all lipid species examined, suggesting it is a universal effect. This creep was also associated with the slow CNT pulling towards the bilayer, which suggests that the timescale of CNT-membrane related phenomena is longer than expected. It seems further confirmed by the CNT internalisation times reported in chapter 5.2.3. This is particularly relevant for the choice of simulation lengths, as many authors would focus on shorter timescales, which, while computationally convenient, may lead to some effects being glossed over, as evidenced by no prior reporting or detailed description of the lipid creep in simulations, as illustrated in this work.

The lipid creep disappeared for the less hydrophobic particle types. For the most hydrophilic CNT-like molecule, the interaction was drastically different - not only did the lipid creep disappear but the membrane would form a depression when the CNT was pulled towards it. For the most hydrophilic particle types, this depression and membrane deformation was quite drastic (see chapter 3.2.3). The varying CNT particle types used in this work were used to assess the sensitivity of the observed effects to parametrisation. They also averaged over the effects of CNT functionalisation that is typically employed experimentally (see chapter 1.2.2 and 3.2.3). In light of this, it appears that CNTs with different hydrophobicity, or levels of functionalisation, will interact with the membrane in different ways. This is important as it shows that a more careful and systematic experimental approach should be used when talking about CNT-membrane interaction. This may also explain why different CNT uptake mechanisms have been suggested experimentally [121].

The meniscus formation was observed to be triggered by a random event, which in-

duced cooperative transition (see chapter 3.2.1). It may suggest that the affinity between the CNT and lipids is not the default behaviour and should not be taken for granted.

Another effect that seemed to be conserved across the simulations was the thickening of the bilayer around the nanotube when the CNT was located within and perpendicular to the membrane. In chapter 5.2.1 it was attributed to hydrophobic length matching between the bilayer and the CNT. This could also be a likely explanation of the thickening observed in chapter 3.2.1, with lipids being able to only match a part of the length of the CNT, but via a similar mechanism.

The mechanical properties of the CNT-lipid interaction reported here (see chapter 4) are very important. The proof-of-concept lipid indentations with a conventional AFM probe gave rise to 'classic' results that could be well described with the known mechanical indentation models (see chapter 4.2.1).

The mechanical indentation of lipids with a CNT probe (see chapter 4.2.1) did show a different behaviour. The observed response could not be described in terms of the usual, conventional models and no compelling reasons for the observed discrepancy could be justified. This suggests that a different mechanism governs the mechanical response of the lipids interacting with a CNT.

To understand the observed experimental results, a set of MD simulations was prepared (see chapter 4.2.2). The simulations agree, if at least qualitatively, with the AFM results (see chapter 4.3). They seem to capture the essential features of the experimental force curves. This suggests that the coarse grained methodology used in the simulations provides sufficient detail to describe the system accurately, while being computationally effective. Given the different timescales and pulling speeds used in the experiments (see chapter 4.1.1) and simulations (see chapter 4.1.2) presented here, this agreement seems quite remarkable, despite a few minor differences.

Overall, comparing the simulation results with the experimental data suggests that

the CG simulations are a good model of the real interaction, which justifies their further use to describe the CNT-lipid interaction.

Once internalised (in chapter 5, this was done via a deliberate placement of CNTs in a lipid bilayer), the CNTs will slow down the lipid diffusion around them (see chapter 5.2.1). This is similar to what was observed for proteins and is most likely the result of the reduction of the 2D space that the lipids can explore.

Placing short CNTs in a pre-equilibrated bilayer resulted in bilayer thickening described before. However, the CNTs also rotated towards the centre of the bilayer (see chapter 5.2.1), a process that is readily observed for proteins. It also minimised the exposure of the CNTs to water, which was one of the reasons given for the lipid creep observed in chapter 3.2.1. This lipid creep and thickening was not the only way the lipid bilayer would respond to the presence of a CNT. More drastic changes and bilayer deformations were observed for the case of nanotubes restrained in the membrane (see chapter 5.2.2). Together, these show that the membrane will adapt its shape and conformation to the presence of a CNT. However, as the CNT rotation and diffusion shows, the short CNTs will also be influenced by the lipid bilayer, suggesting such adaptation is mutual.

When placed in solution outside the membrane, the CNTs showed that their internalisation within the lipid bilayer was not an obvious and straightforward process. Nor was the internalisation universal. It was subject to the overall approach angle that the CNT made with the bilayer, with the nanotubes approaching in the nearly perpendicular direction (via a 'nano-needle' mechanism) being internalised, and the CNTs approaching largely parallel to the bilayer staying on the *outside* bilayer surface, facing the solvent. This shows that the CNT internalisation is not a universal process and will not happen in all cases, despite the high CNT-membrane affinity observed *in vitro*. This should be taken into account when designing future experiments and interpreting their results.

6.2 Future work

The work in this thesis focused on basic interactions between simplified lipid bilayers and single walled carbon nanotubes. The immediate future work should concentrate on increasing the complexity of the systems studied. A few suggested extensions of this work are summarised below:

- Firstly, the interaction between CNTs and membrane embedded proteins should be investigated. Real membranes contain a large collection of proteins [2]. It has also been reported that CNTs show an affinity to certain peptides and proteins [107, 106]. It would be very interesting to see how that potential interaction would influence the behaviour of either the proteins or the nanotubes. This could initially be studied using simple peptides, comparable in size to the SWNTs used, before moving on to larger proteins.

- To further investigate membrane complexity, lipid mixtures, with more diverse lipids, including cholesterol, should be studied. This would show whether the CNTs have particular affinity to any specific lipids. Their location within such rich bilayer mixes could also be looked at. Experimentally, CNT interaction with different lipid phases needs to be addressed.

- More attention should be focused on multi-walled nanotubes. This would test the interaction of larger CNTs with the bilayer. As the typical CNTs tend to be bulkier and multi-walled, this would shed some light onto the behaviour of such systems. Also, the MWNTs used as nano-needles in steered molecular dynamics simulations would contact the bilayer with a larger area, having larger cross sections. This would exert a different pressure profile on the membrane, which could lead to new effects.

- Ideally, atomistic simulations of the CNT-bilayer system should be carried out.

This would further test the applicability of CG force fields to the description of the interaction. This, however, demands more computing power, due to the fairly large spatial and temporal scale required. It may be possible to achieve this with the newer supercomputers.

- Simulations with less structurally idealised CNTs should be carried out. This may involve structural defects, as well as side-wall functionalisation with larger molecules projecting away from the surface. Such derivatisation would bring this work even closer to the CNTs employed in experiments. Atomistic simulations could be used to parametrise such inclusions.

- Regarding the use of the AFM to research this interaction, a further set of experiments could focus on imaging mixes of lipid bilayers prepared in the presence of CNTs. This could reveal the mechanisms of CNT internalisation, e.g. the location of CNTs after dispersing a CNT-containing imaging buffer over the prepared bilayers.

- The effects of a SWNT acting on a lipid membrane should be investigated experimentally. This would involve preparation of a SWNT AFM probe. There are some technical challenges related to this (such as the small size of single-walled CNTs, or difficulties in straightening a single-shell CNT), but such experiments would definitely be beneficial.

- An interesting cross check on the experimental results could come about from using a probe with a rod-like tip made of amorphous carbon. This could be easily achieved by growing such a carbon spike on the AFM tip using electron beam-induced deposition (EBID). Such a probe could be used to see how a long rod of unstructured carbon (as opposed to the structured CNT) would interact with the lipid membrane.

- The CNT-lipid interaction should be investigated under the environmental scanning electron microscope. This has the advantages of a typical SEM, but the experiments can be carried out in a gaseous and humid atmosphere, allowing the observation of wet systems, which is relevant for lipid membranes. A controlled interaction with a CNT as an indenting probe could be looked at, helping visualise the processes occurring on contact at the nanoscale.

Overall, the further study of the CNT-lipid interactions would benefit from further MD simulations. There is a wealth of experimental and toxicology data on CNT-cell interaction at the macroscale but the molecular description of the process needs more focus and refinement. It is hoped that this study will stimulate further investigations in this field.

Bibliography

[1] M. Luckey, *Membrane Structural Biology: With Biochemical and Biophysical Foundations*. Cambridge University Press, 2008.

[2] B. Alberts, *Molecular Biology of the Cell: Reference edition*. Garland Science, 2008.

[3] T. Weiss, *Cellular Biophysics: Transport*, vol. 1. A Bradford Book, 1996.

[4] A. Finkelstein, *Water movement through lipid bilayers, pores, and plasma membranes: theory and reality*. Wiley, 1987.

[5] J. V. Møller, C. Olesen, A. M. L. Winther, and P. Nissen, "The sarcoplasmic Ca2+-ATPase: Design of a perfect chemi-osmotic pump," *Quarterly Reviews of Biophysics*, vol. 43, no. 4, pp. 501–566, 2010.

[6] J. P. Morth, B. P. Pedersen, M. J. Buch-Pedersen, J. P. Andersen, B. Vilsen, M. G. Palmgren, and P. Nissen, "A structural overview of the plasma membrane Na+,K+-ATPase and H+-ATPase ion pumps," *Nature Reviews Molecular Cell Biology*, vol. 12, no. 1, pp. 60–70, 2011.

[7] A. G. Therien and R. Blostein, "Mechanisms of sodium pump regulation," *American Journal of Physiology - Cell Physiology*, vol. 279, no. 3 48-3, pp. C541–C566, 2000.

[8] T. Zeuthen, "Water-transporting proteins," *Journal of Membrane Biology*, vol. 234, no. 2, pp. 57–73, 2010.

[9] D. Voet and J. Voet, *Biochemistry*. John Wiley & Sons, 2011.

[10] E. Fahy, S. Subramaniam, H. A. Brown, C. K. Glass, A. H. Merrill Jr., R. C. Murphy, C. R. H. Raetz, D. W. Russell, Y. Seyama, W. Shaw, T. Shimizu, F. Spener, G. Van Meer, M. S. VanNieuwenhze, S. H. White, J. L. Witztum, and E. A. Dennis, "A comprehensive classification system for lipids," *Journal of Lipid Research*, vol. 46, no. 5, pp. 839–861, 2005.

[11] G. Van Meer, "Cellular lipidomics," *EMBO Journal*, vol. 24, no. 18, pp. 3159–3165, 2005.

[12] A. Shevchenko and K. Simons, "Lipidomics: Coming to grips with lipid diversity," *Nature Reviews Molecular Cell Biology*, vol. 11, no. 8, pp. 593–598, 2010.

[13] G. Van Meer, D. R. Voelker, and G. W. Feigenson, "Membrane lipids: Where they are and how they behave," *Nature Reviews Molecular Cell Biology*, vol. 9, no. 2, pp. 112–124, 2008.

[14] U. Coskun and K. Simons, "Cell membranes: The lipid perspective," *Structure*, vol. 19, no. 11, pp. 1543–1548, 2011.

[15] N. Kučerka, S. Tristram-Nagle, and J. F. Nagle, "Closer look at structure of fully hydrated fluid phase DPPC bilayers," *Biophysical Journal*, vol. 90, no. 11, pp. L83–L85, 2006.

[16] J. N. Israelachvili, *Intermolecular and surface forces*. Academic Press, 3rd ed., 2011.

[17] D. Marsh, "Lateral pressure profile, spontaneous curvature frustration, and the incorporation and conformation of proteins in membranes," *Biophysical Journal*, vol. 93, no. 11, pp. 3884–3899, 2007.

[18] S. Iijima, "Helical microtubules of graphitic carbon," *Nature*, vol. 354, no. 6348, pp. 56–58, 1991.

[19] M. Monthioux and V. L. Kuznetsov, "Who should be given the credit for the discovery of carbon nanotubes?," *Carbon*, vol. 44, pp. 1621–1623, 8 2006.

[20] R. C. Haddon, "Carbon nanotubes," *Accounts of Chemical Research*, vol. 35, no. 12, p. 997, 2002.

[21] H. W. Kroto, J. R. Heath, S. C. O'Brien, R. F. Curl, and R. E. Smalley, "C60: Buckminsterfullerene," *Nature*, vol. 318, no. 6042, pp. 162–163, 1985.

[22] M. S. Dresselhaus, G. Dresselhaus, and R. Saito, "Carbon fibers based on C60 and their symmetry," *Physical Review B*, vol. 45, no. 11, pp. 6234–6242, 1992.

[23] X. Wang, Q. Li, J. Xie, Z. Jin, J. Wang, Y. Li, K. Jiang, and S. Fan, "Fabrication of ultralong and electrically uniform single-walled carbon nanotubes on clean substrates," *Nano Letters*, vol. 9, no. 9, pp. 3137–3141, 2009.

[24] K. Anazawa, K. Shimotani, C. Manabe, H. Watanabe, and M. Shimizu, "High-purity carbon nanotubes synthesis method by an arc discharging in magnetic field," *Applied Physics Letters*, vol. 81, no. 4, pp. 739–741, 2002.

[25] T. W. Ebbesen and P. M. Ajayan, "Large-scale synthesis of carbon nanotubes," *Nature*, vol. 358, no. 6383, pp. 220–222, 1992.

[26] T. Yamaguchi, S. Bandow, and S. Iijima, "Synthesis of carbon nanohorn particles by simple pulsed arc discharge ignited between pre-heated carbon rods," *Chemical Physics Letters*, vol. 389, no. 1-3, pp. 181–185, 2004.

[27] T. Guo, P. Nikolaev, A. Thess, D. T. Colbert, and R. E. Smalley, "Catalytic growth of single-walled manotubes by laser vaporization," *Chemical Physics Letters*, vol. 243, no. 1-2, pp. 49–54, 1995.

[28] W. K. Maser, E. Muñoz, A. M. Benito, M. T. Martínez, G. F. De La Fuente, Y. Maniette, E. Anglaret, and J. L. Sauvajol, "Production of high-density single-walled nanotube material by a simple laser-ablation method," *Chemical Physics Letters*, vol. 292, no. 4-6, pp. 587–593, 1998.

[29] A. Thess, R. Lee, P. Nikolaev, H. Dai, P. Petit, J. Robert, C. Xu, Y. H. Lee, S. G. Kim, A. G. Rinzler, D. T. Colbert, G. E. Scuseria, D. Tománek, J. E. Fischer, and R. E. Smalley, "Crystalline ropes of metallic carbon nanotubes," *Science*, vol. 273, no. 5274, pp. 483–487, 1996.

[30] C. D. Scott, S. Arepalli, P. Nikolaev, and R. E. Smalley, "Growth mechanisms for single-wall carbon nanotubes in a laser-ablation process," *Applied Physics A: Materials Science and Processing*, vol. 72, no. 5, pp. 573–580, 2001.

[31] R. Alexandrescu, A. Crunteanu, R. E. Morjan, I. Morjan, F. Rohmund, L. K. L. Falk, G. Ledoux, and F. Huisken, "Synthesis of carbon nanotubes by CO2-laser-assisted chemical vapour deposition," *Infrared Physics and Technology*, vol. 44, no. 1, pp. 43–50, 2003.

[32] C. J. Lee, S. C. Lyu, H. W. Kim, C. Y. Park, and C. W. Yang, "Large-scale production of aligned carbon nanotubes by the vapor phase growth method," *Chemical Physics Letters*, vol. 359, no. 1-2, pp. 109–114, 2002.

[33] P. Nikolaev, M. J. Bronikowski, R. K. Bradley, F. Rohmund, D. T. Colbert, K. A. Smith, and R. E. Smalley, "Gas-phase catalytic growth of single-walled carbon nanotubes from carbon monoxide," *Chemical Physics Letters*, vol. 313, no. 1-2, pp. 91–97, 1999.

[34] P. Nikolaev, "Gas-phase production of single-walled carbon nanotubes from carbon monoxide: A review of the HiPco process," *Journal of Nanoscience and Nanotechnology*, vol. 4, no. 4, pp. 307–316, 2004.

[35] J. B. Park, G. S. Choi, Y. S. Cho, S. Y. Hong, D. Kim, S. Y. Choi, J. H. Lee, and K. I. Cho, "Characterization of Fe-catalyzed carbon nanotubes grown by thermal chemical vapor deposition," *Journal of Crystal Growth*, vol. 244, no. 2, pp. 211–217, 2002.

[36] S. W. Kim, T. Kim, Y. S. Kim, H. S. Choi, H. J. Lim, S. J. Yang, and C. R. Park, "Surface modifications for the effective dispersion of carbon nanotubes in solvents and polymers," *Carbon*, vol. 50, no. 1, pp. 3–33, 2012.

[37] R. M. Stevens, C. V. Nguyen, and M. Meyyappan, "Carbon nanotube scanning probe for imaging in aqueous environment," *IEEE Transactions on Nanobioscience*, vol. 3, no. 1, pp. 56–60, 2004.

[38] L. Lacerda, A. Bianco, M. Prato, and K. Kostarelos, "Carbon nanotubes as nanomedicines: From toxicology to pharmacology," *Advanced Drug Delivery Reviews*, vol. 58, no. 14, pp. 1460–1470, 2006.

[39] J. H. Walther, R. Jaffe, T. Halicioglu, and P. Koumoutsakos, "Carbon nanotubes in water: Structural characteristics and energetics," *The Journal of Physical Chemistry B*, vol. 105, no. 41, pp. 9980–9987, 2001.

[40] T. W. Ebbesen, P. M. Ajayan, H. Hiura, and K. Tanigaki, "Purification of nanotubes [6]," *Nature*, vol. 367, no. 6463, p. 519, 1994.

[41] Y. S. Park, Y. C. Choi, K. S. Kim, D. C. Chung, D. J. Bae, K. H. An, S. C. Lim, X. Y. Zhu, and Y. H. Lee, "High yield purification of multiwalled carbon nanotubes by selective oxidation during thermal annealing," *Carbon*, vol. 39, no. 5, pp. 655–661, 2001.

[42] J. L. Zimmerman, R. K. Bradley, C. B. Huffman, R. H. Hauge, and J. L. Margrave, "Gas-phase purification of single-wall carbon nanotubes," *Chemistry of Materials*, vol. 12, no. 5, pp. 1361–1366, 2000.

[43] Y. Li, X. Zhang, J. Luo, W. Huang, J. Cheng, Z. Luo, T. Li, F. Liu, G. Xu, X. Ke, L. Lin, and H. J. Geise, "Purification of CVD synthesized single-wall carbon nanotubes by different acid oxidation treatments," *Nanotechnology*, vol. 15, no. 11, pp. 1645–1649, 2004.

[44] E. Dujardin, T. W. Ebbesen, A. Krishnan, and M. M. J. Treacy, "Purification of single-shell nanotubes," *Advanced Materials*, vol. 10, no. 8, pp. 611–613, 1998.

[45] K. Hernadi, A. Siska, L. Thiên-Nga, L. Forró, and I. Kiricsi, "Reactivity of different kinds of carbon during oxidative purification of catalytically prepared carbon nanotubes," *Solid State Ionics*, vol. 141-142, pp. 203–209, 2001.

[46] H. Hu, B. Zhao, M. E. Itkis, and R. C. Haddon, "Nitric acid purification of single-walled carbon nanotubes," *Journal of Physical Chemistry B*, vol. 107, no. 50, pp. 13838–13842, 2003.

[47] T. Suzuki, K. Suhama, X. Zhao, S. Inoue, N. Nishikawa, and Y. Ando, "Purification of single-wall carbon nanotubes produced by arc plasma jet method," *Diamond and Related Materials*, vol. 16, no. 4-7 SPEC. ISS., pp. 1116–1120, 2007.

[48] J. Zhang, H. Zou, Q. Qing, Y. Yang, Q. Li, Z. Liu, X. Guo, and Z. Du, "Effect of chemical oxidation on the structure of single-walled carbon nanotubes," *Journal of Physical Chemistry B*, vol. 107, no. 16, pp. 3712–3718, 2003.

[49] H. Hu, A. Yu, E. Kim, B. Zhao, M. E. Itkis, E. Bekyarova, and R. C. Haddon, "Influence of the zeta potential on the dispersability and purification of single-walled carbon nanotubes," *Journal of Physical Chemistry B*, vol. 109, no. 23, pp. 11520–11524, 2005.

[50] A. Yu, E. Bekyarova, M. E. Itkis, D. Fakhrutdinov, R. Webster, and R. C. Haddon, "Application of centrifugation to the large-scale purification of electric arc-produced single-walled carbon nanotubes," *Journal of the American Chemical Society*, vol. 128, no. 30, pp. 9902–9908, 2006.

[51] R. Andrews, D. Jacques, D. Qian, and E. C. Dickey, "Purification and structural annealing of multiwalled carbon nanotubes at graphitization temperatures," *Carbon*, vol. 39, no. 11, pp. 1681–1687, 2001.

[52] W. Huang, Y. Wang, G. Luo, and F. Wei, "99.9% purity multi-walled carbon nanotubes by vacuum high-temperature annealing," *Carbon*, vol. 41, no. 13, pp. 2585–2590, 2003.

[53] Y. Wang, J. Wu, and F. Wei, "A treatment method to give separated multi-walled carbon nanotubes with high purity, high crystallization and a large aspect ratio," *Carbon*, vol. 41, no. 15, pp. 2939–2948, 2003.

[54] S. Bandow, A. M. Rao, K. A. Williams, A. Thess, R. E. Smalley, and P. C. Eklund, "Purification of single-wall carbon nanotubes by microfiltration," *Journal of Physical Chemistry B*, vol. 101, no. 44, pp. 8839–8842, 1997.

[55] K. B. Shelimov, R. O. Esenaliev, A. G. Rinzler, C. B. Huffman, and R. E. Smalley, "Purification of single-wall carbon nanotubes by ultrasonically assisted filtration," *Chemical Physics Letters*, vol. 282, no. 5-6, pp. 429–434, 1998.

[56] J. L. Bahr and J. M. Tour, "Covalent chemistry of single-wall carbon nanotubes," *Journal of Materials Chemistry*, vol. 12, no. 7, pp. 1952–1958, 2002.

[57] A. Hirsch, "Functionalization of single-walled carbon nanotubes," *Angewandte Chemie - International Edition*, vol. 41, no. 11, pp. 1853–1859, 2002.

[58] M. Holzinger, O. Vostrowsky, A. Hirsch, F. Hennrich, M. Kappes, R. Weiss, and F. Jellen, "Sidewall functionalization of carbon nanotubes," *Angewandte Chemie - International Edition*, vol. 40, no. 21, pp. 4002–4005, 2001.

[59] S. Niyogi, M. A. Hamon, H. Hu, B. Zhao, P. Bhowmik, R. Sen, M. E. Itkis, and R. C. Haddon, "Chemistry of single-walled carbon nanotubes," *Accounts of Chemical Research*, vol. 35, no. 12, pp. 1105–1113, 2002.

[60] R. Saito, G. Dresselhaus, and M. Dresselhaus, *Physical Properties of Carbon Nanotube*. Imperial College Press, 1998.

[61] X. Lu and Z. Chen, "Curved Pi-conjugation, aromaticity, and the related chemistry of small fullerenes (<C60) and single-walled carbon nanotubes," *Chemical Reviews*, vol. 105, no. 10, pp. 3643–3696, 2005.

[62] M. Bockrath, D. H. Cobden, P. L. McEuen, N. G. Chopra, A. Zettl, A. Thess, and R. E. Smalley, "Single-electron transport in ropes of carbon nanotubes," *Science*, vol. 275, no. 5308, pp. 1922–1925, 1997.

[63] J. C. Charlier, X. Blase, and S. Roche, "Electronic and transport properties of nanotubes," *Reviews of Modern Physics*, vol. 79, no. 2, pp. 677–732, 2007.

[64] H. Dai, E. W. Wong, and C. M. Lieber, "Probing electrical transport in nanomaterials: Conductivity of individual carbon nanotubes," *Science*, vol. 272, no. 5261, pp. 523–526, 1996.

[65] T. W. Ebbesen, H. J. Lezec, H. Hiura, J. W. Bennett, H. F. Ghaemi, and T. Thio, "Electrical conductivity of individual carbon nanotubes," *Nature*, vol. 382, no. 6586, pp. 54–56, 1996.

[66] S. Hong and S. Myung, "Nanotube electronics: A flexible approach to mobility," *Nature Nanotechnology*, vol. 2, no. 4, pp. 207–208, 2007.

[67] J. Hone, M. Whitney, C. Piskoti, and A. Zettl, "Thermal conductivity of single-walled carbon nanotubes," *Physical Review B - Condensed Matter and Materials Physics*, vol. 59, no. 4, pp. R2514–R2516, 1999.

[68] P. Kim, L. Shi, A. Majumdar, and P. L. McEuen, "Thermal transport measurements of individual multiwalled nanotubes," *Physical Review Letters*, vol. 87, no. 21, pp. 2155021–2155024, 2001.

[69] E. Pop, D. Mann, Q. Wang, K. Goodson, and H. Dai, "Thermal conductance of an individual single-wall carbon nanotube above room temperature," *Nano Letters*, vol. 6, no. 1, pp. 96–100, 2006.

[70] S. Sinha, S. Barjami, G. Iannacchione, A. Schwab, and G. Muench, "Off-axis thermal properties of carbon nanotube films," *Journal of Nanoparticle Research*, vol. 7, no. 6, pp. 651–657, 2005.

[71] A. Krishnan, E. Dujardin, T. W. Ebbesen, P. N. Yianilos, and M. M. J. Treacy, "Young's modulus of single-walled nanotubes," *Physical Review B - Condensed Matter and Materials Physics*, vol. 58, no. 20, pp. 14013–14019, 1998.

[72] J. P. Lu, "Elastic properties of carbon nanotubes and nanoropes," *Physical Review Letters*, vol. 79, no. 7, pp. 1297–1300, 1997.

[73] M. M. J. Treacy, T. W. Ebbesen, and J. M. Gibson, "Exceptionally high Young's modulus observed for individual carbon nanotubes," *Nature*, vol. 381, no. 6584, pp. 678–680, 1996.

[74] E. W. Wong, P. E. Sheehan, and C. M. Lieber, "Nanobeam mechanics: Elasticity, strength, and toughness of nanorods and nanotubes," *Science*, vol. 277, no. 5334, pp. 1971–1975, 1997.

[75] M. F. Yu, O. Lourie, M. J. Dyer, K. Moloni, T. F. Kelly, and R. S. Ruoff, "Strength and breaking mechanism of multiwalled carbon nanotubes under tensile load," *Science*, vol. 287, no. 5453, pp. 637–640, 2000.

[76] C. M. Wang, Y. Y. Zhang, Y. Xiang, and J. N. Reddy, "Recent studies on buckling of carbon nanotubes," *Applied Mechanics Reviews*, vol. 63, no. 3, pp. 1–18, 2010.

[77] M. F. L. De Volder, S. H. Tawfick, R. H. Baughman, and A. J. Hart, "Carbon nanotubes: Present and future commercial applications," *Science*, vol. 339, no. 6119, pp. 535–539, 2013.

[78] "Zyvex Marine components." http://www.zyvexmarine.com/components/, September 2013.

[79] G. Dennler, M. C. Scharber, and C. J. Brabec, "Polymer-fullerene bulk-heterojunction solar cells," *Advanced Materials*, vol. 21, no. 13, pp. 1323–1338, 2009.

[80] R. M. Stevens, "New carbon nanotube AFM probe technology," *Materials Today*, vol. 12, no. 10, pp. 42–45, 2009.

[81] T.-W. Chou, L. Gao, E. T. Thostenson, Z. Zhang, and J.-H. Byun, "An assessment of the science and technology of carbon nanotube-based fibers and composites," *Composites Science and Technology*, vol. 70, pp. 1–19, 1 2010.

[82] A. Beigbeder, P. Degee, S. L. Conlan, R. J. Mutton, A. S. Clare, M. E. Pettitt, M. E. Callow, J. A. Callow, and P. Dubois, "Preparation and characterisation of silicone-based coatings filled with carbon nanotubes and natural sepiolite and their application as marine fouling-release coatings," *Biofouling*, vol. 24, no. 4, pp. 291–302, 2008.

[83] J. N. Coleman, U. Khan, W. J. Blau, and Y. K. Gun'ko, "Small but strong: A review of the mechanical properties of carbon nanotube-polymer composites," *Carbon*, vol. 44, no. 9, pp. 1624–1652, 2006.

[84] Z. Wu, Z. Chen, X. Du, J. M. Logan, J. Sippel, M. Nikolou, K. Kamaras, J. R. Reynolds, D. B. Tanner, A. F. Hebard, and A. G. Rinzler, "Transparent, conductive carbon nanotube films," *Science*, vol. 305, no. 5688, pp. 1273–1276, 2004.

[85] L. Dai, D. W. Chang, J. B. Baek, and W. Lu, "Carbon nanomaterials for advanced energy conversion and storage," *Small*, vol. 8, no. 8, pp. 1130–1166, 2012.

[86] B. Corry, "Designing carbon nanotube membranes for efficient water desalination," *Journal of Physical Chemistry B*, vol. 112, no. 5, pp. 1427–1434, 2008.

[87] M. Motta, A. Moisala, I. A. Kinloch, and A. H. Windle, "High performance fibres from 'dog bone' carbon nanotubes," *Advanced Materials*, vol. 19, no. 21, pp. 3721–3726, 2007.

[88] "Q-Flo." http://www.q-flo.com/, September 2013.

[89] K. Jensen, J. Weldon, H. Garcia, and A. Zettl, "Nanotube radio," *Nano Letters*, vol. 7, no. 11, pp. 3508–3511, 2007.

[90] A. D. Franklin, M. Luisier, S. J. Han, G. Tulevski, C. M. Breslin, L. Gignac, M. S. Lundstrom, and W. Haensch, "Sub-10 nm carbon nanotube transistor," *Nano Letters*, vol. 12, no. 2, pp. 758–762, 2012.

[91] T. Rueckes, K. Kim, E. Joselevich, G. Y. Tseng, C. L. Cheung, and C. M. Lieber, "Carbon nanotube-based nonvolatile random access memory for molecular computing," *Science*, vol. 289, no. 5476, pp. 94–97, 2000.

[92] N. W. S. Kam and H. Dai, "Carbon nanotubes as intracellular protein transporters: Generality and biological functionality," *Journal of the American Chemical Society*, vol. 127, no. 16, pp. 6021–6026, 2005.

[93] A. Star, E. Tu, J. Niemann, J. C. P. Gabriel, C. S. Joiner, and C. Valcke, "Label-free detection of DNA hybridization using carbon nanotube network field-effect transistors," *Proceedings of the National Academy of Sciences of the United States of America*, vol. 103, no. 4, pp. 921–926, 2006.

[94] E. S. Snow, F. K. Perkins, E. J. Houser, S. C. Badescu, and T. L. Reinecke, "Chemical detection with a single-walled carbon nanotube capacitor," *Science*, vol. 307, no. 5717, pp. 1942–1945, 2005.

[95] B. Edwards and E. Westling, *The Space Elevator*. Bc Edwards, 2003.

[96] S. Banerjee, T. Hemraj-Benny, and S. S. Wong, "Covalent surface chemistry of single-walled carbon nanotubes," *Advanced Materials*, vol. 17, no. 1, pp. 17–29, 2005.

[97] V. Georgakilas, K. Kordatos, M. Prato, D. M. Guldi, M. Holzinger, and A. Hirsch, "Organic functionalization of carbon nanotubes," *Journal of the American Chemical Society*, vol. 124, no. 5, pp. 760–761, 2002.

[98] N. Karousis, N. Tagmatarchis, and D. Tasis, "Current progress on the chemical modification of carbon nanotubes," *Chemical Reviews*, vol. 110, no. 9, pp. 5366–5397, 2010.

[99] R. J. Chen, Y. Zhang, D. Wang, and H. Dai, "Noncovalent sidewall functionalization of single-walled carbon nanotubes for protein immobilization [11]," *Journal of the American Chemical Society*, vol. 123, no. 16, pp. 3838–3839, 2001.

[100] R. J. Chen, S. Bangsaruntip, K. A. Drouvalakis, N. Wong Shi Kam, M. Shim, Y. Li, W. Kim, P. J. Utz, and H. Dai, "Noncovalent functionalization of carbon nanotubes for highly specific electronic biosensors," *Proceedings of the National Academy of Sciences of the United States of America*, vol. 100, no. 9, pp. 4984–4989, 2003.

[101] Y. L. Zhao and J. F. Stoddart, "Noncovalent functionalization of single-walled carbon nanotubes," *Accounts of Chemical Research*, vol. 42, no. 8, pp. 1161–1171, 2009.

[102] M. Zheng, A. Jagota, E. D. Semke, B. A. Diner, R. S. McLean, S. R. Lustig, R. E. Richardson, and N. G. Tassi, "DNA-assisted dispersion and separation of carbon nanotubes," *Nature Materials*, vol. 2, no. 5, pp. 338–342, 2003.

[103] A. Star, J. F. Stoddart, D. Steuerman, M. Diehl, A. Boukai, E. W. Wong, X. Yang, S. W. Chung, H. Choi, and J. R. Heath, "Preparation and properties of polymer-wrapped single-walled carbon nanotubes," *Angewandte Chemie - International Edition*, vol. 40, no. 9, pp. 1721–1725, 2001.

[104] A. Star, D. W. Steuerman, J. R. Heath, and J. F. Stoddart, "Starched carbon nanotubes," *Angewandte Chemie - International Edition*, vol. 41, no. 14, pp. 2508–2512, 2002.

[105] S. Vardharajula, S. Z. Ali, P. M. Tiwari, E. Eroğlu, K. Vig, V. A. Dennis, and S. R. Singh, "Functionalized carbon nanotubes: Biomedical applications," *International Journal of Nanomedicine*, vol. 7, pp. 5361–5374, 2012.

[106] D. Pantarotto, C. D. Partidos, R. Graff, J. Hoebeke, J.-P. Briand, M. Prato, and A. Bianco, "Synthesis, structural characterization, and immunological properties of carbon nanotubes functionalized with peptides," *Journal of the American Chemical Society*, vol. 125, pp. 6160–6164, 04 2003.

[107] A. Guiseppi-Elie, C. Lei, and R. H. Baughman, "Direct electron transfer of glucose oxidase on carbon nanotubes," *Nanotechnology*, vol. 13, no. 5, pp. 559–564, 2002.

[108] R. Singh, D. Pantarotto, D. McCarthy, O. Chaloin, J. Hoebeke, C. D. Partidos, J.-P. Briand, M. Prato, A. Bianco, and K. Kostarelos, "Binding and condensation of plasmid dna onto functionalized carbon nanotubes: Toward the construction of nanotube-based gene delivery vectors," *Journal of the American Chemical Society*, vol. 127, pp. 4388–4396, 03 2005.

[109] Y. Liu, D. C. Wu, W. D. Zhang, X. Jiang, C. B. He, T. S. Chung, S. H. Goh, and K. W. Leong, "Polyethylenimine-grafted multiwalled carbon nanotubes for secure noncovalent immobilization and efficient delivery of DNA," *Angewandte Chemie - International Edition*, vol. 44, no. 30, pp. 4782–4785, 2005.

[110] Q. Lu, J. M. Moore, G. Huang, A. S. Mount, A. M. Rao, L. L. Larcom, and P. C. Ke, "RNA polymer translocation with single-walled carbon nanotubes," *Nano Letters*, vol. 4, no. 12, pp. 2473–2477, 2004.

[111] K. Kostarelos, A. Bianco, and M. Prato, "Promises, facts and challenges for carbon nanotubes in imaging and therapeutics," *Nature Nanotechnology*, vol. 4, no. 10, pp. 627–633, 2009.

[112] L. Stryer, *Biochemistry*. W.H. Freeman, New York, 3rd ed. ed., 1988.

[113] Z. Liu, S. Tabakman, K. Welsher, and H. Dai, "Carbon nanotubes in biology and medicine: In vitro and in vivo detection, imaging and drug delivery," *Nano Research*, vol. 2, no. 2, pp. 85–120, 2009.

[114] M. Prato, K. Kostarelos, and A. Bianco, "Functionalized carbon nanotubes in drug design and discovery," *Accounts of Chemical Research*, vol. 41, no. 1, pp. 60–68, 2008.

[115] A. Bianco, K. Kostarelos, and M. Prato, "Applications of carbon nanotubes in drug delivery," *Current Opinion in Chemical Biology*, vol. 9, no. 6, pp. 674–679, 2005.

[116] Z. Liu, K. Chen, C. Davis, S. Sherlock, Q. Cao, X. Chen, and H. Dai, "Drug delivery with carbon nanotubes for in vivo cancer treatment," *Cancer Research*, vol. 68, no. 16, pp. 6652–6660, 2008.

[117] Z. Liu, M. Winters, M. Holodniy, and H. Dai, "siRNA delivery into human T cells and primary cells with carbon-nanotube transporters," *Angewandte Chemie - International Edition*, vol. 46, no. 12, pp. 2023–2027, 2007.

[118] J. Wang, "Carbon-nanotube based electrochemical biosensors: A review," *Electroanalysis*, vol. 17, no. 1, pp. 7–14, 2005.

[119] D. Pantarotto, C. D. Partidos, J. Hoebeke, F. Brown, E. Kramer, J. P. Briand, S. Muller, M. Prato, and A. Bianco, "Immunization with peptide-functionalized carbon nanotubes enhances virus-specific neutralizing antibody responses," *Chemistry and Biology*, vol. 10, no. 10, pp. 961–966, 2003.

[120] L. Lacerda, J. Russier, G. Pastorin, M. A. Herrero, E. Venturelli, H. Dumortier, K. T. Al-Jamal, M. Prato, K. Kostarelos, and A. Bianco, "Translocation mecha-

nisms of chemically functionalised carbon nanotubes across plasma membranes," *Biomaterials*, vol. 33, no. 11, pp. 3334–3343, 2012.

[121] K. Kostarelos, L. Lacerda, G. Pastorin, W. Wu, S. Wieckowski, J. Luangsivilay, S. Godefroy, D. Pantarotto, J. P. Briand, S. Muller, M. Prato, and A. Bianco, "Cellular uptake of functionalized carbon nanotubes is independent of functional group and cell type," *Nature Nanotechnology*, vol. 2, no. 2, pp. 108–113, 2007.

[122] H. Ali-Boucetta, K. T. Al-Jamal, K. H. Müller, S. Li, A. E. Porter, A. Eddaoudi, M. Prato, A. Bianco, and K. Kostarelos, "Cellular uptake and cytotoxic impact of chemically functionalized and polymer-coated carbon nanotubes," *Small*, vol. 7, no. 22, pp. 3230–3238, 2011.

[123] M. Bottini, S. Bruckner, K. Nika, N. Bottini, S. Bellucci, A. Magrini, A. Bergamaschi, and T. Mustelin, "Multi-walled carbon nanotubes induce t lymphocyte apoptosis," *Toxicology Letters*, vol. 160, no. 2, pp. 121–126, 2006.

[124] C. Cheng, K. H. Müller, K. K. K. Koziol, J. N. Skepper, P. A. Midgley, M. E. Welland, and A. E. Porter, "Toxicity and imaging of multi-walled carbon nanotubes in human macrophage cells," *Biomaterials*, vol. 30, no. 25, pp. 4152–4160, 2009.

[125] C. Cheng, A. E. Porter, K. Muller, K. Koziol, J. N. Skepper, P. Midgley, and M. Welland, "Imaging carbon nanoparticles and related cytotoxicity," *Journal of Physics: Conference Series*, vol. 151, 2009.

[126] L. Ding, J. Stilwell, T. Zhang, O. Elboudwarej, H. Jiang, J. P. Selegue, P. A. Cooke, J. W. Gray, and F. F. Chen, "Molecular characterization of the cytotoxic mechanism of multiwall carbon nanotubes and nano-onions on human skin fibroblast," *Nano Letters*, vol. 5, no. 12, pp. 2448–2464, 2005.

[127] A. A. Shvedova, V. Castranova, E. R. Kisin, D. Schwegler-Berry, A. R. Murray, V. Z. Gandelsman, A. Maynard, and P. Baron, "Exposure to carbon nanotube material: Assessment of nanotube cytotoxicity using human keratinocyte cells," *Journal of Toxicology and Environmental Health - Part A*, vol. 66, no. 20, pp. 1909–1926, 2003.

[128] A. A. Shvedova, E. R. Kisin, R. Mercer, A. R. Murray, V. J. Johnson, A. I. Potapovich, Y. Y. Tyurina, O. Gorelik, S. Arepalli, D. Schwegler-Berry, A. F. Hubbs, J. Antonini, D. E. Evans, B. K. Ku, D. Ramsey, A. Maynard, V. E. Kagan, V. Castranova, and P. Baron, "Unusual inflammatory and fibrogenic pulmonary responses to single-walled carbon nanotubes in mice," *American Journal of Physiology - Lung Cellular and Molecular Physiology*, vol. 289, no. 5 33-5, pp. L698–L708, 2005.

[129] X. Zhao and R. Liu, "Recent progress and perspectives on the toxicity of carbon nanotubes at organism, organ, cell, and biomacromolecule levels," *Environment International*, vol. 40, no. 1, pp. 244–255, 2012.

[130] X. Wang, G. Jia, H. Wang, H. Nie, L. Yan, X. Y. Deng, and S. Wang, "Diameter effects on cytotoxicity of multi-walled carbon nanotubes," *Journal of Nanoscience and Nanotechnology*, vol. 9, no. 5, pp. 3025–3033, 2009.

[131] D. Cui, F. Tian, C. S. Ozkan, M. Wang, and H. Gao, "Effect of single wall carbon nanotubes on human HEK293 cells," *Toxicology Letters*, vol. 155, no. 1, pp. 73–85, 2005.

[132] A. E. Porter, M. Gass, K. Muller, J. N. Skepper, P. A. Midgley, and M. Welland, "Direct imaging of single-walled carbon nanotubes in cells," *Nature Nanotechnology*, vol. 2, no. 11, pp. 713–717, 2007.

[133] G. Jia, H. Wang, L. Yan, X. Wang, R. Pei, T. Yan, Y. Zhao, and X. Guo, "Cytotoxicity of carbon nanomaterials: Single-wall nanotube, multi-wall nanotube, and fullerene," *Environmental Science and Technology*, vol. 39, no. 5, pp. 1378–1383, 2005.

[134] C. M. Sayes, F. Liang, J. L. Hudson, J. Mendez, W. Guo, J. M. Beach, V. C. Moore, C. D. Doyle, J. L. West, W. E. Billups, K. D. Ausman, and V. L. Colvin, "Functionalization density dependence of single-walled carbon nanotubes cytotoxicity in vitro," *Toxicology Letters*, vol. 161, no. 2, pp. 135–142, 2006.

[135] A. R. Leach, *Molecular Modelling: Principles and Applications*. Prentice Hall, 2001.

[136] M. A. Ditzler, M. Otyepka, J. Šponer, and N. G. Walter, "Molecular dynamics and quantum mechanics of RNA: Conformational and chemical change we can believe in," *Accounts of Chemical Research*, vol. 43, no. 1, pp. 40–47, 2010.

[137] H. Liu, M. Elstner, E. Kaxiras, T. Frauenheim, J. Hermans, and W. Yang, "Quantum mechanics simulation of protein dynamics on long timescale," *Proteins: Structure, Function and Genetics*, vol. 44, no. 4, pp. 484–489, 2001.

[138] M. Born and R. Oppenheimer, "Zur Quantentheorie der Molekeln," *Annalen der Physik*, vol. 389, no. 20, pp. 457–484, 1927.

[139] B. Hess, C. Kutzner, D. van der Spoel, and E. Lindahl, "GROMACS 4: Algorithms for Highly Efficient, Load-Balanced, and Scalable Molecular Simulation," *Journal of Chemical Theory and Computation*, vol. 4, no. 3, pp. 435–447, 2008.

[140] "GROMACS Manual: http://www.gromacs.org/Documentation/Manual."

[141] W. van Gunsteren, *Biomolecular Simulation: The GROMOS96 Manual and User Guide*. Biomos Zürich, 1996.

[142] P. M. Morse, "Diatomic molecules according to the wave mechanics. II. Vibrational levels," *Physical Review*, vol. 34, no. 1, pp. 57–64, 1929.

[143] P. Bond and M. Sansom, "Insertion and assembly of membrane proteins via simulation," *Journal of the American Chemical Society*, vol. 128, no. 8, pp. 2697–2704, 2006.

[144] S. Marrink, A. De Vries, and A. Mark, "Coarse grained model for semiquantitative lipid simulations," *Journal of Physical Chemistry B*, vol. 108, no. 2, pp. 750–760, 2004.

[145] S. Marrink, H. Risselada, S. Yefimov, D. Tieleman, and A. De Vries, "The MARTINI force field: Coarse grained model for biomolecular simulations," *Journal of Physical Chemistry B*, vol. 111, no. 27, pp. 7812–7824, 2007.

[146] W. D. Cornell, P. Cieplak, C. I. Bayly, I. R. Gould, K. M. Merz Jr., D. M. Ferguson, D. C. Spellmeyer, T. Fox, J. W. Caldwell, and P. A. Kollman, "A second generation force field for the simulation of proteins, nucleic acids, and organic molecules," *Journal of the American Chemical Society*, vol. 117, no. 19, pp. 5179–5197, 1995.

[147] Y. Duan, C. Wu, S. Chowdhury, M. C. Lee, G. Xiong, W. Zhang, R. Yang, P. Cieplak, R. Luo, T. Lee, J. Caldwell, J. Wang, and P. Kollman, "A point-charge force field for molecular mechanics simulations of proteins based on condensed-phase quantum mechanical calculations," *Journal of Computational Chemistry*, vol. 24, no. 16, pp. 1999–2012, 2003.

[148] W. L. Jorgensen, D. S. Maxwell, and J. Tirado-Rives, "Development and testing of the OPLS all-atom force field on conformational energetics and properties of organic liquids," *Journal of the American Chemical Society*, vol. 118, no. 45, pp. 11225–11236, 1996.

[149] G. A. Kaminski, R. A. Friesner, J. Tirado-Rives, and W. L. Jorgensen, "Evaluation and reparametrization of the OPLS-AA force field for proteins via comparison with accurate quantum chemical calculations on peptides," *Journal of Physical Chemistry B*, vol. 105, no. 28, pp. 6474–6487, 2001.

[150] A. D. MacKerell Jr., D. Bashford, M. Bellott, R. L. Dunbrack Jr., J. D. Evanseck, M. J. Field, S. Fischer, J. Gao, H. Guo, S. Ha, D. Joseph-McCarthy, L. Kuchnir, K. Kuczera, F. T. K. Lau, C. Mattos, S. Michnick, T. Ngo, D. T. Nguyen, B. Prodhom, W. E. Reiher III, B. Roux, M. Schlenkrich, J. C. Smith, R. Stote, J. Straub, M. Watanabe, J. Wiórkiewicz-Kuczera, D. Yin, and M. Karplus, "All-atom empirical potential for molecular modeling and dynamics studies of proteins," *Journal of Physical Chemistry B*, vol. 102, no. 18, pp. 3586–3616, 1998.

[151] R. C. Rizzo and W. L. Jorgensen, "OPLS all-atom model for amines: Resolution of the amine hydration problem," *Journal of the American Chemical Society*, vol. 121, no. 20, pp. 4827–4836, 1999.

[152] S. E. Feller and A. D. MacKerell Jr., "An improved empirical potential energy function for molecular simulations of phospholipids," *Journal of Physical Chemistry B*, vol. 104, no. 31, pp. 7510–7515, 2000.

[153] R. DeVane, M. L. Klein, C.-c. Chiu, S. O. Nielsen, W. Shinoda, and P. B. Moore, "Coarse-grained potential models for phenyl-based molecules: I. parametrization using experimental data," *The Journal of Physical Chemistry B*, vol. 114, no. 19, pp. 6386–6393, 2010.

[154] R. DeVane, A. Jusufi, W. Shinoda, C.-c. Chiu, S. O. Nielsen, P. B. Moore, and M. L. Klein, "Parametrization and application of a coarse grained force field for benzene/fullerene interactions with lipids," *The Journal of Physical Chemistry B*, vol. 114, no. 49, pp. 16364–16372, 2010.

[155] G. Voth, *Coarse-Graining of Condensed Phase and Biomolecular Systems*. Taylor & Francis, 2008.

[156] J. P. Ulmschneider and M. B. Ulmschneider, "United atom lipid parameters for combination with the optimized potentials for liquid simulations all-atom force field," *Journal of Chemical Theory and Computation*, vol. 5, no. 7, pp. 1803–1813, 2009.

[157] R. W. Hockney, S. P. Goel, and J. W. Eastwood, "Quiet high-resolution computer models of a plasma," *Journal of Computational Physics*, vol. 14, no. 2, pp. 148–158, 1974.

[158] L. Verlet, "Computer "experiments" on classical fluids. I. Thermodynamical properties of Lennard-Jones molecules," *Physical Review*, vol. 159, no. 1, pp. 98–103, 1967.

[159] P. Allen and D. Tildesley, *Computer Simulation of Liquids*. Clarendon Press, 1989.

[160] D. Frenkel and B. Smit, *Understanding Molecular Simulation: From Algorithms to Applications*. Academic Press, 2002.

[161] B. Hess, H. Bekker, H. J. C. Berendsen, and J. G. E. M. Fraaije, "LINCS: A Linear Constraint Solver for molecular simulations," *Journal of Computational Chemistry*, vol. 18, no. 12, pp. 1463–1472, 1997.

[162] O. Becker, A. MacKerell, B. Roux, and M. Watanabe, *Computational Biochemistry and Biophysics*. Marcel Dekker Incorporated, 2001.

[163] S. E. Feller, R. W. Pastor, A. Rojnuckarin, S. Bogusz, and B. R. Brooks, "Effect of electrostatic force truncation on interfacial and transport properties of water," *The Journal of Physical Chemistry*, vol. 100, no. 42, pp. 17011–17020, 1996.

[164] S. Marrink and D. Tieleman, "Perspective on the martini model," *Chemical Society Reviews*, vol. 42, no. 16, pp. 6801–6822, 2013. cited By (since 1996)5.

[165] H. Berendsen, J. Postma, W. Van Gunsteren, A. Dinola, and J. Haak, "Molecular dynamics with coupling to an external bath," *The Journal of Chemical Physics*, vol. 81, no. 8, pp. 3684–3690, 1984.

[166] G. Bussi, D. Donadio, and M. Parrinello, "Canonical sampling through velocity rescaling," *The Journal of Chemical Physics*, vol. 126, no. 1, pp. –, 2007.

[167] W. G. Hoover, "Canonical dynamics: Equilibrium phase-space distributions," *Physical Review A*, vol. 31, pp. 1695–1697, 03 1985.

[168] N. Michaud-Agrawal, E. J. Denning, T. B. Woolf, and O. Beckstein, "MDAnalysis: A toolkit for the analysis of molecular dynamics simulations," *Journal of Computational Chemistry*, vol. 32, no. 10, pp. 2319–2327, 2011.

[169] W. Humphrey, A. Dalke, and K. Schulten, "VMD – Visual Molecular Dynamics," *Journal of Molecular Graphics*, vol. 14, pp. 33–38, 1996.

[170] J. Stone, "An Efficient Library for Parallel Ray Tracing and Animation," Master's thesis, Computer Science Department, University of Missouri-Rolla, 1998.

[171] T. Williams and C. K. et al., "Gnuplot 4.4: an interactive plotting program." http://gnuplot.sourceforge.net/, 2010.

[172] J. N. Israelachvili and D. Tabor, "The measurement of Van Der Waals dispersion forces in the range 1.5 to 130 nm," *Proceedings of the Royal Society of London. A. Mathematical and Physical Sciences*, vol. 331, no. 1584, pp. 19–38, 1972.

[173] D. Tabor and R. H. S. Winterton, "The direct measurement of normal and retarded van der Waals forces," *Proceedings of the Royal Society of London. A. Mathematical and Physical Sciences*, vol. 312, no. 1511, pp. 435–450, 1969.

[174] B. Bhushan, *Principles and Applications of Tribology*. A Wiley interscience publication, Wiley, 1999.

[175] G. Binnig and H. Rohrer, "Scanning tunnelling microscopy," *Helvetica Physica Acta*, vol. 55, p. 726, 1982.

[176] G. Binnig, C. Quate, and C. Gerber, "Atomic force microscope," *Physical Review Letters*, vol. 56, no. 9, pp. 930–933, 1986.

[177] L. Gross, F. Mohn, N. Moll, P. Liljeroth, and G. Meyer, "The chemical structure of a molecule resolved by atomic force microscopy," *Science*, vol. 325, no. 5944, pp. 1110–1114, 2009.

[178] D. J. Müller, H.-J. Sass, S. A. Müller, G. Büldt, and A. Engel, "Surface structures of native bacteriorhodopsin depend on the molecular packing arrangement in the membrane," *Journal of Molecular Biology*, vol. 285, no. 5, pp. 1903 – 1909, 1999.

[179] H.-J. Butt and M. Jaschke, "Calculation of thermal noise in atomic force microscopy," *Nanotechnology*, vol. 6, no. 1, pp. 1–7, 1995.

[180] Y. Gan, "Atomic and subnanometer resolution in ambient conditions by atomic force microscopy," *Surface Science Reports*, vol. 64, no. 3, pp. 99 – 121, 2009.

[181] D. Müller and A. Engel, "The height of biomolecules measured with the atomic force microscope depends on electrostatic interactions," *Biophysical Journal*, vol. 73, no. 3, pp. 1633–1644, 1997.

[182] D. Müller and Y. Dufrêne, "Atomic force microscopy as a multifunctional molecular toolbox in nanobiotechnology," *Nature Nanotechnology*, vol. 3, no. 5, pp. 261–269, 2008.

[183] G. Meyer and N. M. Amer, "Novel optical approach to atomic force microscopy," *Applied Physics Letters*, vol. 53, no. 12, pp. 1045–1047, 1988.

[184] S. Alexander, L. Hellemans, O. Marti, J. Schneir, V. Elings, P. K. Hansma, M. Longmire, and J. Gurley, "An atomic-resolution atomic-force microscope implemented using an optical lever," *Journal of Applied Physics*, vol. 65, no. 1, pp. 164–167, 1989.

[185] J. Gallego-Juarez, "Piezoelectric ceramics and ultrasonic transducers," *Journal of Physics E: Scientific Instruments*, vol. 22, no. 10, pp. 804–816, 1989.

[186] F. London, "The general theory of molecular forces," *Trans. Faraday Soc.*, vol. 33, pp. 8b–26, 1937.

[187] D. C. Grahame, "Diffuse double layer theory for electrolytes of unsymmetrical valence types," *The Journal of Chemical Physics*, vol. 21, no. 6, pp. 1054–1060, 1953.

[188] E. J. W. Verwey, *Theory of the stability of lyophobic colloids: the interaction of sol particles having an electric double layer*. Elsevier, 1948.

[189] L. Cheng, P. Fenter, K. L. Nagy, M. L. Schlegel, and N. C. Sturchio, "Molecular-scale density oscillations in water adjacent to a mica surface," *Phys. Rev. Lett.*, vol. 87, p. 156103, 2001.

[190] W. J. Huisman, J. F. Peters, M. J. Zwanenburg, S. A. de Vries, T. E. Derry, D. Abernathy, and J. F. van der Veen, "Layering of a liquid metal in contact with a hard wall," *Nature*, vol. 390, no. 6658, pp. 379–381, 1997.

[191] H. Hertz, "Über die Berührung fester elastischer Körper," *Journal für die reine und angewandte Mathematik*, vol. 92, p. 156, 1881.

[192] K. L. Johnson, *Contact Mechanics*. Cambridge University Press, 1987.

[193] I. N. Sneddon, "The relation between load and penetration in the axisymmetric boussinesq problem for a punch of arbitrary profile," *International Journal of Engineering Science*, vol. 3, no. 1, pp. 47–57, 1965.

[194] M. Heuberger, G. Dietler, and L. Schlapbach, "Elastic deformations of tip and sample during atomic force microscope measurements," *Journal of Vacuum Science and Technology B: Microelectronics and Nanometer Structures*, vol. 14, no. 2, pp. 1250–1254, 1996.

[195] B. V. Derjaguin, V. M. Müller, and Y. P. Toporov, "Effect of contact deformations on the adhesion of particles," *Journal of Colloid And Interface Science*, vol. 53, no. 2, pp. 314–326, 1975.

[196] B. Cappella and G. Dietler, "Force-distance curves by atomic force microscopy," *Surface Science Reports*, vol. 34, no. 1-3, pp. 1–104, 1999.

[197] K. L. Johnson, K. Kendall, and A. D. Roberts, "Surface energy and the contact of elastic solids," *Proceedings of the Royal Society of London. A. Mathematical and Physical Sciences*, vol. 324, no. 1558, pp. 301–313, 1971.

[198] R. S. Bradley, "LXXIX. the cohesive force between solid surfaces and the surface energy of solids," *Philosophical Magazine Series 7*, vol. 13, no. 86, pp. 853–862, 1932.

[199] D. Maugis, "Adhesion of spheres: The JKR-DMT transition using a Dugdale model," *Journal of Colloid And Interface Science*, vol. 150, no. 1, pp. 243–269, 1992.

[200] D. S. Dugdale, "Yielding of steel sheets containing slits," *Journal of the Mechanics and Physics of Solids*, vol. 8, no. 2, pp. 100–104, 1960.

[201] K. L. Johnson and J. A. Greenwood, "An adhesion map for the contact of elastic spheres," *Journal of Colloid and Interface Science*, vol. 192, no. 2, pp. 326–333, 1997.

[202] J. Domke and M. Radmacher, "Measuring the elastic properties of thin polymer films with the atomic force microscope," *Langmuir*, vol. 14, no. 12, pp. 3320–3325, 1998.

[203] R. S. Chadwick, "Axisymmetric indentation of a thin incompressible elastic layer," *SIAM Journal on Applied Mathematics*, vol. 62, no. 5, pp. 1520–1530, 2002.

[204] Y. Martin, C. C. Williams, and H. K. Wickramasinghe, "Atomic force microscope-force mapping and profiling on a sub 100-A scale," *Journal of Applied Physics*, vol. 61, no. 10, pp. 4723–4729, 1987.

[205] Q. Zhong, D. Inniss, K. Kjoller, and V. B. Elings, "Fractured polymer/silica fiber surface studied by tapping mode atomic force microscopy," *Surface Science*, vol. 290, no. 1-2, pp. L688–L692, 1993.

[206] R. García and R. Pérez, "Dynamic atomic force microscopy methods," *Surface Science Reports*, vol. 47, no. 6-8, pp. 197–301, 2002.

[207] B. Anczykowski, B. Gotsmann, H. Fuchs, J. P. Cleveland, and V. B. Elings, "How to measure energy dissipation in dynamic mode atomic force microscopy," *Applied Surface Science*, vol. 140, no. 3-4, pp. 376–382, 1999.

[208] J. P. Cleveland, B. Anczykowski, A. E. Schmid, and V. B. Elings, "Energy dissipation in tapping-mode atomic force microscopy," *Applied Physics Letters*, vol. 72, no. 20, pp. 2613–2615, 1998.

[209] R. Garcia, C. J. Gómez, N. F. Martinez, S. Patil, C. Dietz, and R. Magerle, "Identification of nanoscale dissipation processes by dynamic atomic force microscopy," *Physical Review Letters*, vol. 97, no. 1, 2006.

[210] J. Tamayo and R. García, "Effects of elastic and inelastic interactions on phase contrast images in tapping-mode scanning force microscopy," *Applied Physics Letters*, vol. 71, no. 16, pp. 2394–2396, 1997.

[211] R. García and A. San Paulo, "Attractive and repulsive tip-sample interaction regimes in tapping-mode atomic force microscopy," *Physical Review B*, vol. 60, no. 7, pp. 4961–4967, 1999.

[212] R. Garcia and A. San Paulo, "Dynamics of a vibrating tip near or in intermittent contact with a surface," *Physical Review B - Condensed Matter and Materials Physics*, vol. 61, no. 20, pp. R13381–R13384, 2000.

[213] R. W. Stark, "Bistability, higher harmonics, and chaos in AFM," *Materials Today*, vol. 13, no. 9, pp. 24–32, 2010.

[214] T. E. Schaffer, J. P. Cleveland, F. Ohnesorge, D. A. Walters, and P. K. Hansma, "Studies of vibrating atomic force microscope cantilevers in liquid," *Journal of Applied Physics*, vol. 80, no. 7, pp. 3622–3627, 1996.

[215] G. Y. Chen, R. J. Warmack, A. Huang, and T. Thundat, "Harmonic response of near-contact scanning force microscopy," *Journal of Applied Physics*, vol. 78, no. 3, pp. 1465–1469, 1995.

[216] S. J. O'Shea, M. A. Lantz, and H. Tokumoto, "Damping near solid-liquid interfaces measured with atomic force microscopy," *Langmuir*, vol. 15, no. 4, pp. 922–925, 1999.

[217] H. J. Butt, B. Cappella, and M. Kappl, "Force measurements with the atomic force microscope: Technique, interpretation and applications," *Surface Science Reports*, vol. 59, no. 1-6, pp. 1–152, 2005.

[218] L. Monticelli, E. Salonen, P. Ke, and I. Vattulainen, "Effects of carbon nanoparticles on lipid membranes: A molecular simulation perspective," *Soft Matter*, vol. 5, no. 22, pp. 4433–4445, 2009.

[219] E. Wallace and M. Sansom, "Carbon nanotube self-assembly with lipids and detergent: A molecular dynamics study," *Nanotechnology*, vol. 20, no. 4, 2009.

[220] E. Wallace and M. Sansom, "Carbon nanotube/detergent interactions via coarse-grained molecular dynamics," *Nano Letters*, vol. 7, no. 7, pp. 1923–1928, 2007.

[221] J. Wong-Ekkabut, S. Baoukina, W. Triampo, I. M. Tang, D. P. Tieleman, and L. Monticelli, "Computer simulation study of fullerene translocation through lipid membranes," *Nature Nanotechnology*, vol. 3, no. 6, pp. 363–368, 2008.

[222] S. Pogodin and V. Baulin, "Can a carbon nanotube pierce through a phospholipid bilayer?," *ACS Nano*, vol. 4, no. 9, pp. 5293–5300, 2010. cited By (since 1996)32.

[223] S. Kraszewski, A. Bianco, M. Tarek, and C. Ramseyer, "Insertion of short amino-functionalized single-walled carbon nanotubes into phospholipid bilayer occurs by passive diffusion," *PLoS ONE*, vol. 7, no. 7, 2012.

[224] R. Parthasarathi, N. R. Tummala, and A. Striolo, "Embedded single-walled carbon nanotubes locally perturb DOPC phospholipid bilayers," *Journal of Physical Chemistry B*, vol. 116, no. 42, pp. 12769–12782, 2012.

[225] Y. M. Ban and D. I. Kopelevich, "Effects of carbon nanotubes on structure and elasticity of lipid bilayers," *Current Nanoscience*, vol. 7, no. 5, pp. 674–689, 2011.

[226] S. Kraszewski, F. Picaud, I. Elhechmi, T. Gharbi, and C. Ramseyer, "How long a functionalized carbon nanotube can passively penetrate a lipid membrane," *Carbon*, vol. 50, no. 14, pp. 5301–5308, 2012.

[227] R. S. G. D'Rozario, C. L. Wee, E. Jayne Wallace, and M. S. P. Sansom, "The interaction of C60 and its derivatives with a lipid bilayer via molecular dynamics simulations," *Nanotechnology*, vol. 20, no. 11, 2009.

[228] B. Liu, X. Li, B. Li, B. Xu, and Y. Zhao, "Carbon nanotube based artificial water channel protein: Membrane perturbation and water transportation," *Nano Letters*, vol. 9, no. 4, pp. 1386–1394, 2009.

[229] P. Raczyński, K. Górny, M. Pabiszczak, and Z. Gburski, "Nanoindentation of biomembrane by carbon nanotubes – MD simulation," *Computational Materials Science*, vol. 70, pp. 13 – 18, 2013.

[230] E. Wallace and M. Sansom, "Blocking of carbon nanotube based nanoinjectors by lipids: A simulation study," *Nano Letters*, vol. 8, no. 9, pp. 2751–2756, 2008.

[231] S. Nielsen, B. Ensing, V. Ortiz, P. Moore, and M. Klein, "Lipid bilayer perturbations around a transmembrane nanotube: A coarse grain molecular dynamics study," *Biophysical Journal*, vol. 88, no. 6, pp. 3822–3828, 2005.

[232] H. Berendsen, D. van der Spoel, and R. van Drunen, "GROMACS: A message-passing parallel molecular dynamics implementation," *Computer Physics Communications*, vol. 91, no. 1–3, pp. 43 – 56, 1995.

[233] J. Nagle and S. Tristram-Nagle, "Structure of lipid bilayers," *Biochimica et Biophysica Acta - Reviews on Biomembranes*, vol. 1469, no. 3, pp. 159–195, 2000.

[234] J. Israelachvili and R. Pashley, "Molecular layering of water at surfaces and origin of repulsive hydration forces," *Nature*, vol. 306, no. 5940, pp. 249–250, 1983.

[235] G. Van Meer, "Cellular lipidomics," *EMBO Journal*, vol. 24, no. 18, pp. 3159–3165, 2005.

[236] G. Van Meer, D. Voelker, and G. Feigenson, "Membrane lipids: Where they are and how they behave," *Nature Reviews Molecular Cell Biology*, vol. 9, no. 2, pp. 112–124, 2008.

[237] M. Nussio, G. Oncins, I. Ridelis, E. Szili, J. Shapter, F. Sanz, and N. Voelcker, "Nanomechanical characterization of phospholipid bilayer islands on flat and porous substrates: A force spectroscopy study," *Journal of Physical Chemistry B*, vol. 113, no. 30, pp. 10339–10347, 2009.

[238] R. Stevens, "New carbon nanotube AFM probe technology," *Materials Today*, vol. 12, no. 10, pp. 42–45, 2009.

[239] R. Stevens, N. Frederick, B. Smith, D. Morse, G. Stucky, and P. Hansma, "Carbon nanotubes as probes for atomic force microscopy," *Nanotechnology*, vol. 11, no. 1, pp. 1–5, 2000.

[240] D. Burns and K. Youcef-Toumi, "Shortening carbon nanotube-tipped AFM probes," *International Journal of Nanomanufacturing*, vol. 1, pp. 799–809, 2007.

[241] R. Stevens, C. Nguyen, and M. Meyyappan, "Nanomanipulation and fabrication by ion beam molding," *IEEE Transactions on Nanotechnology*, vol. 5, no. 3, pp. 255–257, 2006.

[242] R. M. Stevens, "US Patent 7601650: Carbon nanotube device and process for manufacturing same," 2009.

[243] B. Wei, J. D'Arcy-Gall, P. Ajayan, and G. Ramanath, "Tailoring structure and electrical properties of carbon nanotubes using kilo-electron-volt ions," *Applied Physics Letters*, vol. 83, no. 17, pp. 3581–3583, 2003.

[244] V. Nau. Private communication.

[245] L. McNeil and M. Grimsditch, "Elastic moduli of muscovite mica," *Journal of Physics: Condensed Matter*, vol. 5, no. 11, pp. 1681–1690, 1993.

[246] T. Bayerl and M. Bloom, "Physical properties of single phospholipid bilayers adsorbed to micro glass beads. a new vesicular model system studied by 2h-nuclear magnetic resonance," *Biophysical Journal*, vol. 58, no. 2, pp. 357–362, 1990.

[247] J. Israelachvili, "Adhesion forces between surfaces in liquids and condensable vapours," *Surface Science Reports*, vol. 14, no. 3, pp. 109–159, 1992.

[248] S. Jeffery, P. Hoffmann, J. Pethica, C. Ramanujan, H. Özer, and A. Oral, "Direct measurement of molecular stiffness and damping in confined water layers," *Physical Review B - Condensed Matter and Materials Physics*, vol. 70, no. 5, pp. 054114–1–054114–8, 2004.

[249] P. Hoffmann, S. Jeffery, A. Oral, R. Grimble, H. Ozer, and J. Pethica, "Nanomechanics using an ultra-small amplitude AFM," vol. 649, pp. Q9.2.1–Q9.2.6, 2001.

[250] "Iridis Compute Cluster. http://www.southampton.ac.uk/isolutions/computing/hpc/iridis/."

[251] "Oxford Supercomputing Centre. http://www.osc.ox.ac.uk/."

[252] S. Garcia-Manyes and F. Sanz, "Nanomechanics of lipid bilayers by force spectroscopy with AFM: A perspective," *Biochimica et Biophysica Acta - Biomembranes*, vol. 1798, no. 4, pp. 741–749, 2010.

[253] Y. Dufrêne and G. Lee, "Advances in the characterization of supported lipid films with the atomic force microscope," *Biochimica et Biophysica Acta - Biomembranes*, vol. 1509, no. 1-2, pp. 14–41, 2000.

[254] S. Loi, G. Sun, V. Franz, and H.-J. Butt, "Rupture of molecular thin films observed in atomic force microscopy. II. Experiment," *Physical Review E - Statistical, Nonlinear, and Soft Matter Physics*, vol. 66, no. 3, pp. 031602/1–031602/7, 2002.

[255] H.-J. Butt and V. Franz, "Rupture of molecular thin films observed in atomic force microscopy. I. Theory," *Physical Review E - Statistical, Nonlinear, and Soft Matter Physics*, vol. 66, no. 3, pp. 031601/1–031601/9, 2002.

[256] Z. Leonenko, E. Finot, H. Ma, T. Dahms, and D. Cramb, "Investigation of temperature-induced phase transitions in DOPC and DPPC phospholipid bilayers using temperature-controlled scanning force microscopy," *Biophysical Journal*, vol. 86, no. 6, pp. 3783–3793, 2004.

[257] S. Garcia-Manyes, G. Oncins, and F. Sanz, "Effect of temperature on the nanomechanics of lipid bilayers studied by force spectroscopy," *Biophysical Journal*, vol. 89, no. 6, pp. 4261–4274, 2005.

[258] S. Garcia-Manyes, G. Oncins, and F. Sanz, "Effect of ion-binding and chemical phospholipid structure on the nanomechanics of lipid bilayers studied by force spectroscopy," *Biophysical Journal*, vol. 89, no. 3, pp. 1812–1826, 2005.

[259] J. Schneider, W. Barger, and G. Lee, "Nanometer scale surface properties of supported lipid bilayers measured with hydrophobic and hydrophilic atomic force microscope probes," *Langmuir*, vol. 19, no. 5, pp. 1899–1907, 2003.

[260] Y. Dufrêne, T. Boland, J. Schneider, W. Barger, and G. Lee, "Characterization of the physical properties of model biomembranes at the nanometer scale with the atomic force microscope," *Faraday Discussions*, vol. 111, pp. 79–94, 1999.

[261] E. Dimitriadis, F. Horkay, J. Maresca, B. Kachar, and R. Chadwick, "Determination of elastic moduli of thin layers of soft material using the atomic force microscope," *Biophysical Journal*, vol. 82, no. 5, pp. 2798–2810, 2002.

[262] K. Voïtchovsky, S. Contera, M. Kamihira, A. Watts, and J. Ryan, "Differential stiffness and lipid mobility in the leaflets of purple membranes," *Biophysical Journal*, vol. 90, no. 6, pp. 2075–2085, 2006.

[263] C. Rutkowski, L. Williams, T. Haines, and H. Cummins, "The elasticity of synthetic phospholipid vesicles obtained by photon correlation spectroscopy," *Biochemistry*, vol. 30, no. 23, pp. 5688–5696, 1991.

[264] I. Mey, M. Stephan, E. Schmitt, M. Müller, M. Amar, C. Steinem, and A. Janshoff, "Local membrane mechanics of pore-spanning bilayers," *Journal of the American Chemical Society*, vol. 131, no. 20, pp. 7031–7039, 2009.

[265] S. Künneke, D. Krüger, and A. Janshoff, "Scrutiny of the failure of lipid membranes as a function of headgroups, chain length, and lamellarity measured by scanning force microscopy," *Biophysical Journal*, vol. 86, no. 3, pp. 1545–1553, 2004.

[266] S. Krüger, D. Krüger, and A. Janshoff, "Scanning force microscopy based rapid force curve acquisition on supported lipid bilayers: Experiments and simulations using pulsed force mode," *ChemPhysChem*, vol. 5, no. 7, pp. 989–997, 2004.

[267] M. A. Poggi, J. S. Boyles, L. A. Bottomley, A. W. McFarland, J. S. Colton, C. V. Nguyen, R. M. Stevens, and P. T. Lillehei, "Measuring the compression of a carbon nanospring," *Nano Letters*, vol. 4, no. 6, pp. 1009–1016, 2004.

[268] A. Csató, A. Szabó, A. Fonseca, D. Vuono, Z. Kónya, A. Volodin, C. V. Haesendonck, L. Biro, G. Giordano, and J. B. Nagy, "Synthesis and characterisation of coiled carbon nanotubes," *Catalysis Today*, vol. 181, no. 1, pp. 33 – 39, 2012.

[269] A. Szabó, A. Fonseca, J. Nagy, P. Lambin, and L. Biró, "Structural origin of coiling in coiled carbon nanotubes," *Carbon*, vol. 43, no. 8, pp. 1628–1633, 2005.

[270] M. Falvo, G. Clary, R. Taylor II, V. Chi, F. Brooks Jr., S. Washburn, and R. Superfine, "Bending and buckling of carbon nanotubes under large strain," *Nature*, vol. 389, no. 6651, pp. 582–584, 1997.

[271] D. Qian, G. Wagner, W. Liu, M.-F. Yu, and R. Ruoff, "Mechanics of carbon nanotubes," *Applied Mechanics Reviews*, vol. 55, no. 6, pp. 495–532, 2002.

[272] O. Lourie, D. Cox, and H. Wagner, "Buckling and collapse of embedded carbon nanotubes," *Physical Review Letters*, vol. 81, no. 8, pp. 1638–1641, 1998.

[273] L. Sudak, "Column buckling of multiwalled carbon nanotubes using nonlocal continuum mechanics," *Journal of Applied Physics*, vol. 94, no. 11, pp. 7281–7287, 2003.

[274] W. K. Den Otter and W. J. Briels, "The bending rigidity of an amphiphilic bilayer from equilibrium and nonequilibrium molecular dynamics," *Journal of Chemical Physics*, vol. 118, no. 10, pp. 4712–4720, 2003.

[275] R. Goetz, G. Gompper, and R. Lipowsky, "Mobility and elasticity of self-assembled membranes," *Physical Review Letters*, vol. 82, no. 1, pp. 221–224, 1999.

[276] E. Lindahl and O. Edholm, "Mesoscopic undulations and thickness fluctuations in lipid bilayers from molecular dynamics simulations," *Biophysical Journal*, vol. 79, no. 1, pp. 426–433, 2000.

[277] S. J. Marrink and A. E. Mark, "Effect of undulations on surface tension in simulated bilayers," *Journal of Physical Chemistry B*, vol. 105, no. 26, pp. 6122–6127, 2001.

[278] A. Naji, A. J. Levine, and P. A. Pincus, "Corrections to the saffman-delbrück mobility for membrane bound proteins," *Biophysical Journal*, vol. 93, no. 11, pp. L49–L51, 2007.

[279] P. G. Saffman and M. Delbrueck, "Brownian motion in biological membranes," *Proceedings of the National Academy of Sciences of the United States of America*, vol. 72, no. 8, pp. 3111–3113, 1975.

[280] Y. Gambin, M. Reffay, E. Sierecki, F. Homblé, R. S. Hodges, N. S. Gov, N. Taulier, and W. Urbach, "Variation of the lateral mobility of transmembrane peptides with hydrophobic mismatch," *Journal of Physical Chemistry B*, vol. 114, no. 10, pp. 3559–3566, 2010.

[281] U. Harzer and B. Bechinger, "Alignment of lysine-anchored membrane peptides under conditions of hydrophobic mismatch: A cd, 15n and 31p solid-state nmr spectroscopy investigation," *Biochemistry*, vol. 39, no. 43, pp. 13106–13114, 2000.

[282] S. K. Kandasamy and R. G. Larson, "Molecular dynamics simulations of model trans-membrane peptides in lipid bilayers: A systematic investigation of hydrophobic mismatch," *Biophysical Journal*, vol. 90, no. 7, pp. 2326–2343, 2006.

[283] J. A. Dix and A. S. Verkman, "Crowding effects on diffusion in solutions and cells," *Annual Review of Biophysics*, vol. 37, pp. 247–263, 2008.

[284] S. R. McGuffee and A. H. Elcock, "Diffusion, crowding & protein stability in a dynamic molecular model of the bacterial cytoplasm," *PLoS Computational Biology*, vol. 6, no. 3, 2010.

[285] J. E. Goose and M. S. P. Sansom, "Reduced lateral mobility of lipids and proteins in crowded membranes," *PLoS Computational Biology*, vol. 9, no. 4, 2013.

[286] J. Wohlert and O. Edholm, "Dynamics in atomistic simulations of phospholipid membranes: Nuclear magnetic resonance relaxation rates and lateral diffusion," *Journal of Chemical Physics*, vol. 125, no. 20, 2006.

[287] W. L. Vaz and P. F. Almeida, "Microscopic versus macroscopic diffusion in one-component fluid phase lipid bilayer membranes.," *Biophysical Journal*, vol. 60, no. 6, pp. 1553–1554, 1991.

[288] J. Tabony and B. Perly, "Quasielastic neutron scattering measurements of fast local translational diffusion of lipid molecules in phospholipid bilayers," *Biochimica et Biophysica Acta - Biomembranes*, vol. 1063, no. 1, pp. 67–72, 1991.

[289] M. Radmacher, "Measuring the elastic properties of biological samples with the afm," *IEEE Engineering in Medicine and Biology Magazine*, vol. 16, no. 2, pp. 47–57, 1997.

[290] Y. Li, X. Chen, and N. Gu, "Computational investigation of interaction between nanoparticles and membranes: Hydrophobic/hydrophilic effect," *Journal of Physical Chemistry B*, vol. 112, no. 51, pp. 16647–16653, 2008.

[291] K. T. Al-Jamal, H. Nerl, K. H. Müller, H. Ali-Boucetta, S. Li, P. D. Haynes, J. R. Jinschek, M. Prato, A. Bianco, K. Kostarelos, and A. E. Porter, "Cellular uptake mechanisms of functionalised multi-walled carbon nanotubes by 3D electron tomography imaging.," *Nanoscale*, vol. 3, no. 6, pp. 2627–2635, 2011.